

Pure-rotational and rotational-vibrational Raman spectrum of the atmosphere at an altitude of 23 km

Frédéric P. A. Vogt^{1,*}, Andrea Mehner², Pedro Figueira^{3,4}, Shanshan Yu⁵, Florian Kerber,⁶ Thomas Pfrommer,⁶ Wolfgang Hackenberg⁶, and Domenico Bonaccini Calia⁶

¹Federal Office of Meteorology and Climatology MeteoSwiss, Chemin de l'Aérologie 1, 1530 Payerne, Switzerland

²European Southern Observatory (ESO), Av. Alonso de Córdova 3107, 763 0355 Vitacura, Santiago, Chile

³Department of Astronomy, University of Geneva, Chemin Pegasi 51, Versoix, Switzerland

⁴Instituto de Astrofísica e Ciências do Espaço, Universidade do Porto, CAUP, Rua das Estrelas, 4150-762 Porto, Portugal

⁵Jet Propulsion Laboratory, California Institute of Technology, Pasadena, California 91109, USA

⁶European Southern Observatory (ESO), Karl-Schwarzschild-Str. 2, 85748 Garching, Germany



(Received 6 May 2022; accepted 10 April 2023; published 1 June 2023)

Ground-based optical astronomical observations supported by or in the vicinity of laser guide-star systems can be contaminated by Raman-scattered laser photons. Anticipating, alleviating, and correcting for the impact of this self-inflicted contamination requires a detailed knowledge of the pure-rotational and rotational-vibrational spectrum of the molecules in our atmosphere. We present a 15.3-hr-deep combined spectrum of the 4LGSF's 589 nm \approx 509 THz sodium laser beams of Paranal observatory, acquired with the ESPRESSO spectrograph at a resolution $\lambda/\Delta\lambda \cong 140000 \approx 0.12 \text{ cm}^{-1}$ and an altitude of 23 km above mean sea level. We identify 865 Raman lines over the spectral range of [3770; 7900] Å \approx [+9540; -4315] cm $^{-1}$, with relative intensities spanning ~ 5 orders of magnitudes. These lines are associated to the most abundant molecules of dry air, including their isotopes: $^{14}\text{N}^{14}\text{N}$, $^{14}\text{N}^{15}\text{N}$, $^{16}\text{O}^{16}\text{O}$, $^{16}\text{O}^{17}\text{O}$, $^{16}\text{O}^{18}\text{O}$, and $^{12}\text{C}^{16}\text{O}^{16}\text{O}$. The signal-to-noise of these observations implies that professional observatories can treat the resulting catalog of Raman lines as exhaustive (for the detected molecules, over the observed Raman shift range) for the purpose of predicting/correcting/exploiting Raman lines in astronomical data. Our observations also reveal that the four laser units of the 4LGSF do not all lase at the same central wavelength. We measure a blueshift of $+43 \pm 10 \text{ MHz} \cong -50 \pm 10 \text{ fm}$ with respect to $\lambda_* = 5891.59120 \text{ Å}$ for LGSU1/2, and $+94 \pm 10 \text{ MHz} \cong -109 \pm 10 \text{ fm}$ for LGSU3/4. These offsets, including the difference of $\sim 50 \text{ MHz}$ between LGSU1/2 and LGSU3/4, are larger than the observed 4LGSF spectral stability of $\pm 3 \text{ MHz}$ over hours. They remain well within the operational requirements for creating artificial laser guide-stars, but hinder the assessment of the radial velocity accuracy of ESPRESSO at the required level of 10 m s^{-1} . Altogether, our observations demonstrate how Raman lines can be exploited by professional observatories as highly-accurate, on-sky wavelength references.

DOI: 10.1103/PhysRevResearch.5.023145

I. INTRODUCTION

Laser guide-star systems, supporting adaptative optical techniques, allow astronomers to mitigate the blurring of ground-based astronomical observations by the atmosphere of Earth [1,2]. The first systems coupled optical lasers with infrared astronomical instruments, for which the adaptative optics corrections are less demanding [3,4]. The integral field spectrograph *Multi-Unit Spectroscopic Explorer* (MUSE) [5] is mounted on the Unit Telescope 4 (UT4) of the European Southern Observatory's (ESO) Very Large Telescope (VLT) at the observatory of Cerro Paranal. It has been one of the

very first astronomical instruments operating at visible wavelengths to be paired with an optical laser guide-star system: the four-laser guide-star facility (4LGSF) [6], which is part of UT4's Adaptive Optics Facility (AOF) [7].

The fact that Rayleigh- and Mie-scattered laser guide-star photons can contaminate astronomical observations is well known by the astronomical community [8–12]. It is the combination of MUSE with the 4LGSF that first revealed that astronomical observations can also be contaminated by Raman-scattered laser guide-star photons [13]. Specifically, inelastic Raman scattering physics implies that the excitation of the first vibrational mode $\nu_{1\leftarrow 0}$ of the most abundant air molecules (N_2 and O_2) already redshifts laser guide-star photons by up to $2700 \text{ cm}^{-1} \approx 1000 \text{ Å}$. In the wake of its observation at the VLT, this *Raman signal* was also reported at other professional astronomical observatories [14–17], and a series of specific follow-up observations were undertaken at Cerro Paranal to characterize it. These observations revealed that in the case of UT4 and the off-axis launch configuration of the 4LGSF, dust particles on the primary telescope mirror are

*frederic.vogt@alumni.anu.edu.au; <https://fpavogt.github.io>

primarily responsible for redirecting Raman-scattered laser photons inside the MUSE field-of-view [18].

Inserting notch filter(s) in the optical path of affected astronomical instruments—to block the contaminating Raman-scattered photons—would drastically reduce the spectral coverage (and thus the scientific usefulness) of these instruments. While this choice could remain meaningful for narrow-wavelength or low-resolution spectrographs, it does not make sense for most spectrographs used by the astronomical community. Specific measures (e.g., keeping the telescope optics as clean as possible, see [18]) can be taken to mitigate the impact of the contamination. In practice, instruments contaminated (at any level) by Raman-scattered photons—be they emitted by their own supporting laser guide-star systems, or by a nearby one at dense observing sites—will inevitably require their data to be cleaned-up in a dedicated postprocessing step. For example, a *Raman cleanup* step is now part of the official MUSE data reduction pipeline [19]. The necessity of such a step for the data reduction pipeline of HARMONI [20], a first generation instrument of ESO’s Extremely Large Telescope [21], is currently being assessed (J. Richard, private communication). Removing the Raman signal from contaminated data requires, in part, a detailed catalog of molecular transitions and associated Raman shifts. Such a catalog would benefit any science case requiring high spectral fidelity, provided that it is accurate enough.

The Raman signature of the most abundant air molecules is comprised of a series of dense line forests with intensity variations of several orders of magnitude. A higher-resolution spectrograph and/or better signal-to-noise observation will thus reveal a more spectrally complex Raman signal. This fact becomes evident when comparing, for example, the observations from the MUSE, FORS2 [22], and *Échelle Spectrograph for Rocky Exoplanets and Stable Spectroscopic Observations* (ESPRESSO) [23–25] instruments (with respective spectral resolutions $R = \lambda/\Delta\lambda$ of ~ 2500 , ~ 2900 , and ~ 140000) of the $v_1 \leftarrow 0$ rotational-vibrational forests for the $^{14}\text{N}^{14}\text{N}$ and $^{16}\text{O}^{16}\text{O}$ molecules [13,26]. It was thus suggested that Raman-scattered laser photons could also have positive uses for astronomical observatories: for example, to characterize the spectral accuracy of astronomical spectrographs via the exact same light path as science photons [26], a feat unattainable with traditional calibration sources.

In this article, we present the deepest (i.e., highest signal-to-noise) and most accurate spectrum of the pure-rotational and rotational-vibrational spectrum of the atmosphere recorded with an astronomical spectrograph to date. This spectrum, acquired with ESPRESSO, is intended to provide astronomers with an exhaustive catalog of Raman lines, associated to the most abundant air molecules, that can contaminate their observations.

The article is structured as follows. We provide an exhaustive description of our nonstandard observations in Sec. II, including our data acquisition and reduction procedures. The molecular lines visible in the resulting spectrum are discussed in Sec. III A. The discovery of distinct lasing wavelengths for the different laser beams of the 4LGSF is presented in Sec. III B. We summarize our conclusions in Sec. IV. All wavelengths are quoted in vacuum. Throughout the article, we express laser photon energies and energy differences in

different units (\AA , fm, cm^{-1} , m s^{-1} , Hz) following the usual practices of the applicable subfield (astrophysics, molecular physics, or laser physics). Unless specified otherwise, the conversion between these units is made with respect to $\lambda_* = 5891.59120 \text{ \AA}$. We refer to N as the end-over-end rotational quantum number of a given molecule, and J its total angular momentum quantum number. We follow the usual molecular branch-naming conventions with $O \equiv (\Delta J = -2)$, $P \equiv (\Delta J = -1)$, $Q \equiv (\Delta J = 0)$, $R \equiv (\Delta J = +1)$ and $S \equiv (\Delta J = +2)$.

II. OBSERVATIONS

A. Atmospheric conditions

The data presented in this article were acquired in ESO’s period 104 under the calibration Program Id. 4104.L-0074(A) (P.I.: Vogt), for which a total of 24 h of dark time with ESPRESSO on VLT UT4 were awarded. The observations took place between 21 October 2019 and 27 October 2019 (included), specifically between the half-night mark and the rise of the Moon in the East. All the observations were performed under CLEAR [27] sky conditions, with no visible clouds reported by the observatory’s weather officer. We present in Fig. 1 the horizontal wind speed $\|\vec{w}\|$ and azimuth $\phi_{\vec{w}}$ above Cerro Paranal over the course of the entire observing run, derived from the ERA5 reanalysis dataset from the European Center for Medium-Range Weather Forecast (ECMWF) [28]. Specifically, we used the Python library `cdsapi` [29] to request ERA5 reanalysis wind information for 37 pressure levels interpolated at the location of Cerro Paranal (24.62684° South, 70.40453° West) over the duration of the observing run. We converted the geopotential height h of every data point to geometrical altitudes above mean sea level (amsl) H via the following ECMWF prescription applicable to ERA5 products in the GRIB-1 data format,

$$H = R_e \frac{h}{R_e - h} \quad (1)$$

with $R_e = 6367.47 \text{ km}$.

The wind speed at ground level never reached more than 10 m s^{-1} during the observations. At high altitudes, a persistent jet stream current coming from the West was present at an altitude of 12–15 km amsl every night of the observing run, with horizontal speeds in the range of 20–40 m s^{-1} that are typical for this geographical location [30].

B. Data acquisition

The performed observations were highly nonstandard: they targeted the four up-link laser beams of the 4LGSF laser guide-star system of UT4, which ESPRESSO is not intended/optimized to exploit for Adaptive Optics purposes (ESPRESSO is optimized for seeing-limited observations). These observations were made possible, in large, thanks to the Laser Pointing Camera (LPC) [31,32], which allows the telescope operator to use the laser guide-star system independently from the astronomical instrument. Since ESPRESSO is entirely oblivious to the 4LGSF, no information regarding the status of the laser guide-star system is recorded in the header of the ESPRESSO raw data files. This information was thus

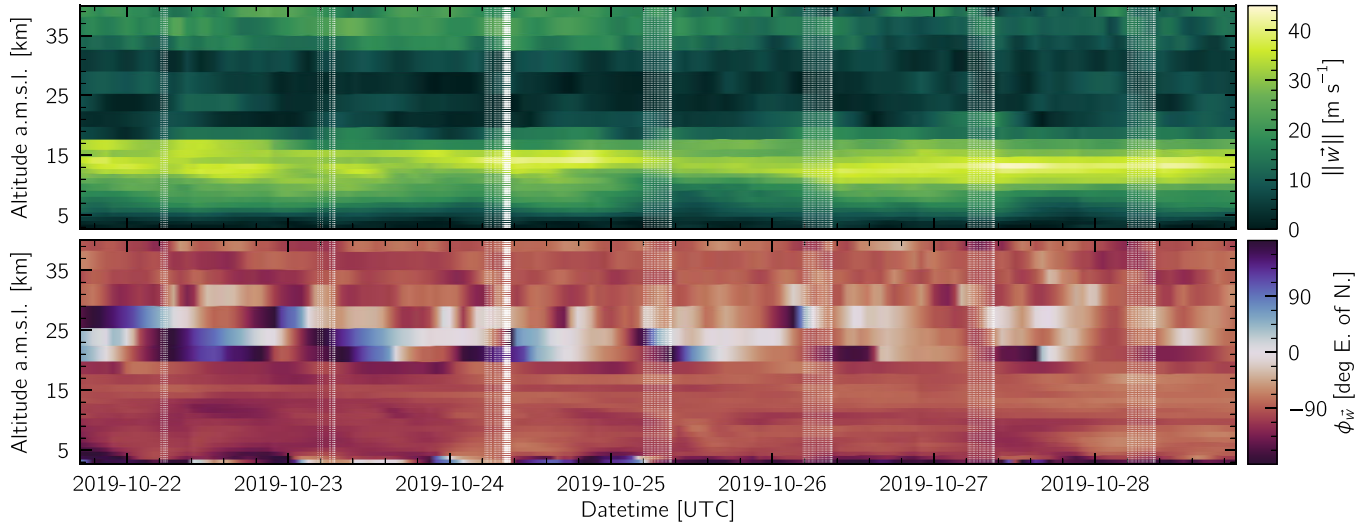


FIG. 1. Top: Horizontal wind speed $\|\vec{w}\|$ above Cerro Paranal over the course of the ESPRESSO observing run 4104.L-0074(A), derived from the ECMWF ERA5 reanalysis dataset. The altitude axis is cropped at the altitude of UT4 (2648 m amsl). The white vertical lines denote the start of every 175 ESPRESSO exposures acquired over the course of the observing run. Bottom: Idem, but for the wind azimuth $\phi_{\vec{w}}$ in degrees East of North (0° ≡ wind coming from the North; 90° ≡ wind coming from the East). These stable conditions with dominant winds from the West are typical of this geographical location.

recorded manually for each of the 175 exposures acquired during the observing run. We provide it in Table IV in the Appendix B, to enable reanalysis by interested readers.

All our observations used the singleHR mode of ESPRESSO with the 2x1_SLOW detector readout mode. At the time, this provided the largest on-sky collecting fiber (1 arcsec diameter on-sky) and lowest associated read-out noise [33]. We targeted empty fields with no entries in the GAIA [34] Data Release 2 [35] and USNO-B2 [36] catalogues within a radius of 10 arcsec. This ensures a homogeneous background with a V magnitude of ~ 21 or higher [37] for our observations. The targeted fields are located in the declination range $-35^\circ \lesssim \text{Dec.} \lesssim -40^\circ$ to minimize the speed of the field rotation when crossing the meridian. The majority of the observations were made at R.A.: $04^{\text{h}}00^{\text{m}}29^{\text{s}}$; Dec.: $-39^\circ 52' 30''$. This field could be tracked continuously during our observing half-nights, which allowed to maximize the time spent on-source while systematically remaining in the telescope elevation range of $55^\circ - 75^\circ$.

All observations were performed with the telescope strongly defocused. This allowed to spatially concentrate the emission from the laser beams that (unlike astronomical targets) are not located at “infinity”. The defocus was achieved by offsetting the secondary telescope mirror by +10 mm from its nominal position. No active optics corrections can be applied to the primary mirror of a defocused Unit Telescope at the VLT [38,39]. Yet, as the telescope tracks, it remains important to account for the changing gravity vector to maintain a good image quality. We thus manually triggered (after temporarily refocusing the telescope at infinity to detect stars in the field) several active optics correction cycles for the primary mirror every hour.

In regular operations, the ESPRESSO instrument provides an automated secondary field stabilization. This helps maximize light collection and ensure an homogeneous illumination of the fiber(s) during integration. This automated image stabi-

lization is performed on the science target with a technical CCD (TCCD) [40], and complements the primary field stabilization performed by the telescope using a guide-star. For our observations, the field stabilization from both the telescope and ESPRESSO were disabled. The former because of the strong defocus of the telescope, and the latter because of the spatially-extended nature of the up-link laser beams.

The narrowest (≡ in focus) part of the 4LGSF laser beams were moved, one-at-a-time, to the on-sky location of the ESPRESSO fiber “A” as part of the acquisition sequence (see Fig. 2). A smooth drift of the laser beams over time required small readjustments of their positions with respect to the fiber every ~ 20 min. This drift, and the regular manual corrections performed sequentially for each laser beam, lead to:

(1) fluctuations in the observed flux of the Raman lines of up to a factor of 2 amongst the different exposures from fiber A, and

(2) a time-varying mixing ratio between the fluxes of the individual laser guide-star units (LGSUs) over both ESPRESSO fibers.

For legacy and reproducibility purposes, our detailed acquisition sequence is included in Appendix A. In every exposure, the fibre “B” of ESPRESSO was open to the sky. Its orientation is fixed with respect to fiber A in the image plane. Given the fact that ESPRESSO does not have a field derotator, fibre B did not always collect light from the same area (≡ height) of the laser beams, which are fixed in the Altitude-Azimuth frame of the telescope.

The observations are comprised of four main sets of exposures:

(i) set 1: 92×600 s exposures acquired with the four LGSUs propagating, intended to assemble the deep spectrum of the pure-rotational and rotational-vibrational Raman signature of air.

(ii) set 2: 3×1200 s exposures with no laser propagation, to assemble a sky reference spectrum.

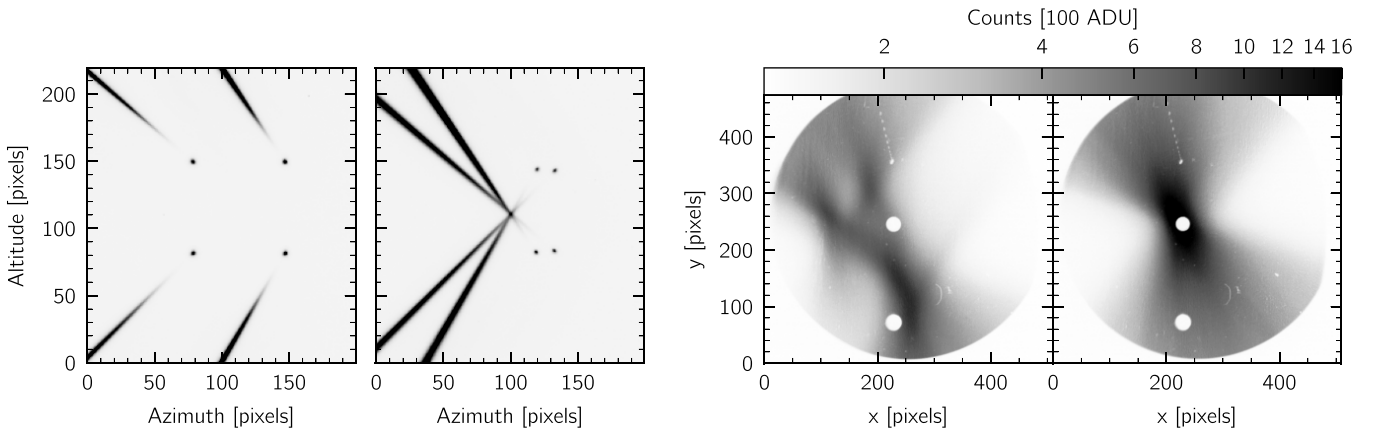


FIG. 2. Left: LPC images of the 4LGSF up-link laser beams and associated guide-stars in (1) the nominal *Wide-Field-Mode* asterism and (2) after manual centering of the beams onto the ESPRESSO fiber. The slanted perspective is a consequence of the off-axis position of the LPC, mounted on the top ring of UT4. Right: ESPRESSO TCCD view of the up-link laser beams before and after the finer alignment onto the ESPRESSO fiber A (central white dot, 1 arcsec in diameter). Prior to the fine tuning, the individual patterns from the four beams is distinguishable, with their narrowest part corresponding to the distance in-focus (~ 21.5 km along the line-of-sight, see Sec. II C). The strong spatial dependence of the observed beams' width is a direct consequence of the launch configuration for the 4LGSF lasers. This implies that the return flux seen by ESPRESSO is strongly sensitive to the fine alignment of the laser beams over the ESPRESSO fibers. The second white dot towards the bottom of the TCCD images corresponds to fiber B.

(iii) set 3: $1 \times 4 \times 300$ s and $6 \times 4 \times 120$ s exposures, a series of quadruplet exposures acquired at the end of each half night to assess the spectral consistency of the different LGSUs. For each quadruplet (one per night), we cycled through all four LGSUs sequentially, enabling a single beam per exposure.

(iv) set 4: 11×1 s exposures with only 1 laser beam (LGSU3) propagating, and an additional telescope focus offset of $+1$ mm (for a total focus offset of $+11$ mm). They are meant to assemble an unsaturated spectrum of the main laser line.

All the other exposures listed in Table IV that do not belong to any of these four sets were used for alignment, adjustment, and fine-tuning purposes.

With the exception of the night of 21 October 2019, a set of manual laser frequency comb (LFC) wavelength calibrations were triggered immediately before the start of the observations. Together with the daily calibrations triggered immediately after the end of the nights, these ensure than no scientific exposure was acquired more than ~ 2.5 hr apart from an LFC reference calibration exposure. LFCs are state-of-the-art, extremely precise and accurate wavelength calibration sources [41–43]. These devices can generate dense forests of narrow lines with even intensities and a uniform line spacing, that can be matched to the resolution and wavelength range of high-resolution spectrographs like ESPRESSO. The frequencies of the LFC lines can be locked to an atomic clock, ensuring a precision and accuracy of up to one part in 10^{11} . At the time of our observations, ESPRESSO's LFC was formally under commissioning, but nonetheless operational.

C. Sampled altitude range

We do not have a direct measure of the altitude at which the recorded Raman signal originated. However, we can obtain an estimate of the distance (along the line-of-sight) that is

in-focus during the observations from basic telescope optics. UT4 has an effective focal length $f_{\text{eff}} = 121.561$ m. Its secondary mirror has a radius of curvature $r = 4553.1$ mm [44]. According to the VLT optical layout, the Nasmyth focus lies $a = 9896 + 6800 = 16696$ mm away from the surface of the secondary mirror. Treating the secondary mirror as a spherical rather than hyperbolic surface (for the sake of simplicity) implies that the virtual focal plane of the primary mirror lies $a' \approx ra/(r + 2a) = 2003$ mm behind the surface of its secondary mirror [45]. When the telescope is focused at infinity, the image is formed at a distance $l = f_{\text{eff}}$. Offsetting the secondary mirror by $\Delta x = +10$ mm changes the effective focal length of the telescope to

$$f_{\text{eff}}^* = f_{\text{eff}} \cdot \frac{a'}{a} \cdot \frac{a + \Delta x}{a' - \Delta x} = 122.24 \text{ m.} \quad (2)$$

The camera being fixed, its distance l along the optical path translates to an object plane located at a distance D along the line-of-sight given by

$$D = \left(\frac{1}{f_{\text{eff}}^*} - \frac{1}{l} \right)^{-1} = 21.8 \text{ km.} \quad (3)$$

This analytical estimate was verified using a complete model of UT4, its Coudé train [46], and the ESPRESSO instrument, implemented in a state-of-the-art ray-tracing optical design software. Offsetting the secondary mirror by $+10$ mm in the model placed the object plane at a distance of $D = 21.5$ km along the line-of-sight (A. Cabral, private communication). For a given UT4 pointing altitude ψ , this corresponds to a geometric altitude above mean sea level $H_{\text{obs}} = D \sin \psi + H_{\text{UT4}}$ with $H_{\text{UT4}} = 2.648$ km. The median value of H_{obs} for the set 1 exposures is 23.0 km amsl.

The finite aperture size of the ESPRESSO fibers (1 arcsec in diameter) coupled to the slow, regularly-and-manually-corrected drift of the laser beams imply that emission from a

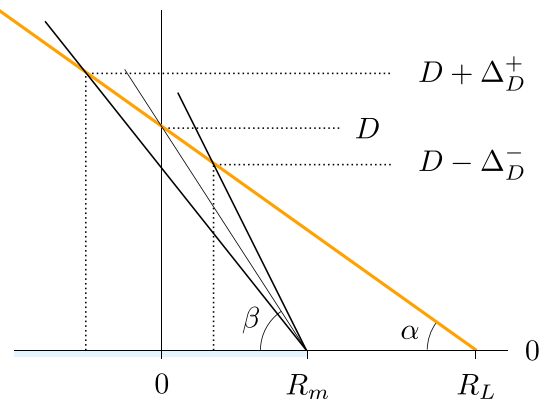


FIG. 3. Simple schematic of the UT4 primary mirror (with a diameter R_m) and one 4LGSF laser beam (not to scale). The telescope is assumed to be focused at a distance D along the line-of-sight. The finite aperture size of the ESPRESSO fibers and the slow, regularly-and-manually-corrected drift of the laser beams imply that emission from a range of distances along the line-of-sight will be collected. The maximum range limits Δ_D^- and Δ_D^+ are set by the optical paths passing closest (when hitting the UT4 mirror) from the laser launch telescopes.

range of distances $[D - \Delta_D^-; D + \Delta_D^+]$ along the line-of-sight will be sampled in the observations. We estimate this range using the simple model depicted in Fig. 3, with $R_m = 4.1$ m the radius of the UT4 primary mirror, and $R_L = 5.51$ m the distance between the optical axis of UT4 and the location where the 4LGSF laser beams would cross the mirror plane (if extended backward from the launch telescopes, see the Appendix in [13]). The maximum range of distances sampled by the ESPRESSO fiber A, when focused at a distance D along the line-of-sight, is set by the optical paths passing the closest to any of the four LGSUs' launch telescopes. From basic trigonometry, given a fiber diameter of 1 arcsec on-sky and an estimated motion of the laser beams up to ~ 1 arcsec beyond this diameter, we have

$$D \pm \Delta_D^\pm = \frac{(R_L - R_m) \tan \alpha \tan \beta^\mp}{\tan \beta^\mp - \tan \alpha} \quad (4)$$

with $\tan \alpha = D/R_L$, $\beta^\mp = \beta \mp 1.5$ arcsec, and $\tan \beta = D/R_m$. With a telescope focus set at $D = 21.5$ km, we thus estimate that $\Delta_D^- \approx 2.2$ km and $\Delta_D^+ \approx 2.7$ km, such that the range of observed distances along the line-of-sight in the data is [19.3 km; 24.2 km]. The corresponding geometric altitude range for every ESPRESSO exposure acquired during the observing run is presented in Fig. 9: it lies systematically within the interval [18 km; 26 km] amsl.

D. 4LGSF state

All four LGSUs of the 4LGSF were used in their nominal mode for the majority of the exposures acquired during the observing run. In this mode, the emitted light is comprised of 18 W in a central component designed to excite the D_{2a} sodium transition, and 2×2 W in symmetric sidelines located ± 1.713 GHz on either side [26]. The lower-energy sideline is designed to excite the D_{2b} sodium line, and to recover atoms lost to the $3^2S_{1/2} F = 1$ state [47].

The 4LGSF 589 nm \approx 509 THz laser sources (one per LGSU) are based on a frequency-doubled fibre amplifier. The output emission wavelength of the 1178 nm \approx 255 THz master oscillators (seed lasers) of the 589-nm laser sources are actively stabilized to twice the sodium resonance wavelength via wavelength meters (one per LGSU) with a specified accuracy of better than ± 10 MHz [48]. The wavelength meters exhibit a passive stability of about 80 kHz h^{-1} (linear drift). The absolute accuracy of the wavelength meters is guaranteed by periodical calibrations against iodine-referenced helium-neon lasers (one per LGSU), which themselves have a specified absolute accuracy of better than ± 5 MHz. The feedback loop, which stabilizes the seed lasers to the wavelength meters is another factor contributing to the actual LGSUs emission wavelengths. This feedback loop has an accuracy of about ± 5 MHz at 1178 nm, which was determined during the development of the laser sources.

The four wavelength meters were calibrated every afternoon before our observing nights. However, it must be noted that the 4LGSF system was rebooted during the first half of night 6 (i.e. after the afternoon wavelength meter calibrations were executed), and no new wavelength meter calibrations could be executed before the start of the ESPRESSO observations.

For a handful of exposures, one or more of the four LGSUs were detuned for test purposes. The detuning of each LGSU is configured in the laser control software. When detuned, LGSU1, LGSU2, and LGSU4 wavelengths are (blue)shifted by +5.960 GHz at 589 nm; LGSU3 is (red)shifted by -11.057 GHz at 589 nm. These exposures will not be discussed in this article, but they are clearly identified in Table IV.

E. Saturation-induced artefacts

The strength of the Raman lines is several orders of magnitude (≥ 3) fainter than the strength of the main laser line resulting from elastic Mie and Rayleigh backscattering. For an optical CCD like that of ESPRESSO with a range of $\sim 65\,000$ ADU mounted on a telescope with a collecting area 8 m in diameter, the main laser line already saturates in exposures as short as 1 s (with the beam in focus). For the significantly-fainter Raman lines, on the other hand, the longer the ESPRESSO exposures are, the stronger the signal-to-noise ratio of the lines, and the more efficient the observations.

The use of 600 s exposures for our observations is the result of the trade-off between (a) the need to enhance the signal-to-noise ratio of the Raman lines in individual exposures, and (b) limit the total number of individual exposures to minimize the read-out overheads, while (c) maintaining the degree of saturation bleeds and ghosts on the ESPRESSO CCD within reason. In 600 s, the saturation of the main laser line on the red ESPRESSO CCD is severe nonetheless, as illustrated in Fig. 4. Blooming from the saturated pixels strongly contaminates pixels immediately above and below the main laser line, such that this entire spectral order is effectively lost. Other artefacts caused by the strength of the main laser line include:

- (i) bright trails due to charge transfer inefficiency,
- (ii) an artificial continuum in the vicinity of the main laser line,

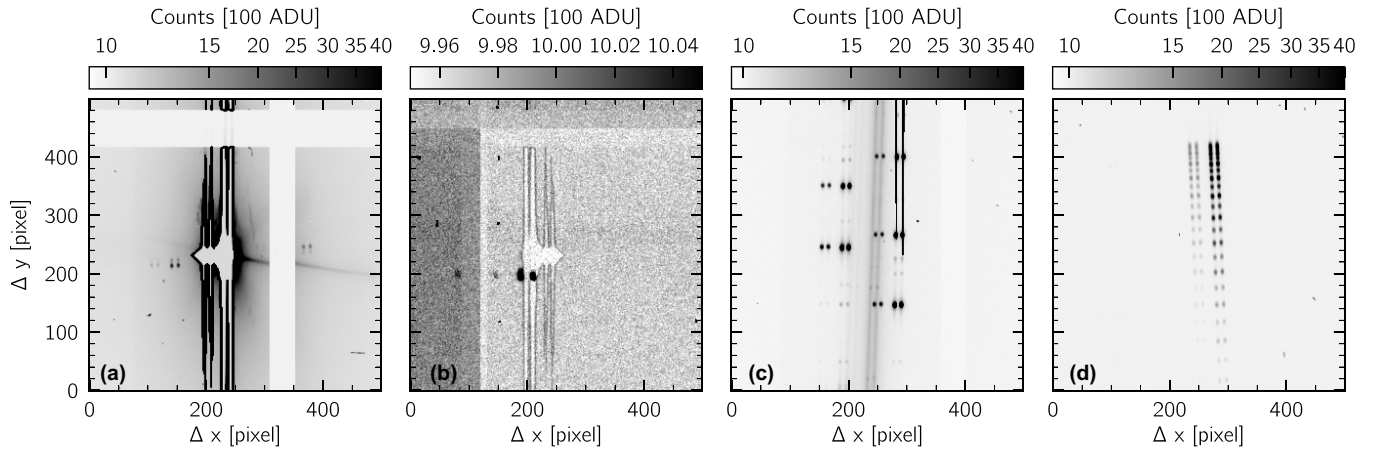


FIG. 4. Subsections of a single **set 1**, 600 s ESPRESSO raw exposure from the red CCD. (a) Region of the main laser line, saturated. Strong blooming (with electrons leaking vertically across the detector) is evident, rendering this specific order un-exploitable. (b) Other regions of the detector display ghost images of the saturated region, but significantly closer to the noise level. (c) In the vicinity of the main laser line, pure rotational Raman lines (black dots) are also being contaminated by an artificial continuum emission (middle-grey emission) in addition to the blooming from the main laser line (vertical black stripes). (d) Most areas of the red detector are free from strong artefacts, but remain subject to an elevated, smooth background signal: for example, the region of the $\nu_{1 \leftarrow 0}$ rotational-vibrational Q branch of the $^{14}\text{N}^{14}\text{N}$ molecule shown here.

- (iii) ghost images of the saturated regions caused by internal reflections, and
- (iv) a higher background for the entire red CCD, illuminated by scattered light.

The exquisite stability of the ESPRESSO instrument implies that all these artefacts do not vary between exposures, except for their respective brightness, which is tied to the incoming laser flux.

F. Data reduction

The raw data were downloaded from the ESO Science Archive Facility and reduced using the ESPRESSO pipeline v2.0.0 [25] via the ESOREFLEX v2.11.0 environment [49]. The data processing consisted of (1) bias and dark subtraction, (2) optimal extraction of spectral orders and creation of extracted spectra (S2D), and (3) wavelength calibration of S2D spectra using the LFC. Subtraction of the interorder background was turned off, because it led to suboptimal results due to the strong bleeding of the saturated laser line. We use the reduced S1D spectra from fibre A in the subsequent analysis, for which we systematically remove the barycentric Earth radial velocity (stored under the keyword HIERARCH ESO QC BERV in the ESPRESSO FITS files) correction applied by default by the ESPRESSO pipeline via

$$\lambda = \lambda_{\text{raw}} \left[(1 + 1.55 \times 10^{-8}) \left(1 + \frac{\text{BERV}}{299792.458} \right) \right]^{-1}. \quad (5)$$

The 15.3-hr-deep ESPRESSO spectrum of the pure-rotational and rotational-vibrational Raman signature of our atmosphere at an altitude of ~ 23 km amsl is assembled using the **set 1** (92×600 s), resampled, blaze-corrected, one-dimensional spectra from fibre A, in units of photoelectrons. These exposures are stacked together on a common wavelength grid using a flux weighted-average combination scheme. This choice is motivated by the fluctuations of the

laser line fluxes between the different exposures (up to a factor ~ 2 , see Sec. II B).

The spectral regions $5880.8 \text{ \AA} < \lambda < 5899.5 \text{ \AA}$ and $5875.1 \text{ \AA} < \lambda < 5875.8 \text{ \AA}$, are strongly affected by the blooming of the main laser line. They are replaced with the (scaled) weighted-average spectrum assembled from the **set 4** (11×1 s) exposures that show no saturation. The resulting, combined spectrum ranges from $3775 \text{ \AA} \approx +9517 \text{ cm}^{-1}$ to $7895 \text{ \AA} \approx -4307 \text{ cm}^{-1}$. In the assembly process, no correction of the estimated spectral shift induced by wind (see Sec. III B) is being applied to the individual exposures. These spectral shifts have amplitudes $< 20 \text{ m s}^{-1} \approx 40 \text{ fm}$. This corresponds to $\lesssim 5\%$ of the Raman line widths, which are dominated by thermal broadening. Wind-induced spectral shifts thus does not limit our ability to identify individual molecular transitions in the resulting deep ESPRESSO spectrum.

III. RESULTS

A. The Raman signature of the atmosphere at $H_{\text{obs}} = 23$ km

The 15.3-hr-deep ESPRESSO spectrum revealing the pure-rotational and rotational-vibrational Raman spectrum of the atmosphere at $H_{\text{obs}} = 23$ km is shown in Fig. 5. The main laser line at $\Delta\nu = 0$ is clearly visible, together with the three forests of:

- (1) pure-rotational Raman lines in its immediate vicinity,
- (2) $\nu_{1 \leftarrow 0}$ rotational-vibrational Raman lines associated with the O_2 molecule at $\sim 6490 \text{ \AA}$, and
- (3) $\nu_{1 \leftarrow 0}$ rotational-vibrational Raman lines associated with the N_2 molecule at $\sim 6830 \text{ \AA}$.

A careful comparison with the reference sky spectrum reveals $\nu_{2 \leftarrow 0}$ rotational-vibrational Q-branch lines from $^{16}\text{O}^{16}\text{O}$ at $\lambda_{\text{vac}} \cong 7202 \text{ \AA}$, and vibrational lines from $^{12}\text{C}^{16}\text{O}^{16}\text{O}$ at $\sim 6366.1 \text{ \AA}$, $\sim 6374.3 \text{ \AA}$, $\sim 6416.4 \text{ \AA}$, and $\sim 6425.1 \text{ \AA}$ [50]. The $\nu_{2 \leftarrow 0}$ rotational-vibrational forest from $^{14}\text{N}^{14}\text{N}$ at $\Delta\nu \approx -4631.2 \text{ cm}^{-1} \approx 8100 \text{ \AA}$ (that can be detected with MUSE)

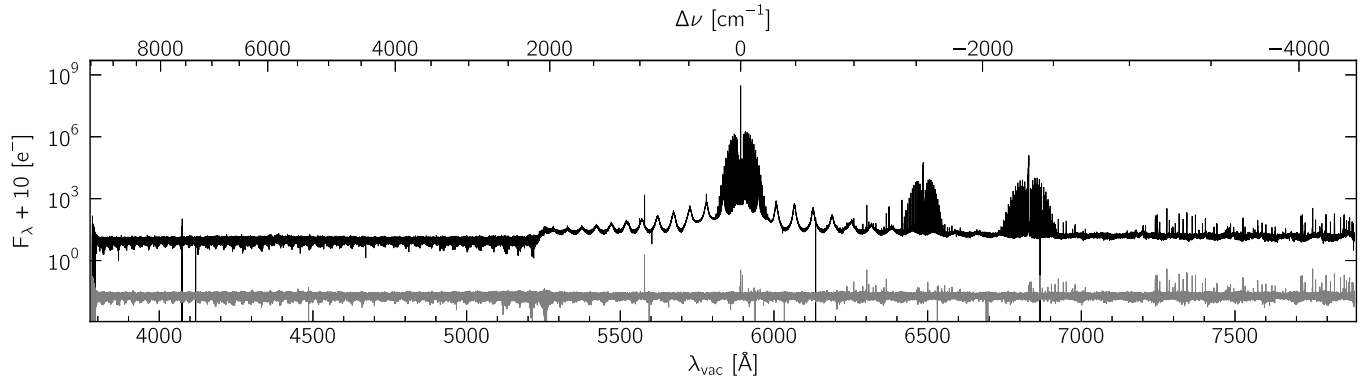


FIG. 5. Weighted-average of 92×600 s ESPRESSO exposures (set 1) of the four 4LGSF laser beams (black), with the strongly saturated regions $5880.8 \text{ \AA} < \lambda < 5899.5 \text{ \AA}$ and $5875.1 \text{ \AA} < \lambda < 5875.8 \text{ \AA}$ replaced by a (scaled) weighted-average combination of 11×1 s exposures (set 4). The reference sky spectrum assembled from 3×1200 s exposures (set 2), artificially scaled and shifted for visualization purposes, is shown in grey. The forest of pure rotational Raman lines immediately surrounding the main laser line is clearly visible, together with the $\nu_1 \leftrightarrow 0$ rotational-vibrational Raman forests associated to the O₂ (at $\sim 6485 \text{ \AA} \approx -1550 \text{ cm}^{-1}$) and N₂ (at $\sim 6825 \text{ \AA} \approx -2320 \text{ cm}^{-1}$) molecules. The jump between the blue and red CCD spectra and the extended oscillatory pattern surrounding the main laser line, clearly visible in this logarithmic view, are artefacts caused by the saturation of the main laser line.

[13]) is located beyond the spectral range of ESPRESSO. The complete list of 865 Raman lines (pure-rotational: 511; rotational-vibrational: 354) identified in the spectrum is presented in Table V in the Appendix C, and accessible electronically as a VizieR [51] catalog [52]. Several of the artefacts caused by the strong saturation of the main laser line are also readily visible in the logarithmic-scale diagram presented in Fig. 5. These include the artificial continuum with an oscillatory-like pattern, and the nonzero background illumination red-wards of $5250 \text{ \AA} \approx +2075 \text{ cm}^{-1}$.

A handful of emission line-like features remain unidentified at this stage. These include, in particular, 22 features located within $\pm 56 \text{ \AA}$ of the main laser line, a subset of which at least appear to be distributed symmetrically (in the Raman shift space) around the main laser line. This could suggest a molecular origin. A careful inspection of the raw ESPRESSO exposures also suggests that these lines are real. However, the complex and diverse nature of the artefacts caused by the strong saturation of the main laser line forbids us from stating with certainty that these 22 unidentified features are not artefacts themselves. Doing so will require a precise match of these features (listed in Table I) with specific molecular transitions, which elude us so far.

1. Pure-rotational Raman lines

Figure 6 presents a detailed view of the spectral region within $\pm 56 \text{ \AA}$ ($\approx \pm 160 \text{ cm}^{-1}$) of the main laser line, which reveals the densest part of the pure-rotational Raman line forest. Molecular lines associated to the most abundant molecules of air, including their isotopes, are clearly detected. These include: ¹⁴N ¹⁴N, ¹⁴N ¹⁵N, ¹⁶O ¹⁶O, ¹⁶O ¹⁷O, ¹⁶O ¹⁸O, and ¹²C ¹⁶O ¹⁶O, for which we identify 511 pure-rotational lines altogether, over the spectral range $[+250 \text{ cm}^{-1}; -265 \text{ cm}^{-1}] \approx [5806 \text{ \AA}; 5985 \text{ \AA}]$. By comparison, the notch filters of MUSE (one per adaptive optics observing mode) are blocking a spectral range of:

- (i) $\approx [5800 \text{ \AA}; 5970 \text{ \AA}]$ in WFM-AO-N mode,
- (ii) $\approx [5750 \text{ \AA}; 6010 \text{ \AA}]$ in WFM-AO-E mode, and
- (iii) $\approx [5780 \text{ \AA}; 6050 \text{ \AA}]$ in NFM-AO-N mode [19].

It was identified during the commissioning of ESPRESSO that the spectral resolution of this instrument is sufficient to resolve the fine-structure Raman lines from ¹⁶O ¹⁶O [26], which has a ³S electronic ground state [53]. This implies that unlike ¹⁴N ¹⁴N, treating the ¹⁶O ¹⁶O molecule as a nonrigid diatomic rotator is not sufficient to identify all its Raman lines present in the 15.3-hr-deep ESPRESSO spectrum. Instead, we rely on an extensive Hamiltonian model constrained by microwave, THz, infrared, visible, and ultraviolet transitions of all six oxygen isotopologues to do so [54–56]. The specific pure-rotational line sets visible for the ¹⁶O ¹⁶O, ¹⁶O ¹⁷O, and ¹⁶O ¹⁸O molecules, identified using this model, are listed in Table II (see Appendix C for details).

TABLE I. Un-indentified emission line-like features located within $\pm 160 \text{ cm}^{-1}$ of the main laser line at $\Delta\nu = 0$ in the 15.3-hr-deep ESPRESSO spectrum of the 4LGSF laser beams. The vacuum wavelengths accuracy is $\sim 0.01 \text{ \AA}$.

λ_{vac} (\AA)	$\Delta\nu$ (cm^{-1})	λ_{vac} (\AA)	$\Delta\nu$ (cm^{-1})
5852.55	+113.23	5901.77	-29.27
5853.89	+109.31	5902.79	-32.20
5856.61	+101.38	5905.55	-40.12
5864.78	+77.59	5910.28	-53.67
5869.73	+63.22	5913.61	-63.20
5877.69	+40.14	5918.64	-77.57
5880.44	+32.19	5924.22	-93.48
5881.47	+29.21	5927.01	-101.43
5886.65	+14.25	5929.78	-109.31
5896.54	-14.25	5931.16	-113.23
5899.74	-23.44	5933.94	-121.13

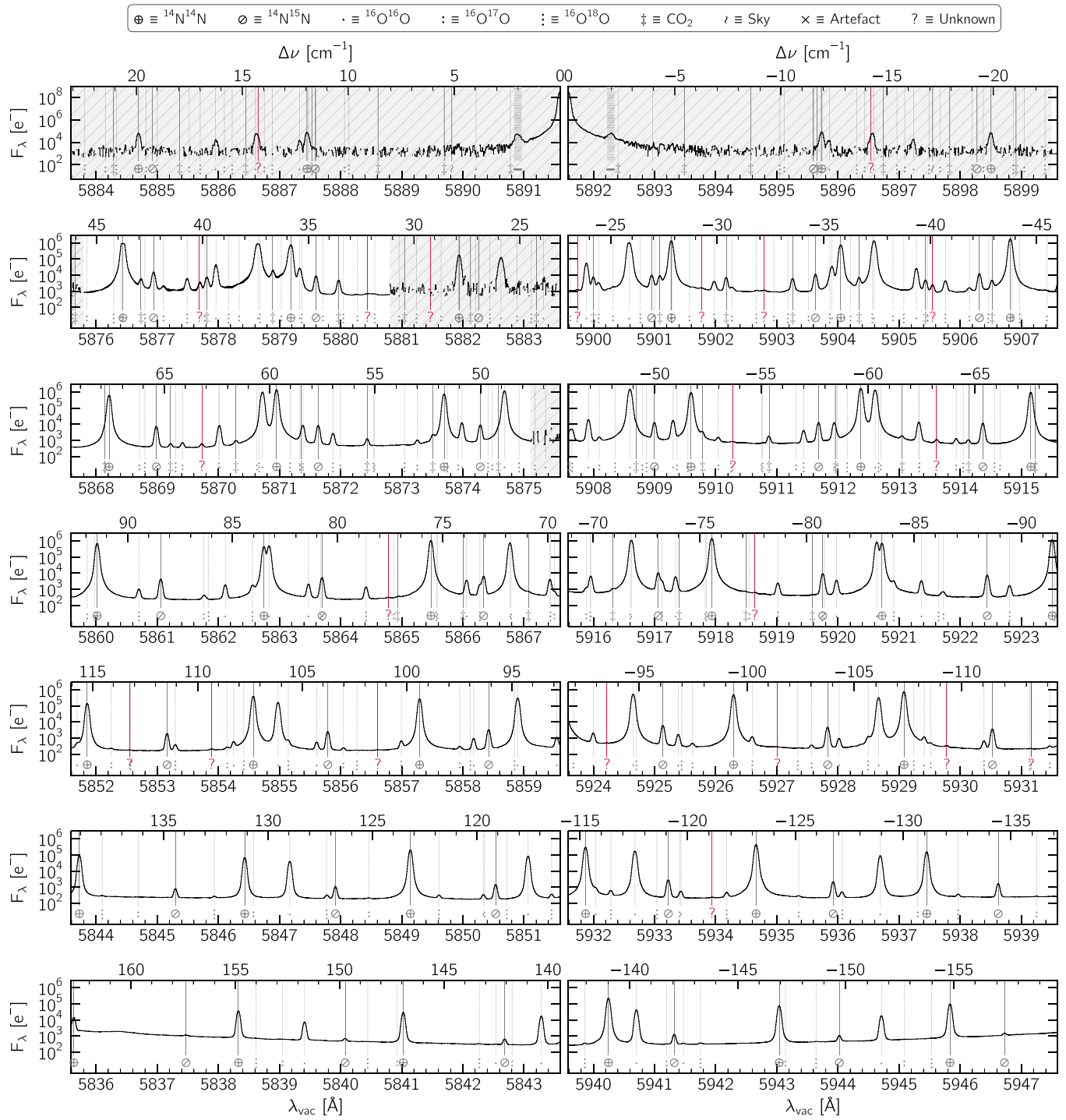


FIG. 6. Pure-rotational Raman spectrum of the atmosphere at an altitude $H_{\text{obs}} = 23$ km, within $\pm 56 \text{ \AA} \approx \mp 160 \text{ cm}^{-1}$ of the main laser wavelength. The spectrum is a weighted-average combination of the set 1 (92×600 s) ESPRESSO exposures. The spectral regions $5880.8 \text{ \AA} < \lambda < 5899.5 \text{ \AA}$ and $5875.1 \text{ \AA} < \lambda < 5875.8 \text{ \AA}$ (highlighted with a dashed-grey background) are assembled from a weighted-average combination of the set 4 (11×1 s) exposures. The theoretical location of pure-rotational transitions from main components of dry air are marked and tagged accordingly (${}^{14}\text{N} {}^{14}\text{N}$: \oplus — ${}^{14}\text{N} {}^{15}\text{N}$: \circ — ${}^{16}\text{O} {}^{16}\text{O}$: \cdot — ${}^{16}\text{O} {}^{17}\text{O}$: $:$ — ${}^{16}\text{O} {}^{18}\text{O}$: \vdash — ${}^{12}\text{C} {}^{16}\text{O} {}^{16}\text{O}$: \ddagger). Sky lines are tagged with the symbol \curlywedge . Artefacts caused by the strong saturation of the main laser line are tagged with the symbol \times . A series of unidentified line-like features, for which a Raman origin is plausible but could not be established, are tagged with red question marks.

2. Vibrational-rotational Raman lines

Figures 7 and 8 present the $\nu_{1 \leftarrow 0}$ rotational-vibrational forests of the O_2 and N_2 molecules, respectively. During the

commissioning of ESPRESSO, only the Q branch of ${}^{16}\text{O} {}^{16}\text{O}$ and ${}^{14}\text{N} {}^{14}\text{N}$ was detected in a single 900 s exposure [26]. The 15.3-hr-deep spectrum reveals, in addition, the Q branch from

TABLE II. Pure-rotational line sets of the $^{16}\text{O}^{16}\text{O}$ molecule and its isotopes identified in the 15.3-hr-deep ESPRESSO spectrum of the 4LGSF laser beams. The maximum value of N up to which the lines of a given set could be identified is specified explicitly.

Molecule	$\Delta^N \Delta J$	(J, N)	max(N)
$^{16}\text{O}^{16}\text{O}$	$^S S$	(N, N)	41
$^{16}\text{O}^{16}\text{O}$	$^S R$	(N, N)	19
$^{16}\text{O}^{16}\text{O}$	$^S R$	($N + 1, N$)	23
$^{16}\text{O}^{16}\text{O}$	$^Q P$	($N + 1, N$)	21
$^{16}\text{O}^{16}\text{O}$	$^Q R$	($N - 1, N$)	21
$^{16}\text{O}^{17}\text{O}$	$^S S$	(N, N)	26
$^{16}\text{O}^{17}\text{O}$	$^S R$	(N, N)	9
$^{16}\text{O}^{17}\text{O}$	$^S R$	($N + 1, N$)	12
$^{16}\text{O}^{18}\text{O}$	$^S S$	(N, N)	27
$^{16}\text{O}^{18}\text{O}$	$^S R$	(N, N)	11
$^{16}\text{O}^{18}\text{O}$	$^S R$	($N + 1, N$)	20

$^{16}\text{O}^{17}\text{O}$, $^{16}\text{O}^{18}\text{O}$, and $^{14}\text{N}^{15}\text{N}$, as well as the O and S branches from $^{16}\text{O}^{16}\text{O}$, $^{16}\text{O}^{18}\text{O}$, $^{14}\text{N}^{14}\text{N}$, and $^{14}\text{N}^{15}\text{N}$.

Rotational-vibrational fine-structure lines related to the $^3\Sigma$ electronic ground state of $^{16}\text{O}^{16}\text{O}$ are detected in all the Q , O , and S branches of this molecule. We list in Table III

the specific sets of rotational-vibrational molecular transitions from the $^{16}\text{O}^{16}\text{O}$ molecule and its isotope that can be identified in the spectrum. For $^{16}\text{O}^{16}\text{O}$, we note that the first lines (corresponding to $N = 1$) of the sets $\Delta N = Q$, $\Delta J = R|P$ are not visible in the ESPRESSO spectrum. This is consistent with these specific transitions having zero intensity [57,58]. We also note that lines from the sets $^S S$ ($N, N - 1$) and $^O O$ ($N, N - 1$) become increasingly blended with lines from the sets $^S S$ (N, N) and $^O O$ (N, N) with increasing N values. The presence of these sets is thus only inferred from their $N = 1$ and $N = 3$ line, respectively [visible in Fig. 7(b)].

B. The 4LGSF lasing wavelengths

It was suggested that Raman lines can be used to assess the spectral accuracy of ESPRESSO (see [26]). Doing so from the combination of 92 individual exposures acquired over seven consecutive nights requires that the Raman signal be spectrally stable over this time span. The presence of wind (i.e., air molecules moving along the observing line-of-sight with respect to the rest frame of UT4) could lead to a varying spectral shift of the observed Raman lines between the different ESPRESSO exposures. A laser photon with frequency ν_* in the rest frame of UT4 will appear Doppler-shifted to a

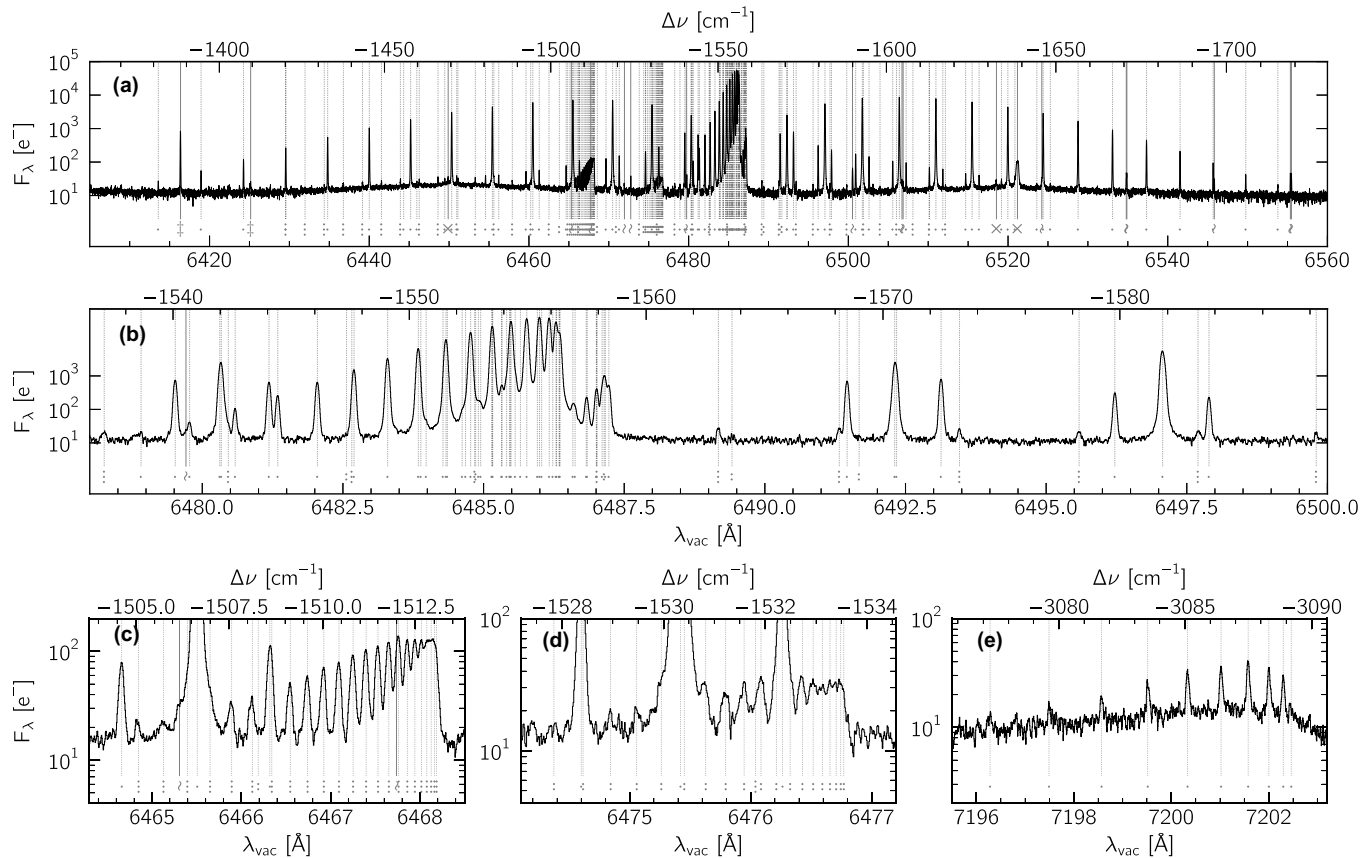


FIG. 7. (a) $\nu_{1 \leftarrow 0}$ vibrational-rotational forest for the $^{16}\text{O}^{16}\text{O}$, $^{16}\text{O}^{17}\text{O}$, and $^{16}\text{O}^{18}\text{O}$ molecules. Two vibrational transitions from $^{12}\text{C}^{16}\text{O}^{16}\text{O}$ are also visible at $\lambda = 6416.4$ Å and 6425.1 Å. (b) Detailed view of the Q-branch for the $^{16}\text{O}^{16}\text{O}$ molecule. The scaled-and-shifted feature at ~ 6487.2 Å is a fine-structure component related to the $^3\Sigma$ electronic ground state of $^{16}\text{O}^{16}\text{O}$, as are the symmetric side lines surrounding the $^S S$ (1, 1) and $^S S$ (3, 3) transitions. (c) Detailed view of the Q branch of the $^{16}\text{O}^{18}\text{O}$ molecule. (d) Detailed view of the Q-branch of the $^{16}\text{O}^{17}\text{O}$ molecule. (e) Detailed view of the $\nu_{2 \leftarrow 0}$ Q branch of the $^{16}\text{O}^{16}\text{O}$ molecule. The theoretical position of individual Raman lines, sky lines, and artefacts are marked using vertical grey lines. Each is tagged using the symbols introduced in Fig. 6.

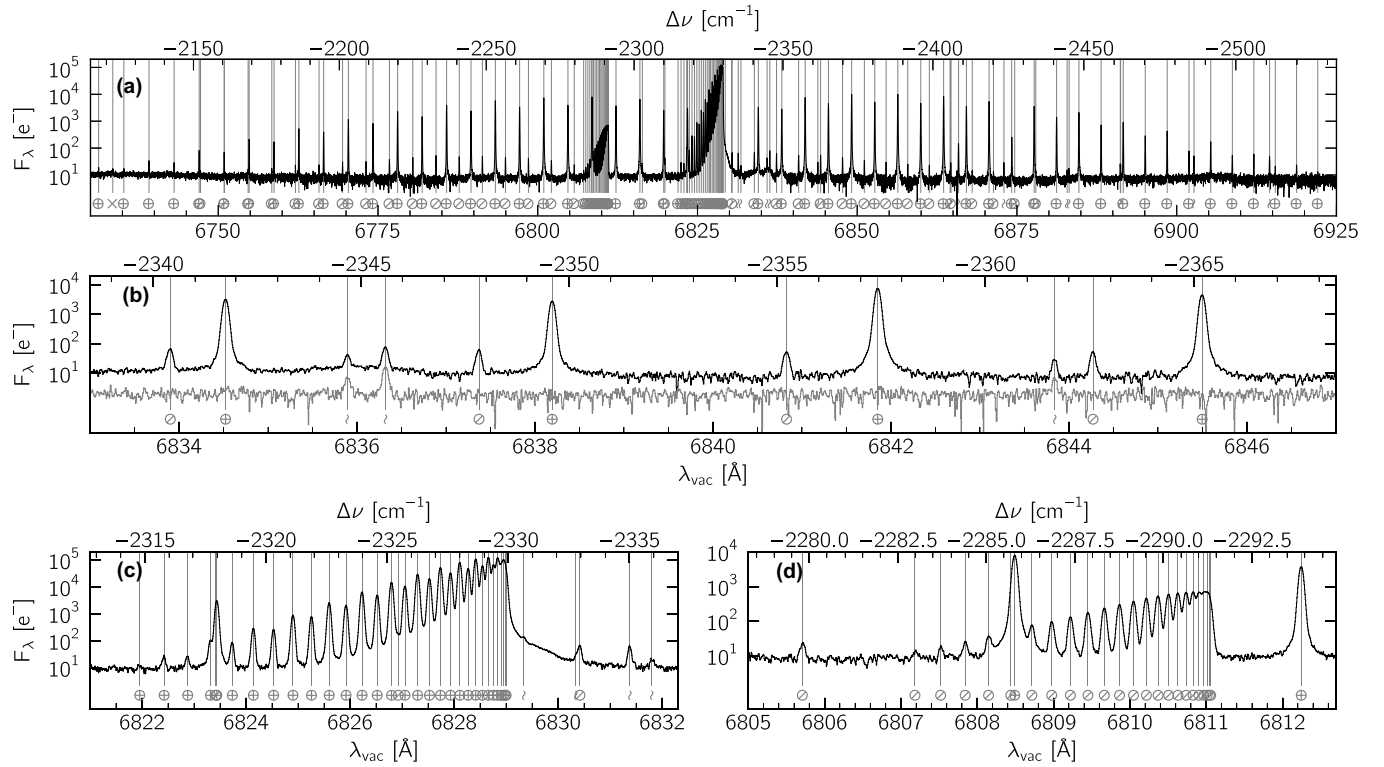


FIG. 8. (a) $\nu_{1 \leftarrow 0}$ vibrational-rotational forest for the $^{14}\text{N}^{14}\text{N}$ and $^{14}\text{N}^{15}\text{N}$ molecules. (b) Detailed view of a subset of Raman and sky lines. Sky lines can be unambiguously identified via their presence in the reference sky spectrum (shown in grey, scaled and shifted for visualization purposes). (c) Detailed view of the Q-branch of the $^{14}\text{N}^{14}\text{N}$ molecule. (d) Detailed view of the Q-branch of the $^{14}\text{N}^{15}\text{N}$ molecule. In every panel, the theoretical position of individual Raman lines, sky lines, and artefacts are marked using vertical grey lines. Each is tagged using the symbols introduced in Fig. 6.

TABLE III. Same as Table II, but for the rotational-vibrational line sets of $^{16}\text{O}^{16}\text{O}$ and its isotopes.

Molecule	Vibrational level	$\Delta N \Delta J$	(J, N)	max(N)
$^{16}\text{O}^{16}\text{O}$	$1 \leftarrow 0$	oQ	(N, N)	33
$^{16}\text{O}^{16}\text{O}$	$1 \leftarrow 0$	oP	(N, N)	16
$^{16}\text{O}^{16}\text{O}$	$1 \leftarrow 0$	oP	$(N+1, N)$	16
$^{16}\text{O}^{16}\text{O}$	$1 \leftarrow 0$	oR	(N, N)	16
$^{16}\text{O}^{16}\text{O}$	$1 \leftarrow 0$	oR	$(N-1, N)$	16
$^{16}\text{O}^{16}\text{O}$	$1 \leftarrow 0$	oS	$(N-1, N)$	3
$^{16}\text{O}^{16}\text{O}$	$1 \leftarrow 0$	oO	$(N+1, N)$	3
$^{16}\text{O}^{16}\text{O}$	$1 \leftarrow 0$	sS	$(N, N-1)$	1
$^{16}\text{O}^{16}\text{O}$	$1 \leftarrow 0$	sS	(N, N)	29
$^{16}\text{O}^{16}\text{O}$	$1 \leftarrow 0$	sR	(N, N)	15
$^{16}\text{O}^{16}\text{O}$	$1 \leftarrow 0$	sR	$(N+1, N)$	15
$^{16}\text{O}^{16}\text{O}$	$1 \leftarrow 0$	oO	$(N, N-1)$	3
$^{16}\text{O}^{16}\text{O}$	$1 \leftarrow 0$	oO	(N, N)	29
$^{16}\text{O}^{16}\text{O}$	$1 \leftarrow 0$	oP	(N, N)	17
$^{16}\text{O}^{16}\text{O}$	$1 \leftarrow 0$	oP	$(N-1, N)$	17
$^{16}\text{O}^{16}\text{O}$	$2 \leftarrow 0$	oQ	(N, N)	19
$^{16}\text{O}^{17}\text{O}$	$1 \leftarrow 0$	oQ	(N, N)	19
$^{16}\text{O}^{17}\text{O}$	$1 \leftarrow 0$	sS	(N, N)	5
$^{16}\text{O}^{17}\text{O}$	$1 \leftarrow 0$	oO	(N, N)	6
$^{16}\text{O}^{18}\text{O}$	$1 \leftarrow 0$	oQ	(N, N)	23
$^{16}\text{O}^{18}\text{O}$	$1 \leftarrow 0$	sS	(N, N)	19
$^{16}\text{O}^{18}\text{O}$	$1 \leftarrow 0$	oO	(N, N)	17

frequency ν' to air molecules moving with a velocity w_{LoS} along the line-of-sight, where

$$\nu' = \nu_* \left(1 - \frac{w_{\text{LoS}}}{c} \right) \quad (6)$$

with $c = 299792458 \text{ m s}^{-1}$ the speed of light, and w_{LoS} taken to be positive for molecules moving away from UT4. The frequency of this photon after being Raman-scattered is

$$\nu'' = \nu' + \Delta\nu = \nu_* \left(1 - \frac{w_{\text{LoS}}}{c} \right) + \Delta\nu \quad (7)$$

with $\Delta\nu$ the Raman shift associated to the specific molecular transition (de-)excited through the inelastic scattering process. With the exception of the pure-rotational anti-Stokes lines, all the Raman lines observed in the ESPRESSO spectrum have $\Delta\nu < 0 \text{ cm}^{-1}$. The Raman-scattered photon will then itself appear Doppler-shifted to a frequency ν_{obs} in the UT4 rest frame, where

$$\nu_{\text{obs}} = \nu'' \frac{c}{c + w_{\text{LoS}}} = \nu_* \frac{c - w_{\text{LoS}}}{c + w_{\text{LoS}}} + \Delta\nu \frac{c}{c + w_{\text{LoS}}}. \quad (8)$$

We are here assuming that the laser photons are emitted along the optical axis of the UT4 telescope: A reasonable assumption given that the inclination of the laser beams for our observations is $\alpha \approx 89.985^\circ$ (see Sec. II C).

When measuring the position of the Raman lines in the ESPRESSO spectrum, this Doppler shift will result in a pseudoredshift zc of the lines compared to their expected frequency $\nu_{\text{ref}} = \nu_* + \Delta\nu$, where

$$\begin{aligned} zc &= \frac{\lambda_{\text{obs}} - \lambda_{\text{ref}}}{\lambda_{\text{ref}}} = \frac{\nu_{\text{ref}} - \nu_{\text{obs}}}{\nu_{\text{obs}}} \\ &= w_{\text{LoS}} \frac{2\nu_* + \Delta\nu}{\nu_* (1 - \frac{w_{\text{LoS}}}{c}) + \Delta\nu} \\ &\approx w_{\text{LoS}} \left(2 - \frac{\Delta\nu}{\nu_* + \Delta\nu} \right). \end{aligned} \quad (9)$$

The largest Raman shifts observed in the ESPRESSO spectra are associated to the $\nu_{2 \leftarrow 0}$ rotational-vibrational band of $^{16}\text{O}^{16}\text{O}$ (see Sec. III A), which corresponds to $\Delta\nu \approx -3000 \text{ cm}^{-1}$. On the blueshifted side, pure-rotational Raman lines of the anti-Stokes branch can be identified only up to $\Delta\nu \approx +250 \text{ cm}^{-1}$. The *Raman component* of zc is thus small for all the lines in the ESPRESSO data, with

$$-0.02 \lesssim \frac{-\Delta\nu}{\nu_* + \Delta\nu} \lesssim 0.2. \quad (10)$$

The intensity and direction of the wind along the line-of-sight w_{LoS} can be estimated from the projection of the horizontal wind vector (derived from the ERA5 reanalysis dataset, see Sec. II A) at the altitude H_{obs} onto the UT4 pointing direction

$$w_{\text{LoS}} = \vec{w}_{H_{\text{obs}}} \cdot \vec{\zeta}, \quad (11)$$

where

$$\vec{w}_{H_{\text{obs}}} = \begin{pmatrix} w_u \\ w_v \\ 0 \end{pmatrix}, \quad \vec{\zeta} = \begin{pmatrix} \cos \psi \cos \phi \\ \cos \psi \sin \phi \\ \sin \psi \end{pmatrix}, \quad (12)$$

with ϕ the UT4 azimuth measured counterclockwise from the East, $\psi \in [0^\circ, 90^\circ]$ the UT4 pointing altitude, and w_u (w_v) the ERA5 reanalysis eastward (northward) component of the wind at a geometric altitude H_{obs} . $w_u > 0$ ($w_v > 0$) indicates wind moving towards the East (North). With these conventions, the link between ϕ and the telescope azimuth provided in ESO FITS files is

$$\phi = -(90 + \text{HIERARCH ESO TEL4 AZ}). \quad (13)$$

The value of w_{LoS} for every ESPRESSO exposure acquired during our observing run is presented in Fig. 9. With a vertical resolution of 2–3 km at the altitudes of interest and a temporal resolution of 1 hr, the ERA5 reanalysis dataset cannot be used to perform a detailed modeling of the wind shifts present in every ESPRESSO exposures, let alone correct them with a level of accuracy of $< 10 \text{ m s}^{-1}$. It does nonetheless provide a reasonable estimate of the direction and order of magnitude of the redshifts zc to be expected. This analysis indicates that the altitudes observed with ESPRESSO are located systematically above the jet stream layer, where horizontal wind speeds always remained below $\sim 15 \text{ m s}^{-1}$ during our observing run. Accounting for the projection onto the telescope line-of-sight, the majority of our observations are thus unlikely to have been subjected to on-axis wind speeds larger than 5 m s^{-1} . For the set 1 exposures specifically, 77 ($\equiv 84\%$) exposures have

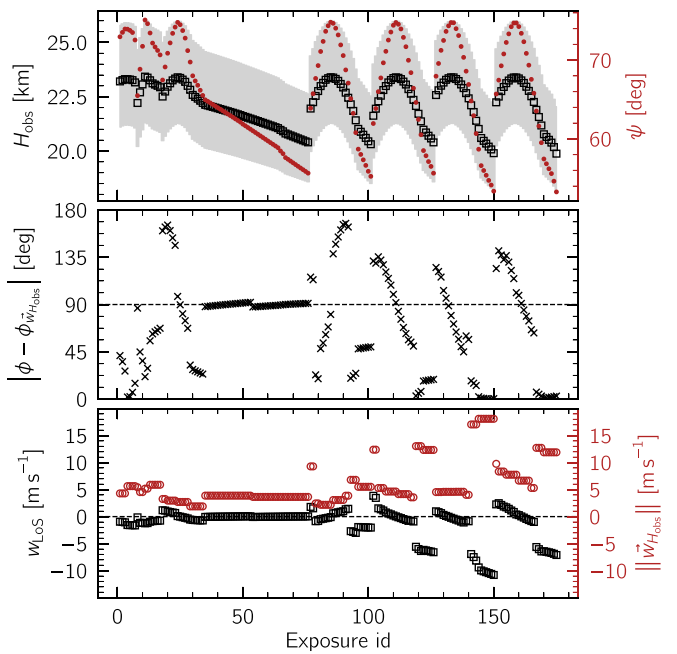


FIG. 9. Top: Geometric altitude H_{obs} associated to a line-of-sight focus distance $D = 21.5 \text{ km}$ for all the 175 ESPRESSO exposures acquired during the observing run. The shaded area shows the projected interval $[D - \Delta_D^-; D + \Delta_D^+]$. The telescope altitude ψ is shown in red. Middle: angular offset between the UT4 pointing direction ϕ and the horizontal wind direction $\phi_{\vec{w}_{H_{\text{obs}}}}$ at the altitude H_{obs} , derived from the ERA5 re-analysis dataset. Bottom: Wind speed along the UT4 line-of-sight w_{LoS} (black) associated to the total horizontal wind speed $\|\vec{w}_{H_{\text{obs}}}\|$ at the geometric altitude H_{obs} .

$|w_{\text{LoS}}| < 2.5 \text{ m s}^{-1}$, 82 ($\equiv 89\%$) exposures have $|w_{\text{LoS}}| < 5 \text{ m s}^{-1}$, and 92 ($\equiv 100\%$) exposures have $|w_{\text{LoS}}| < 10 \text{ m s}^{-1}$.

To measure the actual redshift zc of Raman lines in the ESPRESSO spectra, we adopt a line model composed of three Gaussian components, where the outer two are located exactly 1.713 GHz on either side of the central one, and have their peak intensity set to 1/9 of the central component. In other words, we assume the 4LGSF repumping sidelines are perfectly tied to the central line, both spectrally and in intensity. For each set 1 and set 3 individual exposure, we perform a Markov-Chain Monte-Carlo sampling of the individual posterior distribution of the parameters associated to a given line, using a least-square likelihood and flat priors with a lower bound of 0 for the line intensities and dispersion. For consistency with [26], we adopt $\lambda_* = 5891.59120 \text{ \AA}$ for the central lasing wavelength of all LGSUs. The results for the pure-rotational line associated to the $^{16}\text{O}^{16}\text{O}^{\text{S}}(19, 19)$ transition (with a Raman shift of $\Delta\nu = -117.555334 \text{ cm}^{-1}$) are presented in Fig. 10. For each exposure, a violin symbol is used to trace the full extent of our posterior distribution sampling of the line apparent velocity shift, together with the velocity shift expected from the wind alone [following Eq. (9)].

The slopes of the set 1 zc measurements appear broadly consistent with the gradient expected from UT4 slowly turning towards the West (into the wind) as it tracks the target field across meridian. There is, however, a clear blueshift of

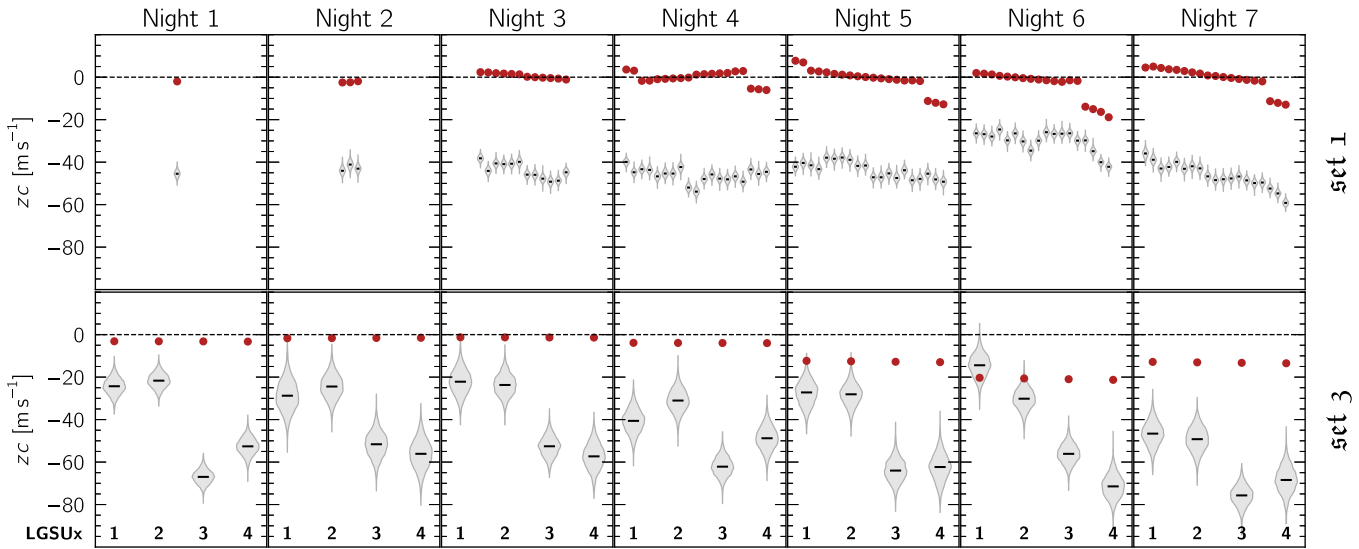


FIG. 10. Measured redshift z_c of the pure-rotational Raman line associated to the $^{16}\text{O}^{16}\text{O}^{\circ}\text{S}(19, 19)$ transition, for every **set 1** and **set 3** exposure, split by observing night. The grey violin symbols trace our full sampling of the posterior distribution of z_c for this line in every exposure, with the median value marked using a black bar. Each measurement can be compared to the redshift that can be expected from the wind speed at the time and location of the observations following Eq. (9), which is shown using red dots. For each **set 3** exposure, the LGSU that was propagating (and thus observed) is indicated.

$-40 \pm 5 \text{ m s}^{-1}$ in the line position, which is unexplained by the wind. This offset is constant for every observing night, albeit somewhat less strong for night 6. Most plausibly, this difference is a consequence of the reboot of the 4LGSF system (and lack of subsequent wavelength meter calibration) on the first half of that specific night.

Light from all four LGSUs is present in **set 1** exposures, albeit in varying mixing ratios depending on the exposure (see Sec. II B). The **set 3** exposures, on the other hand, target a single LGSU each. They reveal that the blueshift z_c observed in **set 1** exposures results in fact from the combination of different offsets for the different LGSUs: $-25 \pm 5 \text{ m s}^{-1}$ for LGSU1/2, and $-55 \pm 5 \text{ m s}^{-1}$ for LGSU3/4. In other words, the different LGSUs of the 4LGSF do not all lase at the same wavelength, and none of them lase at the nominal wavelength of $\lambda_* = 5891.59120 \text{ \AA}$.

This explains the LGSU-dependant Raman line blueshifts detected consistently over seven distinct nights. Alternative causes (meteorological/instrumental/technical/software) can all be ruled out given:

- (1) the extreme spectral stability of ESPRESSO (by design),
- (2) the time difference of no more than 3–4 minutes between consecutive **set 3** exposures in a given quadruplet, with no difference in the instrumental/telescope setup other than a switch of the propagating LGSUs,
- (3) the use of LFC calibration frames acquired within less than 2.5 hr for all exposures on-sky, and
- (4) the very stable atmospheric conditions over the entire duration of the observing run.

We thus introduce ϵ_x the difference between the LGSUs' true lasing frequency $v_{\text{LGSU}x}^T$ and $v_* = c\lambda_*^{-1}$,

$$\epsilon_x = v_{\text{LGSU}x}^T - v_*. \quad (14)$$

Similarly to the wind in Eq. (9), ϵ_x can be linked to the observed line redshift z_c via

$$\begin{aligned} z_c &= \frac{v_* - v_{\text{LGSU}x}^T}{v_{\text{LGSU}x}^T} \\ &= \frac{-\epsilon_x c}{v_* + \epsilon_x + \Delta v}, \end{aligned} \quad (15)$$

such that

$$\begin{aligned} \epsilon_x &= -\frac{v_* + \Delta v}{1 + \frac{c}{z_c}} \\ &\approx -(v_* + \Delta v) \frac{z_c}{c}. \end{aligned} \quad (16)$$

From our observations, we find that

- (i) $\epsilon_1 \approx \epsilon_2 \approx +43 \pm 10 \text{ MHz} \cong -50 \mp 10 \text{ fm}$, and
- (ii) $\epsilon_3 \approx \epsilon_4 \approx +94 \pm 10 \text{ MHz} \cong -109 \mp 10 \text{ fm}$.

The offset of $\sim 50 \text{ MHz}$ between LGSU1/2 and LGSU3/4 appears consistent with dedicated measurements acquired during the commissioning of the 4LGSF [59]. The values of these spectral shifts are several times larger than the observed (relative) spectral stability of the LGUs (better than $\pm 3 \text{ MHz}$ at the $1-\sigma$ level over hours, see [60]). The formal ESO requirements for the LGU's peak-to-peak laser emission wavelength variation over 14 h is 80 MHz (see [61]). The values of ϵ_1 , ϵ_2 , ϵ_3 , and ϵ_4 also remain significantly smaller than the thermal broadening (of the order of 1 GHz) [47,62] of the atomic transitions of sodium atoms to be excited at an altitude of $\sim 90 \text{ km}$ to create laser guide-stars. They are thus of no consequences for adaptive optics purposes. They do, however, prevent any formal assessment of the spectral accuracy of ESPRESSO at the required level of 10 m s^{-1} .

IV. CONCLUSIONS

We have used the high-resolution optical échelle spectrograph ESPRESSO to acquire, from the astronomical observatory of Cerro Paranal, a 15.3-hr-deep spectrum of the four 4LGSF 589 nm sodium laser beams with a resolution of $\lambda/\Delta\lambda \approx 140000 \approx 0.04 \text{ \AA} \approx 0.12 \text{ cm}^{-1}$. This spectrum reveals the pure-rotational and rotational-vibrational Raman signature of the atmosphere at an altitude of 23 km above sea level. It extends from 3775 Å to 7895 Å, equivalent to a Raman shift range of +9517 cm⁻¹ to -4307 cm⁻¹. It contains pure-rotational and rotational-vibrational Raman lines from the most abundant molecules in the atmosphere at this altitude, including their isotopes: ¹⁴N ¹⁴N, ¹⁴N ¹⁵N, ¹⁶O ¹⁶O, ¹⁶O ¹⁷O, ¹⁶O ¹⁸O, and ¹²C ¹⁶O ¹⁶O.

The depth (i.e., the signal-to-noise) and spectral accuracy of these observations is such that professional observatories can treat the catalog of identified Raman lines as exhaustive (over the specific Raman shift range, for the observed molecules) for the purpose of correcting Raman contamination of astronomical data. It must be noted than in addition to the 865 Raman transitions identified in the spectrum, a handful of emission line-like features (including 22 lines within $\pm 56 \text{ \AA} \approx \mp 160 \text{ cm}^{-1}$ of the main laser line) remain unidentified at this stage. Some of them at least exhibit a *Raman-like* distribution. However, the complex nature of the artefacts resulting from the strong saturation of the main laser line prevents us from ruling out an artificial origin without the formal identification of the molecular transitions. All these unidentified lines are at least 4.5 orders of magnitude fainter than the main laser lines, and should thus be of no concern to all but the most demanding astronomical observations.

The detection of spectral shifts between the different LGSUs of the 4LGSF prevent us from formally assessing the spectral accuracy of ESPRESSO as proposed by [26]. The main limitation lies in the unconstrained mix of light from the different LGSUs in the set 1 exposures, that cannot be disentangled prior to their combination. For the purpose of measuring the radial velocity accuracy of ultrahigh resolution spectrographs like ESPRESSO at a level of 10 m s⁻¹, independent knowledge of the lasing frequency with an accuracy <10 MHz ≈ 10 fm is paramount. The assessment of the accuracy of ESPRESSO by means of the Raman lines will thus remain out of reach until the lasing frequency of the different LGSUs can be measured down to that level. Our data indicate that the main lasing frequency of LGSU1/2 (LGSU3/4) is blueshifted by $+43 \pm 10 \text{ MHz} \cong -50 \mp 10 \text{ fm}$ ($+94 \pm 10 \text{ MHz} \cong -109 \mp 10 \text{ fm}$) from $\lambda_* = 5891.59120 \text{ \AA}$.

The fact that our observations reveal the presence of spectral shifts in the 4LGSF lasing frequencies at the level of a few tens of MHz nonetheless demonstrates how Raman lines can be exploited by professional observatories as wavelength references. Their observations is not straightforward. Short of the insertion of a notch filter in the optical path, the important contrast between the main laser line and the Raman lines will inevitably lead to the strong saturation of the former, for optical astronomical instruments with a broad spectral coverage. The resulting artefacts (see Sec. II E) can pose real challenges for the subsequent analysis of the data. To reach the highest level of accuracy, the influence of the wind must also be taken

carefully into account in the design of the observations. By observing at high elevations, outside from any jet stream, and at azimuths perpendicular to the dominant atmospheric currents, the spectral redshifts caused by wind can be kept within $\pm 5 \text{ m s}^{-1}$ (see Sec. III B).

Provided that their lasing wavelength can be characterized with sufficient accuracy, the ever-increasing presence of laser guide-star systems at professional astronomical observatories worldwide could also prove interesting for atmospheric research. A high-resolution spectrograph like ESPRESSO can for example lead to a factor ~ 10 improvement in the measured Raman transitions of ¹⁴N ¹⁴N and ¹⁴N ¹⁵N (see Appendix C). The large collecting areas of ground-based astronomical telescopes could also enable the study and monitoring of very faint Raman signals, for example that of oxygen isotopes up to the highest layers of the atmosphere [63].

ACKNOWLEDGMENTS

We are very grateful to A. Cabral and J. P. Coelho for simulating the observational setup described in Sec. II using their *Zemax* model of UT4, its Coudé train, and the ESPRESSO instrument. We thank Telescope & Instrument Operator Extraordinaire Diego Parraguez, Night Astronomer Anita Zanella, and Instrument Gurus José-Luis Álvares, Juan Beltran Peña, and Álvaro Díaz for their infallible support during the observing run. We also acknowledge the courtesy of the MUSE Consortium (with visitor time awarded immediately prior to our observations) for turning the telescope over to us on-time every night. We thank R. Matthey de l'Endroit for enlightening discussions and valuable suggestions regarding this article, as well as the anonymous reviewer for constructive feedback. This research has made use of the following Python packages: *aplpy* (an open-source plotting package for Python) [64], *astroplan* [65], *astropy* (a community-developed core PYTHON package for Astronomy) [66,67], *astroquery* (a package hosted online [68], which provides a set of tools for querying astronomical web forms and databases; [69,70]), *dfitspy* [71], *emcee* [72], *fcmaker* (a PYTHON module to create ESO-compliant finding charts for OBs on *p2*; [73,74]), *matplotlib* [75], *numpy* [76], *pandas* [77,78], *scipy* [79], *spectres* [80], and *specutils* [81]. This research has also made use of the *Aladin* interactive sky atlas [82], of *SAOImage ds9* [developed by Smithsonian Astrophysical Observatory [83]], and of NASA's Astrophysics Data System. A portion of this work has been carried out within the framework of the National Centre of Competence in Research PlanetS supported by the Swiss National Science Foundation. PFi acknowledges the financial support of the SNSF. Other portions of this article present research carried out at the Jet Propulsion Laboratory, California Institute of Technology, under contract with the National Aeronautics and Space Administration. Government sponsorship is acknowledged by S.Y. The article contains modified Copernicus Climate Change Service information 2022. Neither the European Commission nor ECMWF is responsible for any use that may be made of the Copernicus information or data it contains. Based on observations made with ESO Telescopes at the La Silla Paranal Observatory under Program Id. 4104.L-0074(A). All the observations described in this article are

freely available online from the ESO Science Archive Facility. No detector was harmed during the astronomical observations presented in this article.

APPENDIX A: IMPORTANT ACQUISITION STEPS FOR Program Id. 4104.L-0074

The ESPRESSO observations of the 4LGSF up-link laser beams presented in this article were highly nonstandard. For reproducibility purposes, we list here important steps in the acquisition and observing sequence.

Calibrations:

(1) Perform manual wavemeter calibrations for all LGSUs every day of the run, in the afternoon.

(2) Execute a complete set of LFC and ThAr wavelength calibrations as close as possible before (after) the start (the end) of the observations. We systematically executed a set of FP_FP, THAR_FP, FP_THAR, THAR_THAR, LFC_FP, and FP_LFC calibrations.

Acquisition steps:

(1) Start the telescope and ESPRESSO preset normally. Proceed until ESPRESSO asks to select the target.

(2) Use the LPC to manually place all the lasers in the wide-field mode asterism, and apply the computed corrections. Then, move the lasers to the narrow-field mode asterism.

(3) The laser guide-stars (at ~ 90 km of altitude) are now visible out-of-focus as four donuts of ~ 10 arcsec in diameter in the ESPRESSO TCCD. Change the TCCD density filter to the minimum value.

(4) Stop the telescope Active Optics cycle after a few corrections have been applied.

(5) Offset the focus of the telescope by moving the secondary mirror by a few mm to bring the up-link beams in focus. The focus nominal value was -20 mm: we used an offset of $+10$ mm to reach a final focus position of -10 mm. The telescope guide-star gets lost in the process, and telescope guiding stops.

(6) Send absolute Alt-Az presets to the 4LGSF to move the laser beams into position. Monitor the changes using the ESPRESSO TCCD. For reference, here is a reasonable guess for the offsets required to cross the beams over the ESPRESSO fiber A:

- (i) LGSU1: Alt: $+35$ arcsec; Az: -13 arcsec
- (ii) LGSU2: Alt: -40 arcsec; Az: -13 arcsec
- (iii) LGSU3: Alt: -40 arcsec; Az: $+02$ arcsec
- (iv) LGSU4: Alt: $+33$ arcsec; Az: $+05$ arcsec

Loosing the beams while moving them is extremely likely, when applying large positional shifts or focus changes. Applying a series of small successive focus changes and positional offsets is thus preferable, at least for the first acquisition.

(7) With the four up-link laser beams crossed over the ESPRESSO fiber, continue with the ESPRESSO acquisition. Disable the field stabilization when asked.

(8) Execute the laser observations. Monitor the motions of the laser beams with respect to the fiber using the ESPRESSO TCCD. Use the ESPRESSO exposure meter to monitor the flux received in the fiber A.

(9) Pause the observing every 20 minutes. Sequentially toggle the propagation of individual laser guide-stars on/off.

For each, adjust the pointing as necessary by sending manual offsets to the LGSU.

(10) Every hour, pause the observing, revert the telescope focus to the sky (\equiv infinity), and apply a few cycles of active optics corrections. This helps account for the gravity vector changing over time for the telescope.

APPENDIX B: OBSERVING LOG

We list in Table IV the complete list of raw ESPRESSO exposures acquired under Program Id. 4104.L-0074. All these files are freely accessible from the ESO Science Archive Facility. The status of the different LGSUs (either propagating, or not) is specified explicitly for each exposure. This table is accessible electronically as a VizieR [51] catalogue [52] at the Centre de Données astronomiques de Strasbourg (CDS) via anonymous ftp [84] or over https [85].

APPENDIX C: RAMAN LINES IDENTIFIED IN THE 15.3-HR-DEEP ESPRESSO SPECTRUM OF THE 4LGSF LASER BEAMS

Table V provides an exhaustive list of all the pure-rotational and rotational-vibrational Raman lines that could be identified in the ESPRESSO spectrum described in Sec. IIIA. This table is accessible electronically as a VizieR [51] catalogue [52] at the Centre de Données astronomiques de Strasbourg (CDS) via anonymous ftp [84] or over https [85]. The lines were not identified individually, but rather by sets (see Tables II and III for the sets of O₂). We limited the lines included in a given set to quantum numbers for which the line has a signal-to-noise greater than 1. The only exceptions are the ¹⁶O ¹⁶O rotational-vibrational lines in the sets ⁵S ($N, N - 1$) and ³O ($N, N - 1$). They cannot be identified beyond $N = 1$ and $N = 3$ (respectively) because of their blending with lines in the sets ⁵S (N, N) and ³O (N, N).

Strictly speaking, not every line listed in Table V is *visible* in the ESPRESSO spectrum presented in Fig. 5. Some lines are blended with stronger ones. Others are affected by saturation-induced artefacts. Several are also located in the immediate vicinity of the main laser line at $\Delta\nu = 0$: a spectral region (reconstructed from the set 4 exposures) that has a smaller signal-to-noise. These lines are included in Table V nonetheless, on the basis that (1) they belong to clearly identified theoretical sets found to match the data without evident deviation, and (2) they are surrounded by other lines in the same set that are visible in the spectrum.

The lines are listed in descending order of their Raman shift $\Delta\nu$, with the convention that $\Delta\nu = \nu_{\text{obs}} - \nu_*$ with ν_{obs} and ν_* the Raman-scattered and original laser photon frequencies. The corresponding vacuum wavelengths λ_{vac} are computed with respect to $\lambda_* = 5891.59120$ Å via

$$\lambda_{\text{vac}} = c \left(\frac{c}{\lambda_*} - \Delta\nu_{\text{Hz}} \right)^{-1}, \quad (\text{C1})$$

with $\Delta\nu_{\text{Hz}}$ the Raman shift $\Delta\nu$ expressed in Hz. These wavelengths are quoted to 3 decimals only, in view of the uncertainty regarding the exact lasing frequencies of the 4LGSF LGUs (see Sec. IIIB). Readers requiring accuracy down to the fm level are urged to re-compute the values of λ_{vac} via

TABLE IV. Observing log for ESO Program Id. 4104.L-0074. For each exposure, the status of each LGSU is specified explicitly: either *propagating* (●), or *not propagating* (○). The *set* value identifies different groups of exposures discussed in the article.

#	ESO archive filename	UT4 altitude [°]	Focus [mm]	Exp. time [s]	LGSUx status				<i>set</i>	Comments
					1	2	3	4		
Night 1										
1	ESPRe.2019-10-22T05:02:07.619.fits	72.966	-10.0	300.0	●	○	●	●		
2	ESPRe.2019-10-22T05:11:23.619.fits	73.528	-10.0	600.0	●	○	●	●	1	
3	ESPRe.2019-10-22T05:24:43.346.fits	73.955	-10.0	600.0	○	○	○	○		
4	ESPRe.2019-10-22T05:36:16.411.fits	73.937	-10.0	300.0	●	○	○	○	3	
5	ESPRe.2019-10-22T05:42:36.409.fits	73.774	-10.0	300.0	○	●	○	○	3	
6	ESPRe.2019-10-22T05:48:51.138.fits	73.508	-10.0	300.0	○	○	●	○	3	Moonrise: 5:57 UT
7	ESPRe.2019-10-22T06:02:57.681.fits	72.560	-10.0	300.0	○	○	○	●	3	
Night 2										
8	ESPRe.2019-10-23T04:24:28.591.fits	65.494	-10.0	1200.0	○	○	○	○	2	
9	ESPRe.2019-10-23T04:45:30.716.fits	68.850	-10.0	1200.0	○	○	○	○	2	
10	ESPRe.2019-10-23T05:06:32.885.fits	71.757	-10.0	1200.0	○	○	○	○	2	
11	ESPRe.2019-10-23T06:06:16.015.fits	75.101	-10.0	600.0	●	○	●	●	1	
12	ESPRe.2019-10-23T06:17:18.138.fits	74.630	-10.0	600.0	●	○	●	●	1	
13	ESPRe.2019-10-23T06:32:33.139.fits	73.449	-10.0	600.0	●	○	●	●	1	
14	ESPRe.2019-10-23T06:44:32.041.fits	72.167	-10.0	120.0	●	○	○	○	3	Moonrise: 6:47 UT
15	ESPRe.2019-10-23T06:48:37.309.fits	71.671	-10.0	120.0	○	●	○	○	3	
16	ESPRe.2019-10-23T06:52:04.012.fits	71.231	-10.0	120.0	○	○	●	○	3	
17	ESPRe.2019-10-23T06:56:18.295.fits	70.668	-10.0	120.0	○	○	○	●	3	
Night 3										
18	ESPRe.2019-10-24T05:14:31.743.fits	67.476	-10.0	600.0	●	○	●	●	1	
19	ESPRe.2019-10-24T05:25:33.887.fits	69.133	-10.0	600.0	●	○	●	●	1	
20	ESPRe.2019-10-24T05:38:20.655.fits	70.878	-10.0	600.0	●	○	●	●	1	
21	ESPRe.2019-10-24T05:49:22.802.fits	72.191	-10.0	600.0	●	○	●	●	1	
22	ESPRe.2019-10-24T06:01:48.714.fits	73.403	-10.0	600.0	●	○	●	●	1	
23	ESPRe.2019-10-24T06:12:50.864.fits	74.195	-10.0	600.0	●	○	●	●	1	
24	ESPRe.2019-10-24T06:37:02.440.fits	74.795	-10.0	600.0	●	○	●	●	1	
25	ESPRe.2019-10-24T06:48:04.537.fits	74.506	-10.0	600.0	●	○	●	●	1	
26	ESPRe.2019-10-24T07:00:50.823.fits	73.757	-10.0	600.0	●	○	●	●	1	
27	ESPRe.2019-10-24T07:11:52.961.fits	72.798	-10.0	600.0	●	○	●	●	1	
28	ESPRe.2019-10-24T07:26:03.851.fits	71.209	-10.0	600.0	●	○	●	●	1	Moonrise: 7:33 UT
29	ESPRe.2019-10-24T07:37:05.983.fits	69.759	-10.0	600.0	●	○	●	●	1	
30	ESPRe.2019-10-24T07:49:07.930.fits	68.010	-10.0	120.0	●	○	○	○	3	
31	ESPRe.2019-10-24T07:53:19.033.fits	67.362	-10.0	120.0	○	●	○	○	3	
32	ESPRe.2019-10-24T07:56:51.052.fits	66.807	-10.0	120.0	○	○	●	○	3	
33	ESPRe.2019-10-24T08:00:48.507.fits	66.173	-10.0	120.0	○	○	○	●	3	
34	ESPRe.2019-10-24T08:04:51.102.fits	65.516	-10.0	1.0	○	○	●	○		
35	ESPRe.2019-10-24T08:08:12.461.fits	64.962	-10.0	1.0	○	○	●	○		
36	ESPRe.2019-10-24T08:09:24.455.fits	64.765	-10.0	1.0	○	○	●	○		
37	ESPRe.2019-10-24T08:10:33.994.fits	64.567	-10.0	1.0	○	○	●	○		
38	ESPRe.2019-10-24T08:11:46.084.fits	64.368	-10.0	1.0	○	○	●	○		
39	ESPRe.2019-10-24T08:12:55.865.fits	64.168	-10.0	1.0	○	○	●	○		
40	ESPRe.2019-10-24T08:14:07.954.fits	63.968	-10.0	1.0	○	○	●	○		
41	ESPRe.2019-10-24T08:15:20.023.fits	63.763	-10.0	1.0	○	○	●	○		
42	ESPRe.2019-10-24T08:16:32.121.fits	63.558	-10.0	1.0	○	○	●	○		
43	ESPRe.2019-10-24T08:17:41.709.fits	63.356	-10.0	1.0	○	○	●	○		
44	ESPRe.2019-10-24T08:18:51.411.fits	63.158	-10.0	1.0	○	○	●	○		
45	ESPRe.2019-10-24T08:20:01.107.fits	62.957	-10.0	1.0	○	○	●	○		
46	ESPRe.2019-10-24T08:21:13.137.fits	62.752	-10.0	1.0	○	○	●	○		
47	ESPRe.2019-10-24T08:22:25.139.fits	62.540	-10.0	1.0	○	○	●	○		
48	ESPRe.2019-10-24T08:23:37.139.fits	62.337	-10.0	1.0	○	○	●	○		
49	ESPRe.2019-10-24T08:24:46.714.fits	62.127	-10.0	1.0	○	○	●	○		
50	ESPRe.2019-10-24T08:26:16.712.fits	61.864	-10.0	10.0	○	○	●	○		
51	ESPRe.2019-10-24T08:27:28.857.fits	61.659	-10.0	10.0	○	○	●	○		
52	ESPRe.2019-10-24T08:28:40.964.fits	61.444	-10.0	10.0	○	○	●	○		
53	ESPRe.2019-10-24T08:29:53.056.fits	61.232	-10.0	10.0	○	○	●	○		

TABLE IV. (*Continued.*)

#	ESO archive filename	UT4 altitude [°]	Focus [mm]	Exp. time [s]	LGSUx status				set	Comments
					1	2	3	4		
54	ESPRE.2019-10-24T08:31:05.138.fits	61.019	-10.0	10.0	○	○	●	○		
55	ESPRE.2019-10-24T08:32:17.139.fits	60.806	-10.0	10.0	○	○	●	○		
56	ESPRE.2019-10-24T08:33:29.282.fits	60.592	-10.0	10.0	○	○	●	○		
57	ESPRE.2019-10-24T08:34:41.365.fits	60.377	-10.0	10.0	○	○	●	○		
58	ESPRE.2019-10-24T08:35:53.503.fits	60.163	-10.0	10.0	○	○	●	○		
59	ESPRE.2019-10-24T08:37:05.512.fits	59.947	-10.0	10.0	○	○	●	○		
60	ESPRE.2019-10-24T08:38:15.130.fits	59.734	-10.0	10.0	○	○	●	○		
61	ESPRE.2019-10-24T08:39:27.139.fits	59.521	-10.0	10.0	○	○	●	○		
62	ESPRE.2019-10-24T08:40:37.009.fits	59.307	-10.0	10.0	○	○	●	○		
63	ESPRE.2019-10-24T08:41:49.118.fits	59.093	-10.0	10.0	○	○	●	○		
64	ESPRE.2019-10-24T08:43:01.139.fits	58.875	-10.0	10.0	○	○	●	○		
65	ESPRE.2019-10-24T08:45:15.692.fits	58.462	-10.5	1.0	○	○	●	○		
66	ESPRE.2019-10-24T08:47:09.604.fits	58.119	-11.0	1.0	○	○	●	○		
67	ESPRE.2019-10-24T08:49:52.846.fits	57.618	-11.0	1.0	○	○	●	○	4	
68	ESPRE.2019-10-24T08:51:04.896.fits	57.404	-11.0	1.0	○	○	●	○	4	
69	ESPRE.2019-10-24T08:52:16.966.fits	57.180	-11.0	1.0	○	○	●	○	4	
70	ESPRE.2019-10-24T08:53:29.082.fits	56.959	-11.0	1.0	○	○	●	○	4	
71	ESPRE.2019-10-24T08:54:41.137.fits	56.737	-11.0	1.0	○	○	●	○	4	
72	ESPRE.2019-10-24T08:55:53.139.fits	56.516	-11.0	1.0	○	○	●	○	4	
73	ESPRE.2019-10-24T08:57:02.822.fits	56.297	-11.0	1.0	○	○	●	○	4	
74	ESPRE.2019-10-24T08:58:12.303.fits	56.084	-11.0	1.0	○	○	●	○	4	
75	ESPRE.2019-10-24T08:59:24.399.fits	55.864	-11.0	1.0	○	○	●	○	4	
76	ESPRE.2019-10-24T09:00:34.138.fits	55.644	-11.0	1.0	○	○	●	○	4	
Night 4										
77	ESPRE.2019-10-25T04:48:32.384.fits	63.893	-10.0	600.0	●	○	●	●	1	
78	ESPRE.2019-10-25T04:59:34.525.fits	65.732	-10.0	600.0	●	○	●	●	1	
79	ESPRE.2019-10-25T05:11:49.138.fits	67.677	-10.0	600.0	●	○	●	●	1	
80	ESPRE.2019-10-25T05:22:48.137.fits	69.308	-10.0	600.0	●	○	●	●	1	
81	ESPRE.2019-10-25T05:36:07.848.fits	71.100	-10.0	600.0	●	○	●	●	1	
82	ESPRE.2019-10-25T05:47:09.992.fits	72.381	-10.0	600.0	●	○	●	●	1	
83	ESPRE.2019-10-25T06:00:54.137.fits	73.659	-10.0	600.0	●	○	●	●	1	
84	ESPRE.2019-10-25T06:11:56.328.fits	74.369	-10.0	600.0	●	○	●	●	1	
85	ESPRE.2019-10-25T06:28:33.344.fits	74.817	-10.0	600.0	●	○	●	●	1	
86	ESPRE.2019-10-25T06:39:32.640.fits	74.675	-10.0	600.0	●	○	●	●	1	
87	ESPRE.2019-10-25T06:52:46.985.fits	74.054	-10.0	600.0	●	○	●	●	1	
88	ESPRE.2019-10-25T07:03:45.985.fits	73.202	-10.0	600.0	●	○	●	●	1	
89	ESPRE.2019-10-25T07:16:07.335.fits	71.935	-10.0	600.0	●	○	●	●	1	
90	ESPRE.2019-10-25T07:27:09.471.fits	70.581	-10.0	600.0	●	○	●	●	1	
91	ESPRE.2019-10-25T07:40:13.396.fits	68.759	-10.0	600.0	●	○	●	●	1	
92	ESPRE.2019-10-25T07:51:12.858.fits	67.088	-10.0	600.0	●	○	●	●	1	
93	ESPRE.2019-10-25T08:03:29.443.fits	65.102	-10.0	600.0	●	○	●	●	1	
94	ESPRE.2019-10-25T08:14:31.493.fits	63.242	-10.0	600.0	●	○	●	●	1	Moonrise: 8:16 UT
95	ESPRE.2019-10-25T08:28:28.866.fits	60.791	-10.0	600.0	●	○	●	●	1	
96	ESPRE.2019-10-25T08:40:06.915.fits	58.695	-10.0	120.0	●	○	○	○	3	
97	ESPRE.2019-10-25T08:43:47.655.fits	58.023	-10.0	120.0	○	●	○	○	3	
98	ESPRE.2019-10-25T08:47:32.139.fits	57.338	-10.0	120.0	○	○	●	○	3	
99	ESPRE.2019-10-25T08:51:22.067.fits	56.631	-10.0	120.0	○	○	○	●	3	
100	ESPRE.2019-10-25T08:55:26.030.fits	55.877	-10.0	120.0	○	○	●	○	3	LGSU3 detuned
101	ESPRE.2019-10-25T08:58:52.034.fits	55.241	-10.0	600.0	○	○	●	○	3	LGSU3 detuned
Night 5										
102	ESPRE.2019-10-26T04:33:22.954.fits	61.951	-10.0	600.0	●	○	●	●	1	
103	ESPRE.2019-10-26T04:44:25.138.fits	63.858	-10.0	600.0	●	○	●	●	1	
104	ESPRE.2019-10-26T04:57:16.668.fits	65.998	-10.0	600.0	●	○	●	●	1	
105	ESPRE.2019-10-26T05:08:18.811.fits	67.741	-10.0	600.0	●	○	●	●	1	
106	ESPRE.2019-10-26T05:21:22.139.fits	69.660	-10.0	600.0	●	○	●	●	1	
107	ESPRE.2019-10-26T05:32:24.139.fits	71.119	-10.0	600.0	●	○	●	●	1	
108	ESPRE.2019-10-26T05:44:50.070.fits	72.549	-10.0	600.0	●	○	●	●	1	

TABLE IV. (*Continued.*)

#	ESO archive filename	UT4 altitude [°]	Focus [mm]	Exp. time [s]	LGSUx status				set	Comments
					1	2	3	4		
109	ESPРЕ.2019-10-26T05:55:52.138.fits	73.569	-10.0	600.0	●	●	●	●	1	
110	ESPРЕ.2019-10-26T06:09:09.138.fits	74.428	-10.0	600.0	●	●	●	●	1	
111	ESPРЕ.2019-10-26T06:20:11.139.fits	74.781	-10.0	600.0	●	●	●	●	1	
112	ESPРЕ.2019-10-26T06:39:27.139.fits	74.556	-10.0	600.0	●	●	●	●	1	
113	ESPРЕ.2019-10-26T06:50:27.138.fits	73.963	-10.0	600.0	●	●	●	●	1	
114	ESPРЕ.2019-10-26T07:03:22.913.fits	72.893	-10.0	600.0	●	●	●	●	1	
115	ESPРЕ.2019-10-26T07:14:25.049.fits	71.705	-10.0	600.0	●	●	●	●	1	
116	ESPРЕ.2019-10-26T07:27:52.493.fits	69.984	-10.0	600.0	●	●	●	●	1	
117	ESPРЕ.2019-10-26T07:38:52.355.fits	68.409	-10.0	600.0	●	●	●	●	1	
118	ESPРЕ.2019-10-26T07:51:37.755.fits	66.433	-10.0	600.0	●	●	●	●	1	
119	ESPРЕ.2019-10-26T08:02:39.949.fits	64.624	-10.0	600.0	●	●	●	●	1	
120	ESPРЕ.2019-10-26T08:15:17.751.fits	62.467	-10.0	600.0	●	●	●	●	1	
121	ESPРЕ.2019-10-26T08:26:17.452.fits	60.524	-10.0	600.0	●	●	●	●	1	
122	ESPРЕ.2019-10-26T08:37:26.974.fits	58.513	-10.0	120.0	○	○	○	○	3	
123	ESPРЕ.2019-10-26T08:41:01.279.fits	57.858	-10.0	120.0	○	●	○	○	3	
124	ESPРЕ.2019-10-26T08:45:05.039.fits	57.114	-10.0	120.0	○	○	●	○	3	
125	ESPРЕ.2019-10-26T08:48:25.073.fits	56.501	-10.0	120.0	○	○	○	●	3	
126	ESPРЕ.2019-10-26T08:53:02.901.fits	55.639	-10.0	120.0	●	●	●	●		All LGSUs detuned
			Night 6							
127	ESPРЕ.2019-10-27T05:05:49.138.fits	67.961	-10.0	600.0	●	●	●	●	1	4LGSF rebooted in H1
128	ESPРЕ.2019-10-27T05:16:51.355.fits	69.576	-10.0	600.0	●	●	●	●	1	
129	ESPРЕ.2019-10-27T05:29:29.138.fits	71.246	-10.0	600.0	●	●	●	●	1	
130	ESPРЕ.2019-10-27T05:40:31.325.fits	72.503	-10.0	600.0	●	●	●	●	1	
131	ESPРЕ.2019-10-27T05:52:59.972.fits	73.649	-10.0	600.0	●	●	●	●	1	
132	ESPРЕ.2019-10-27T06:04:02.131.fits	74.357	-10.0	600.0	●	●	●	●	1	
133	ESPРЕ.2019-10-27T06:16:55.535.fits	74.773	-10.0	600.0	●	●	●	●	1	
134	ESPРЕ.2019-10-27T06:27:57.644.fits	74.749	-10.0	600.0	●	●	●	●	1	
135	ESPРЕ.2019-10-27T06:45:34.489.fits	73.998	-10.0	600.0	●	●	●	●	1	
136	ESPРЕ.2019-10-27T06:56:36.591.fits	73.124	-10.0	600.0	●	●	●	●	1	
137	ESPРЕ.2019-10-27T07:09:51.374.fits	71.735	-10.0	600.0	●	●	●	●	1	
138	ESPРЕ.2019-10-27T07:20:53.496.fits	70.354	-10.0	600.0	●	●	●	●	1	
139	ESPРЕ.2019-10-27T07:33:21.905.fits	68.596	-10.0	600.0	●	●	●	●	1	
140	ESPРЕ.2019-10-27T07:44:24.087.fits	66.910	-10.0	600.0	●	●	●	●	1	
141	ESPРЕ.2019-10-27T07:57:14.055.fits	64.818	-10.0	600.0	●	●	●	●	1	
142	ESPРЕ.2019-10-27T08:08:16.139.fits	62.945	-10.0	600.0	●	●	●	●	1	
143	ESPРЕ.2019-10-27T08:21:12.985.fits	60.667	-10.0	600.0	●	●	●	●	1	
144	ESPРЕ.2019-10-27T08:32:15.132.fits	58.684	-10.0	600.0	●	●	●	●	1	
145	ESPРЕ.2019-10-27T08:43:35.858.fits	56.599	-10.0	120.0	●	●	●	●		
146	ESPРЕ.2019-10-27T08:46:55.913.fits	55.982	-10.0	120.0	○	○	○	○	3	
147	ESPРЕ.2019-10-27T08:50:10.984.fits	55.375	-10.0	120.0	○	●	○	○	3	
148	ESPРЕ.2019-10-27T08:53:39.892.fits	54.725	-10.0	120.0	○	○	●	○	3	
149	ESPРЕ.2019-10-27T08:56:49.920.fits	54.133	-10.0	120.0	○	○	○	●	3	
150	ESPРЕ.2019-10-27T09:00:59.138.fits	53.354	-10.0	600.0	●	●	●	●		LGSU2,4 detuned
			Night 7							
151	ESPРЕ.2019-10-28T04:47:33.849.fits	65.698	-10.0	600.0	●	●	●	●	1	
152	ESPРЕ.2019-10-28T04:58:35.980.fits	67.460	-10.0	600.0	●	●	●	●	1	
153	ESPРЕ.2019-10-28T05:10:46.522.fits	69.281	-10.0	600.0	●	●	●	●	1	
154	ESPРЕ.2019-10-28T05:21:48.555.fits	70.787	-10.0	600.0	●	●	●	●	1	
155	ESPРЕ.2019-10-28T05:34:02.434.fits	72.248	-10.0	600.0	●	●	●	●	1	
156	ESPРЕ.2019-10-28T05:45:04.569.fits	73.338	-10.0	600.0	●	●	●	●	1	
157	ESPРЕ.2019-10-28T05:57:31.116.fits	74.246	-10.0	600.0	●	●	●	●	1	
158	ESPРЕ.2019-10-28T06:08:33.140.fits	74.714	-10.0	600.0	●	●	●	●	1	
159	ESPРЕ.2019-10-28T06:26:51.884.fits	74.722	-10.0	600.0	●	●	●	●	1	
160	ESPРЕ.2019-10-28T06:37:54.077.fits	74.264	-10.0	600.0	●	●	●	●	1	
161	ESPРЕ.2019-10-28T06:49:52.499.fits	73.407	-10.0	600.0	●	●	●	●	1	
162	ESPРЕ.2019-10-28T07:00:54.574.fits	72.338	-10.0	600.0	●	●	●	●	1	
163	ESPРЕ.2019-10-28T07:13:21.105.fits	70.859	-10.0	600.0	●	●	●	●	1	

TABLE IV. (*Continued.*)

#	ESO archive filename	UT4 altitude [°]	Focus [mm]	Exp. time [s]	LGSUx status				set	Comments
					1	2	3	4		
164	ESPRESSO.2019-10-28T07:24:23.291.fits	69.361	-10.0	600.0	●	○	○	○	1	
165	ESPRESSO.2019-10-28T07:36:31.285.fits	67.560	-10.0	600.0	●	○	○	○	1	
166	ESPRESSO.2019-10-28T07:47:33.420.fits	65.801	-10.0	600.0	●	○	○	○	1	
167	ESPRESSO.2019-10-28T08:01:02.635.fits	63.538	-10.0	600.0	●	○	○	○	1	
168	ESPRESSO.2019-10-28T08:12:02.071.fits	61.623	-10.0	600.0	●	○	○	○	1	
169	ESPRESSO.2019-10-28T08:23:52.059.fits	59.511	-10.0	600.0	●	○	○	○	1	
170	ESPRESSO.2019-10-28T08:35:12.138.fits	57.446	-10.0	120.0	●	○	○	○	3	
171	ESPRESSO.2019-10-28T08:38:28.038.fits	56.837	-10.0	120.0	○	●	○	○	3	
172	ESPRESSO.2019-10-28T08:41:54.748.fits	56.202	-10.0	120.0	○	○	●	○	3	
173	ESPRESSO.2019-10-28T08:45:12.406.fits	55.588	-10.0	120.0	○	○	○	●	3	
174	ESPRESSO.2019-10-28T08:50:21.586.fits	54.626	-10.0	300.0	●	○	○	○		LGSU1,2,4 detuned
175	ESPRESSO.2019-10-28T08:57:37.422.fits	53.261	-10.0	300.0	●	○	○	○		All LGSUs detuned

Eq. (C1) using the best possible estimate of λ_* available to them at the time.

It must be stressed that the list of Raman shifts provided in Table V is not the result of a fitting procedure using the ESPRESSO data described in this article. These are all obtained from the literature, and merely compared against the ESPRESSO spectrum to identify the different emission lines in it. The shifts therefore have varying degrees of accuracy, with those associated to the O₂ molecule being the most accurate (and thus the most suitable for acting as wavelength references). The readers are referred to the original sources for specific details:

(1) ¹⁶O ¹⁶O, ¹⁶O ¹⁷O, ¹⁶O ¹⁸O

The Raman shifts for these molecules were obtained from a complex Hamiltonian model [53–56] that was used to simultaneously fit the microwave, THz, infrared, visible and ultraviolet transitions of all six oxygen isotopologues. The model accounts for the ³S electronic ground state of these molecules, which leads to a fine-structure splitting of the lines. The specific fine-structure level of each O₂ line in Table V is specified as ${}^{\Delta N} \Delta J$ ($J_{\text{lower}}, N_{\text{lower}}$) alongside the vibrational levels. With an accuracy $<0.0001 \text{ cm}^{-1}$, these Raman shifts are the most accurate in Table V.

(ii) ¹⁴N ¹⁴N, ¹⁴N ¹⁵N

We treat these molecules as diatomic nonrigid rotators, and account for the vibrational stretching of the molecular bond driven by rotation to derive the Raman shifts for the different branches and values of the rotational quantum number $J = N$. The corresponding equations are laid out in details in the Appendix of [26], to which we refer the reader for further details. Unlike [26], however, we rely here on the molecular parameters from [86]. The specific transition of each N₂ line in Table V is identified in the form ΔJ (J_{lower}). Their accuracy

is $\sim 0.001 \text{ cm}^{-1}$. One should note that in the case of anti-Stokes lines, $J_{\text{lower}} \neq J_{\text{final}}$, since the laser photons gain energy from excited molecules in those transitions. With our adopted notation, the first Stokes and anti-Stokes lines of a given molecule are thus both labeled as S(0) (for more details, see Sec. 8.2 in [87]).

(iii) ¹²C ¹⁶O ¹⁶O:

For the pure-rotational lines, we treat these molecules using the same approach as N₂, with the molecular constants from [88]. The rotational-vibrational shifts, on the other hand, are taken from [50]. With an accuracy $\sim 0.1 \text{ cm}^{-1}$, these Raman shifts are the least accurate in Table V.

The intensity of the Raman lines in a dedicated/contaminated observation acquired using an astronomical spectrograph will be highly dependent on

- (1) the technical specifications of the instrument, telescope, and laser system,
- (2) the parameters of the laser *collision*, and (to a much lesser extent), and
- (3) the meteorological conditions.

In Table V, we thus provide a measure of the order of magnitude difference between the intensity of the main laser line I_* (visible through Rayleigh and Mie scattering at $\Delta v = 0$) and the intensity of each Raman line I , in lieu of direct fluxes. This measure, computed as $\log(I_*/I)$, is directly estimated from the ESPRESSO spectrum presented in Fig. 5. It indicates, in relative terms, which Raman lines are the strongest, and thus most easily detectable. It must be stressed that this measure is indicative only, in that it does not rely on any complex line fitting scheme. No special treatment is applied to blended lines, the relative intensity of which will be overestimated. Overall, we identify Raman lines with intensities spanning 5 orders of magnitude.

TABLE V. Exhaustive list of all the Raman lines identified in the 15.3-hr-deep ESPRESSO spectrum of the 4LGSF laser beams. The line wavelengths are quoted in vacuum. They are computed with respect to $\lambda_* = 5891.59120 \text{ \AA}$. The value $\log(I_*/I)$ provides a crude measure of the order of magnitude difference between a given line and the main laser line visible through Rayleigh and Mie scattering at $\Delta\nu = 0$. The larger this value, the fainter the Raman line.

$\Delta\nu (\text{cm}^{-1})$	$\lambda_{\text{vac}} (\text{\AA})$	$\log(\frac{I_*}{I})$	Molecule	Transition
+249.248396	5806.327	6.4	$^{14}\text{N}^{14}\text{N}$	$v_{0\leftarrow 0}$
+241.431361	5808.964	6.4	$^{16}\text{O}^{16}\text{O}$	$v_{0\leftarrow 0}$
+241.422811	5808.967	6.4	$^{14}\text{N}^{14}\text{N}$	$v_{0\leftarrow 0}$
+233.588798	5811.611	6.2	$^{14}\text{N}^{14}\text{N}$	$v_{0\leftarrow 0}$
+230.330204	5812.712	6.5	$^{16}\text{O}^{16}\text{O}$	$v_{0\leftarrow 0}$
+225.746637	5814.261	6.2	$^{14}\text{N}^{14}\text{N}$	$v_{0\leftarrow 0}$
+219.191412	5816.478	6.4	$^{16}\text{O}^{16}\text{O}$	$v_{0\leftarrow 0}$
+217.896601	5816.916	5.9	$^{14}\text{N}^{14}\text{N}$	$v_{0\leftarrow 0}$
+210.038970	5819.576	5.8	$^{14}\text{N}^{14}\text{N}$	$v_{0\leftarrow 0}$
+208.016844	5820.261	6.3	$^{16}\text{O}^{16}\text{O}$	$v_{0\leftarrow 0}$
+202.174020	5822.241	5.4	$^{14}\text{N}^{14}\text{N}$	$v_{0\leftarrow 0}$
+196.808357	5824.060	6.1	$^{16}\text{O}^{16}\text{O}$	$v_{0\leftarrow 0}$
+195.493814	5824.506	6.2	$^{14}\text{N}^{15}\text{N}$	$v_{0\leftarrow 0}$
+194.302025	5824.911	5.4	$^{14}\text{N}^{14}\text{N}$	$v_{0\leftarrow 0}$
+187.880102	5827.090	6.0	$^{14}\text{N}^{15}\text{N}$	$v_{0\leftarrow 0}$
+186.423262	5827.585	4.8	$^{14}\text{N}^{14}\text{N}$	$v_{0\leftarrow 0}$
+185.567812	5827.876	5.7	$^{16}\text{O}^{16}\text{O}$	$v_{0\leftarrow 0}$
+180.260064	5829.679	5.8	$^{14}\text{N}^{15}\text{N}$	$v_{0\leftarrow 0}$
+178.538009	5830.264	4.8	$^{14}\text{N}^{14}\text{N}$	$v_{0\leftarrow 0}$
+174.297064	5831.706	5.3	$^{16}\text{O}^{16}\text{O}$	$v_{0\leftarrow 0}$
+172.633958	5832.272	5.5	$^{14}\text{N}^{15}\text{N}$	$v_{0\leftarrow 0}$
+170.646538	5832.948	4.3	$^{14}\text{N}^{14}\text{N}$	$v_{0\leftarrow 0}$
+165.002043	5834.869	5.2	$^{14}\text{N}^{15}\text{N}$	$v_{0\leftarrow 0}$
+162.997971	5835.551	4.8	$^{16}\text{O}^{16}\text{O}$	$v_{0\leftarrow 0}$
+162.749129	5835.636	4.3	$^{14}\text{N}^{14}\text{N}$	$v_{0\leftarrow 0}$
+157.364579	5837.470	5.4	$^{14}\text{N}^{15}\text{N}$	$v_{0\leftarrow 0}$
+154.846058	5838.329	3.9	$^{14}\text{N}^{14}\text{N}$	$v_{0\leftarrow 0}$
+153.995182	5838.619	5.6	$^{16}\text{O}^{18}\text{O}$	$v_{0\leftarrow 0}$
+152.727264	5839.051	5.6	$^{16}\text{O}^{17}\text{O}$	$v_{0\leftarrow 0}$
+151.672395	5839.411	4.6	$^{16}\text{O}^{16}\text{O}$	$v_{0\leftarrow 0}$
+149.721822	5840.076	5.6	$^{14}\text{N}^{15}\text{N}$	$v_{0\leftarrow 0}$
+148.645020	5840.443	5.8	$^{16}\text{O}^{18}\text{O}$	$v_{0\leftarrow 0}$
+147.225734	5840.927	5.7	$^{16}\text{O}^{17}\text{O}$	$v_{0\leftarrow 0}$
+146.937599	5841.026	4.0	$^{14}\text{N}^{14}\text{N}$	$v_{0\leftarrow 0}$
+143.289160	5842.271	5.9	$^{16}\text{O}^{18}\text{O}$	$v_{0\leftarrow 0}$
+142.497831	5842.541	6.0	$^{16}\text{O}^{16}\text{O}$	$v_{0\leftarrow 0}$
+142.074029	5842.685	5.6	$^{14}\text{N}^{15}\text{N}$	$v_{0\leftarrow 0}$
+141.718404	5842.807	6.0	$^{16}\text{O}^{17}\text{O}$	$v_{0\leftarrow 0}$
+140.322190	5843.284	4.2	$^{16}\text{O}^{16}\text{O}$	$v_{0\leftarrow 0}$
+139.024033	5843.727	3.5	$^{14}\text{N}^{14}\text{N}$	$v_{0\leftarrow 0}$
+137.927811	5844.101	6.0	$^{16}\text{O}^{18}\text{O}$	$v_{0\leftarrow 0}$
+136.205493	5844.689	6.1	$^{16}\text{O}^{17}\text{O}$	$v_{0\leftarrow 0}$
+134.421460	5845.299	5.6	$^{14}\text{N}^{15}\text{N}$	$v_{0\leftarrow 0}$
+132.561178	5845.935	6.0	$^{16}\text{O}^{18}\text{O}$	$v_{0\leftarrow 0}$
+131.106673	5846.432	3.6	$^{16}\text{O}^{16}\text{O}$	$v_{0\leftarrow 0}$
+131.105628	5846.432	3.6	$^{14}\text{N}^{14}\text{N}$	$v_{0\leftarrow 0}$
+130.687223	5846.575	5.9	$^{16}\text{O}^{17}\text{O}$	$v_{0\leftarrow 0}$
+128.949217	5847.169	3.9	$^{16}\text{O}^{16}\text{O}$	$v_{0\leftarrow 0}$
+127.189468	5847.771	6.0	$^{16}\text{O}^{18}\text{O}$	$v_{0\leftarrow 0}$
+126.764374	5847.916	5.4	$^{14}\text{N}^{15}\text{N}$	$v_{0\leftarrow 0}$
+125.163811	5848.464	6.1	$^{16}\text{O}^{17}\text{O}$	$v_{0\leftarrow 0}$
+123.182670	5849.142	3.2	$^{14}\text{N}^{14}\text{N}$	$v_{0\leftarrow 0}$
+121.812890	5849.610	6.0	$^{16}\text{O}^{18}\text{O}$	$v_{0\leftarrow 0}$
+119.694406	5850.335	5.9	$^{16}\text{O}^{16}\text{O}$	$v_{0\leftarrow 0}$
+119.635475	5850.355	6.0	$^{16}\text{O}^{17}\text{O}$	$v_{0\leftarrow 0}$

TABLE V. (*Continued.*)

$\Delta\nu$ (cm ⁻¹)	λ_{vac} (Å)	$\log(\frac{I_*}{I})$	Molecule	Transition
+119.103028	5850.538	5.3	¹⁴ N ¹⁵ N	$v_{0 \leftarrow 0}$ S (14)
+118.571823	5850.719	6.2	¹⁶ O ¹⁸ O	$v_{0 \leftarrow 0}$ sR (21, 20)
+117.555334	5851.067	3.5	¹⁶ O ¹⁶ O	$v_{0 \leftarrow 0}$ sS (19, 19)
+116.431651	5851.452	5.9	¹⁶ O ¹⁸ O	$v_{0 \leftarrow 0}$ sS (20, 20)
+115.731700	5851.692	5.8	¹⁶ O ¹⁶ O	$v_{0 \leftarrow 0}$ sR (19, 19)
+115.255426	5851.855	3.3	¹⁴ N ¹⁴ N	$v_{0 \leftarrow 0}$ S (13)
+114.102435	5852.250	6.1	¹⁶ O ¹⁷ O	$v_{0 \leftarrow 0}$ sS (19, 19)
+113.177475	5852.567	6.2	¹⁶ O ¹⁸ O	$v_{0 \leftarrow 0}$ sR (20, 19)
+111.437677	5853.163	5.2	¹⁴ N ¹⁵ N	$v_{0 \leftarrow 0}$ S (13)
+111.045957	5853.297	5.9	¹⁶ O ¹⁸ O	$v_{0 \leftarrow 0}$ sS (19, 19)
+108.564908	5854.147	6.0	¹⁶ O ¹⁷ O	$v_{0 \leftarrow 0}$ sS (18, 18)
+108.262817	5854.250	5.7	¹⁶ O ¹⁶ O	$v_{0 \leftarrow 0}$ sR (18, 17)
+107.778821	5854.416	5.6	¹⁶ O ¹⁸ O	$v_{0 \leftarrow 0}$ sR (19, 18)
+107.324181	5854.572	2.9	¹⁴ N ¹⁴ N	$v_{0 \leftarrow 0}$ S (12)
+106.142399	5854.977	3.2	¹⁶ O ¹⁶ O	$v_{0 \leftarrow 0}$ sS (17, 17)
+105.656016	5855.144	5.6	¹⁶ O ¹⁸ O	$v_{0 \leftarrow 0}$ sS (18, 18)
+104.300412	5855.609	5.7	¹⁶ O ¹⁶ O	$v_{0 \leftarrow 0}$ sR (17, 17)
+103.768587	5855.791	5.1	¹⁴ N ¹⁵ N	$v_{0 \leftarrow 0}$ S (12)
+103.023115	5856.047	6.1	¹⁶ O ¹⁷ O	$v_{0 \leftarrow 0}$ sS (17, 17)
+102.376058	5856.269	6.2	¹⁶ O ¹⁸ O	$v_{0 \leftarrow 0}$ sR (18, 17)
+100.262034	5856.994	5.6	¹⁶ O ¹⁸ O	$v_{0 \leftarrow 0}$ sS (17, 17)
+99.389204	5857.293	3.0	¹⁴ N ¹⁴ N	$v_{0 \leftarrow 0}$ S (11)
+97.477275	5857.949	6.0	¹⁶ O ¹⁷ O	$v_{0 \leftarrow 0}$ sS (16, 16)
+96.969381	5858.124	6.1	¹⁶ O ¹⁸ O	$v_{0 \leftarrow 0}$ sR (17, 16)
+96.813658	5858.177	5.5	¹⁶ O ¹⁶ O	$v_{0 \leftarrow 0}$ sR (16, 15)
+96.096008	5858.423	5.0	¹⁴ N ¹⁵ N	$v_{0 \leftarrow 0}$ S (11)
+94.864219	5858.846	4.2	¹⁶ O ¹⁸ O	$v_{0 \leftarrow 0}$ sS (16, 16)
+94.712272	5858.898	3.0	¹⁶ O ¹⁶ O	$v_{0 \leftarrow 0}$ sS (15, 15)
+92.851524	5859.537	5.4	¹⁶ O ¹⁶ O	$v_{0 \leftarrow 0}$ sR (15, 15)
+91.927605	5859.854	5.4	¹⁶ O ¹⁷ O	$v_{0 \leftarrow 0}$ sS (15, 15)
+91.558983	5859.981	3.3	¹⁶ O ¹⁸ O	$v_{0 \leftarrow 0}$ sR (16, 15)
+91.450775	5860.018	2.6	¹⁴ N ¹⁴ N	$v_{0 \leftarrow 0}$ S (10)
+89.462780	5860.701	5.5	¹⁶ O ¹⁸ O	$v_{0 \leftarrow 0}$ sS (15, 15)
+88.420205	5861.059	4.8	¹⁴ N ¹⁵ N	$v_{0 \leftarrow 0}$ S (10)
+86.374323	5861.762	5.9	¹⁶ O ¹⁷ O	$v_{0 \leftarrow 0}$ sS (14, 14)
+86.145050	5861.841	6.1	¹⁶ O ¹⁸ O	$v_{0 \leftarrow 0}$ sR (15, 14)
+85.348623	5862.114	5.2	¹⁶ O ¹⁶ O	$v_{0 \leftarrow 0}$ sR (14, 13)
+84.057921	5862.558	5.2	¹⁶ O ¹⁸ O	$v_{0 \leftarrow 0}$ sS (14, 14)
+83.509167	5862.746	2.8	¹⁴ N ¹⁴ N	$v_{0 \leftarrow 0}$ S (9)
+83.266808	5862.830	2.8	¹⁶ O ¹⁶ O	$v_{0 \leftarrow 0}$ sS (13, 13)
+81.386728	5863.476	5.1	¹⁶ O ¹⁶ O	$v_{0 \leftarrow 0}$ sR (13, 13)
+80.817651	5863.672	5.0	¹⁶ O ¹⁷ O	$v_{0 \leftarrow 0}$ sS (13, 13)
+80.741431	5863.698	4.7	¹⁴ N ¹⁵ N	$v_{0 \leftarrow 0}$ S (9)
+80.727763	5863.703	4.8	¹⁶ O ¹⁸ O	$v_{0 \leftarrow 0}$ sR (14, 13)
+78.649850	5864.417	5.3	¹⁶ O ¹⁸ O	$v_{0 \leftarrow 0}$ sS (13, 13)
+77.327801	5864.872	6.0	¹⁶ O ¹⁷ O	$v_{0 \leftarrow 0}$ sR (13, 12)
+77.148253	5864.934	5.9	¹² C ¹⁶ O ¹⁶ O	$v_{0 \leftarrow 0}$ S (48)
+75.564660	5865.478	2.4	¹⁴ N ¹⁴ N	$v_{0 \leftarrow 0}$ S (8)
+75.307300	5865.567	4.5	¹⁶ O ¹⁸ O	$v_{0 \leftarrow 0}$ sR (13, 12)
+75.257806	5865.584	4.8	¹⁶ O ¹⁷ O	$v_{0 \leftarrow 0}$ sS (12, 12)
+74.040661	5866.003	5.7	¹² C ¹⁶ O ¹⁶ O	$v_{0 \leftarrow 0}$ S (46)
+73.869302	5866.062	4.9	¹⁶ O ¹⁶ O	$v_{0 \leftarrow 0}$ sR (12, 11)
+73.238776	5866.279	5.2	¹⁶ O ¹⁸ O	$v_{0 \leftarrow 0}$ sS (12, 12)
+73.059947	5866.340	4.7	¹⁴ N ¹⁵ N	$v_{0 \leftarrow 0}$ S (8)
+71.807871	5866.771	2.6	¹⁶ O ¹⁶ O	$v_{0 \leftarrow 0}$ sS (11, 11)
+71.755059	5866.789	2.8	¹⁶ O ¹⁷ O	$v_{0 \leftarrow 0}$ sR (12, 11)
+70.931896	5867.073	5.6	¹² C ¹⁶ O ¹⁶ O	$v_{0 \leftarrow 0}$ S (44)
+69.907616	5867.425	4.9	¹⁶ O ¹⁶ O	$v_{0 \leftarrow 0}$ sR (11, 11)

TABLE V. (*Continued.*)

$\Delta\nu$ (cm ⁻¹)	λ_{vac} (Å)	$\log(\frac{I_*}{I})$	Molecule	Transition
+69.883823	5867.433	4.9	¹⁶ O ¹⁸ O	$v_{0\leftarrow 0}$ <i>sR</i> (12, 11)
+69.695006	5867.498	5.6	¹⁶ O ¹⁷ O	$v_{0\leftarrow 0}$ <i>sS</i> (11, 11)
+67.824904	5868.142	4.5	¹⁶ O ¹⁸ O	$v_{0\leftarrow 0}$ <i>sS</i> (11, 11)
+67.821998	5868.143	4.4	¹² C ¹⁶ O ¹⁶ O	$v_{0\leftarrow 0}$ <i>S</i> (42)
+67.617529	5868.214	2.7	¹⁴ N ¹⁴ N	$v_{0\leftarrow 0}$ <i>S</i> (7)
+66.179288	5868.709	5.8	¹⁶ O ¹⁷ O	$v_{0\leftarrow 0}$ <i>sR</i> (11, 10)
+65.921856	5868.798	5.9	¹⁶ O ¹⁸ O	$v_{0\leftarrow 0}$ <i>sR</i> (11, 11)
+65.376009	5868.986	4.6	¹⁴ N ¹⁵ N	$v_{0\leftarrow 0}$ <i>S</i> (7)
+64.711027	5869.215	5.7	¹² C ¹⁶ O ¹⁶ O	$v_{0\leftarrow 0}$ <i>S</i> (40)
+64.457482	5869.302	5.9	¹⁶ O ¹⁸ O	$v_{0\leftarrow 0}$ <i>sR</i> (11, 10)
+64.129472	5869.415	5.6	¹⁶ O ¹⁷ O	$v_{0\leftarrow 0}$ <i>sS</i> (10, 10)
+62.408442	5870.008	4.6	¹⁶ O ¹⁸ O	$v_{0\leftarrow 0}$ <i>sS</i> (10, 10)
+62.377078	5870.019	4.6	¹⁶ O ¹⁶ O	$v_{0\leftarrow 0}$ <i>sR</i> (10, 9)
+61.599029	5870.287	5.5	¹² C ¹⁶ O ¹⁶ O	$v_{0\leftarrow 0}$ <i>S</i> (38)
+60.600622	5870.631	4.7	¹⁶ O ¹⁷ O	$v_{0\leftarrow 0}$ <i>sR</i> (10, 9)
+60.495603	5870.667	3.8	¹⁶ O ¹⁸ O	$v_{0\leftarrow 0}$ <i>sR</i> (10, 10)
+60.337315	5870.722	2.5	¹⁶ O ¹⁶ O	$v_{0\leftarrow 0}$ <i>sS</i> (9, 9)
+59.668053	5870.952	2.3	¹⁴ N ¹⁴ N	$v_{0\leftarrow 0}$ <i>S</i> (6)
+59.028406	5871.173	5.2	¹⁶ O ¹⁸ O	$v_{0\leftarrow 0}$ <i>sR</i> (10, 9)
+58.561420	5871.334	5.1	¹⁶ O ¹⁷ O	$v_{0\leftarrow 0}$ <i>sS</i> (9, 9)
+58.486050	5871.360	4.7	¹² C ¹⁶ O ¹⁶ O	$v_{0\leftarrow 0}$ <i>S</i> (36)
+58.415569	5871.384	4.6	¹⁶ O ¹⁶ O	$v_{0\leftarrow 0}$ <i>sR</i> (9, 9)
+57.689878	5871.634	4.6	¹⁴ N ¹⁵ N	$v_{0\leftarrow 0}$ <i>S</i> (6)
+56.989599	5871.876	5.0	¹⁶ O ¹⁸ O	$v_{0\leftarrow 0}$ <i>sS</i> (9, 9)
+56.638959	5871.997	5.8	¹⁶ O ¹⁷ O	$v_{0\leftarrow 0}$ <i>sR</i> (9, 9)
+55.372141	5872.434	5.4	¹² C ¹⁶ O ¹⁶ O	$v_{0\leftarrow 0}$ <i>S</i> (34)
+55.066607	5872.539	5.8	¹⁶ O ¹⁸ O	$v_{0\leftarrow 0}$ <i>sR</i> (9, 9)
+55.019157	5872.555	5.8	¹⁶ O ¹⁷ O	$v_{0\leftarrow 0}$ <i>sR</i> (9, 8)
+53.596688	5873.046	5.7	¹⁶ O ¹⁸ O	$v_{0\leftarrow 0}$ <i>sR</i> (9, 8)
+52.991071	5873.255	5.5	¹⁶ O ¹⁷ O	$v_{0\leftarrow 0}$ <i>sS</i> (8, 8)
+52.257356	5873.508	5.1	¹² C ¹⁶ O ¹⁶ O	$v_{0\leftarrow 0}$ <i>S</i> (32)
+51.716502	5873.694	2.6	¹⁴ N ¹⁴ N	$v_{0\leftarrow 0}$ <i>S</i> (5)
+51.568579	5873.746	3.7	¹⁶ O ¹⁸ O	$v_{0\leftarrow 0}$ <i>sS</i> (8, 8)
+51.057569	5873.922	5.3	¹⁶ O ¹⁷ O	$v_{0\leftarrow 0}$ <i>sR</i> (8, 8)
+50.872888	5873.986	4.4	¹⁶ O ¹⁶ O	$v_{0\leftarrow 0}$ <i>sR</i> (8, 7)
+50.001811	5874.286	4.5	¹⁴ N ¹⁵ N	$v_{0\leftarrow 0}$ <i>S</i> (5)
+49.634960	5874.413	5.4	¹⁶ O ¹⁸ O	$v_{0\leftarrow 0}$ <i>sR</i> (8, 8)
+49.434936	5874.482	5.3	¹⁶ O ¹⁷ O	$v_{0\leftarrow 0}$ <i>sR</i> (8, 7)
+49.141739	5874.583	4.5	¹² C ¹⁶ O ¹⁶ O	$v_{0\leftarrow 0}$ <i>S</i> (30)
+48.857001	5874.681	2.4	¹⁶ O ¹⁶ O	$v_{0\leftarrow 0}$ <i>sS</i> (7, 7)
+48.162367	5874.921	5.3	¹⁶ O ¹⁸ O	$v_{0\leftarrow 0}$ <i>sR</i> (8, 7)
+47.418644	5875.178	nan	¹⁶ O ¹⁷ O	$v_{0\leftarrow 0}$ <i>sS</i> (7, 7)
+46.911526	5875.353	4.9	¹⁶ O ¹⁶ O	$v_{0\leftarrow 0}$ <i>sR</i> (7, 7)
+46.145591	5875.617	nan	¹⁶ O ¹⁸ O	$v_{0\leftarrow 0}$ <i>sS</i> (7, 7)
+46.025343	5875.659	nan	¹² C ¹⁶ O ¹⁶ O	$v_{0\leftarrow 0}$ <i>S</i> (28)
+45.473414	5875.849	5.5	¹⁶ O ¹⁷ O	$v_{0\leftarrow 0}$ <i>sR</i> (7, 7)
+44.200706	5876.289	4.8	¹⁶ O ¹⁸ O	$v_{0\leftarrow 0}$ <i>sR</i> (7, 7)
+43.847900	5876.410	2.6	¹⁶ O ¹⁷ O	$v_{0\leftarrow 0}$ <i>sR</i> (7, 6)
+43.763155	5876.440	2.5	¹⁴ N ¹⁴ N	$v_{0\leftarrow 0}$ <i>S</i> (4)
+42.908216	5876.735	4.7	¹² C ¹⁶ O ¹⁶ O	$v_{0\leftarrow 0}$ <i>S</i> (26)
+42.725397	5876.798	5.2	¹⁶ O ¹⁸ O	$v_{0\leftarrow 0}$ <i>sR</i> (7, 6)
+42.312062	5876.941	4.3	¹⁴ N ¹⁵ N	$v_{0\leftarrow 0}$ <i>S</i> (4)
+41.844357	5877.102	5.1	¹⁶ O ¹⁷ O	$v_{0\leftarrow 0}$ <i>sS</i> (6, 6)
+40.720842	5877.490	4.7	¹⁶ O ¹⁸ O	$v_{0\leftarrow 0}$ <i>sS</i> (6, 6)
+39.886439	5877.779	4.9	¹⁶ O ¹⁷ O	$v_{0\leftarrow 0}$ <i>sR</i> (6, 6)
+39.790408	5877.812	4.6	¹² C ¹⁶ O ¹⁶ O	$v_{0\leftarrow 0}$ <i>S</i> (24)
+39.356529	5877.962	3.9	¹⁶ O ¹⁶ O	$v_{0\leftarrow 0}$ <i>sR</i> (6, 5)
+38.763794	5878.167	5.2	¹⁶ O ¹⁸ O	$v_{0\leftarrow 0}$ <i>sR</i> (6, 6)
+38.257827	5878.341	5.0	¹⁶ O ¹⁷ O	$v_{0\leftarrow 0}$ <i>sR</i> (6, 5)

TABLE V. (*Continued.*)

$\Delta\nu$ (cm ⁻¹)	λ_{vac} (Å)	$\log(\frac{I_*}{I})$	Molecule	Transition
+37.368787	5878.649	2.5	¹⁶ O ¹⁶ O	$v_{0\leftarrow 0}$ <i>S S</i> (5, 5)
+37.285569	5878.677	2.6	¹⁶ O ¹⁸ O	$v_{0\leftarrow 0}$ <i>S R</i> (6, 5)
+36.671969	5878.889	4.2	¹² C ¹⁶ O ¹⁶ O	$v_{0\leftarrow 0}$ <i>S</i> (22)
+36.268428	5879.029	4.5	¹⁶ O ¹⁷ O	$v_{0\leftarrow 0}$ <i>S S</i> (5, 5)
+35.808290	5879.188	2.6	¹⁴ N ¹⁴ N	$v_{0\leftarrow 0}$ <i>S</i> (3)
+35.395281	5879.331	4.0	¹⁶ O ¹⁶ O	$v_{0\leftarrow 0}$ <i>S R</i> (5, 5)
+35.294538	5879.366	4.4	¹⁶ O ¹⁸ O	$v_{0\leftarrow 0}$ <i>S S</i> (5, 5)
+34.620898	5879.598	4.5	¹⁴ N ¹⁵ N	$v_{0\leftarrow 0}$ <i>S</i> (3)
+34.296417	5879.711	5.6	¹⁶ O ¹⁷ O	$v_{0\leftarrow 0}$ <i>S R</i> (5, 5)
+33.552948	5879.968	4.8	¹² C ¹⁶ O ¹⁶ O	$v_{0\leftarrow 0}$ <i>S</i> (20)
+33.324017	5880.047	5.6	¹⁶ O ¹⁸ O	$v_{0\leftarrow 0}$ <i>S R</i> (5, 5)
+32.664165	5880.275	5.7	¹⁶ O ¹⁷ O	$v_{0\leftarrow 0}$ <i>S R</i> (5, 4)
+31.842377	5880.559	5.6	¹⁶ O ¹⁸ O	$v_{0\leftarrow 0}$ <i>S R</i> (5, 4)
+30.691076	5880.957	nan	¹⁶ O ¹⁷ O	$v_{0\leftarrow 0}$ <i>S S</i> (4, 4)
+30.433391	5881.046	nan	¹² C ¹⁶ O ¹⁶ O	$v_{0\leftarrow 0}$ <i>S</i> (18)
+29.866888	5881.242	5.4	¹⁶ O ¹⁸ O	$v_{0\leftarrow 0}$ <i>S S</i> (4, 4)
+28.702800	5881.645	nan	¹⁶ O ¹⁷ O	$v_{0\leftarrow 0}$ <i>S R</i> (4, 4)
+27.880868	5881.929	3.2	¹⁶ O ¹⁸ O	$v_{0\leftarrow 0}$ <i>S R</i> (4, 4)
+27.852182	5881.939	3.2	¹⁴ N ¹⁴ N	$v_{0\leftarrow 0}$ <i>S</i> (2)
+27.824102	5881.949	3.3	¹⁶ O ¹⁶ O	$v_{0\leftarrow 0}$ <i>S R</i> (4, 3)
+27.313355	5882.126	5.7	¹² C ¹⁶ O ¹⁶ O	$v_{0\leftarrow 0}$ <i>S</i> (16)
+27.065676	5882.211	nan	¹⁶ O ¹⁷ O	$v_{0\leftarrow 0}$ <i>S R</i> (4, 3)
+26.928571	5882.259	nan	¹⁴ N ¹⁵ N	$v_{0\leftarrow 0}$ <i>S</i> (2)
+26.394667	5882.444	nan	¹⁶ O ¹⁸ O	$v_{0\leftarrow 0}$ <i>S R</i> (4, 3)
+25.874533	5882.624	3.4	¹⁶ O ¹⁶ O	$v_{0\leftarrow 0}$ <i>S S</i> (3, 3)
+25.112522	5882.887	5.3	¹⁶ O ¹⁷ O	$v_{0\leftarrow 0}$ <i>S S</i> (3, 3)
+24.438099	5883.121	nan	¹⁶ O ¹⁸ O	$v_{0\leftarrow 0}$ <i>S S</i> (3, 3)
+24.192885	5883.206	5.4	¹² C ¹⁶ O ¹⁶ O	$v_{0\leftarrow 0}$ <i>S</i> (14)
+23.862939	5883.320	4.9	¹⁶ O ¹⁶ O	$v_{0\leftarrow 0}$ <i>S R</i> (3, 3)
+23.104349	5883.582	nan	¹⁶ O ¹⁷ O	$v_{0\leftarrow 0}$ <i>S R</i> (3, 3)
+22.433194	5883.815	nan	¹⁶ O ¹⁸ O	$v_{0\leftarrow 0}$ <i>S R</i> (3, 3)
+21.459431	5884.152	nan	¹⁶ O ¹⁷ O	$v_{0\leftarrow 0}$ <i>S R</i> (3, 2)
+21.072031	5884.286	nan	¹² C ¹⁶ O ¹⁶ O	$v_{0\leftarrow 0}$ <i>S</i> (12)
+20.939713	5884.332	5.1	¹⁶ O ¹⁸ O	$v_{0\leftarrow 0}$ <i>S R</i> (3, 2)
+19.895107	5884.694	3.7	¹⁴ N ¹⁴ N	$v_{0\leftarrow 0}$ <i>S</i> (1)
+19.532983	5884.819	5.3	¹⁶ O ¹⁷ O	$v_{0\leftarrow 0}$ <i>S S</i> (2, 2)
+19.235339	5884.922	5.4	¹⁴ N ¹⁵ N	$v_{0\leftarrow 0}$ <i>S</i> (1)
+19.008378	5885.001	5.5	¹⁶ O ¹⁸ O	$v_{0\leftarrow 0}$ <i>S S</i> (2, 2)
+17.950841	5885.367	nan	¹² C ¹⁶ O ¹⁶ O	$v_{0\leftarrow 0}$ <i>S</i> (10)
+17.498134	5885.524	5.1	¹⁶ O ¹⁷ O	$v_{0\leftarrow 0}$ <i>S R</i> (2, 2)
+16.978269	5885.704	5.5	¹⁶ O ¹⁸ O	$v_{0\leftarrow 0}$ <i>S R</i> (2, 2)
+16.252887	5885.955	4.2	¹⁶ O ¹⁶ O	$v_{0\leftarrow 0}$ <i>S R</i> (2, 1)
+15.837330	5886.099	nan	¹⁶ O ¹⁷ O	$v_{0\leftarrow 0}$ <i>S R</i> (2, 1)
+15.469975	5886.226	5.1	¹⁶ O ¹⁸ O	$v_{0\leftarrow 0}$ <i>S R</i> (2, 1)
+14.829368	5886.448	nan	¹² C ¹⁶ O ¹⁶ O	$v_{0\leftarrow 0}$ <i>S</i> (8)
+14.376096	5886.605	3.8	¹⁶ O ¹⁶ O	$v_{0\leftarrow 0}$ <i>S S</i> (1, 1)
+13.952677	5886.752	5.0	¹⁶ O ¹⁷ O	$v_{0\leftarrow 0}$ <i>S S</i> (1, 1)
+13.577931	5886.882	nan	¹⁶ O ¹⁸ O	$v_{0\leftarrow 0}$ <i>S S</i> (1, 1)
+12.291779	5887.328	4.3	¹⁶ O ¹⁶ O	$v_{0\leftarrow 0}$ <i>S R</i> (1, 1)
+11.937341	5887.451	3.6	¹⁴ N ¹⁴ N	$v_{0\leftarrow 0}$ <i>S</i> (0)
+11.876054	5887.472	3.7	¹⁶ O ¹⁷ O	$v_{0\leftarrow 0}$ <i>S R</i> (1, 1)
+11.707658	5887.530	5.1	¹² C ¹⁶ O ¹⁶ O	$v_{0\leftarrow 0}$ <i>S</i> (6)
+11.541462	5887.588	5.0	¹⁴ N ¹⁵ N	$v_{0\leftarrow 0}$ <i>S</i> (0)
+11.508553	5887.599	5.0	¹⁶ O ¹⁸ O	$v_{0\leftarrow 0}$ <i>S R</i> (1, 1)
+10.167662	5888.064	4.9	¹⁶ O ¹⁷ O	$v_{0\leftarrow 0}$ <i>S R</i> (1, 0)
+9.955987	5888.137	5.0	¹⁶ O ¹⁸ O	$v_{0\leftarrow 0}$ <i>S R</i> (1, 0)
+8.585765	5888.613	nan	¹² C ¹⁶ O ¹⁶ O	$v_{0\leftarrow 0}$ <i>S</i> (4)
+5.463734	5889.695	4.8	¹² C ¹⁶ O ¹⁶ O	$v_{0\leftarrow 0}$ <i>S</i> (2)

TABLE V. (*Continued.*)

$\Delta\nu$ (cm ⁻¹)	λ_{vac} (Å)	$\log(\frac{I_*}{I})$	Molecule	Transition
+3.961085	5890.217	5.5	¹⁶ O ¹⁶ O	$\nu_{0\leftarrow 0}$ $\varrho R(0, 1)$
+2.341614	5890.779	4.6	¹² C ¹⁶ O ¹⁶ O	$\nu_{0\leftarrow 0}$ $S(0)$
+2.157456	5890.842	4.2	¹⁶ O ¹⁶ O	$\nu_{0\leftarrow 0}$ $\varrho P(22, 21)$
+2.139072	5890.849	3.9	¹⁶ O ¹⁶ O	$\nu_{0\leftarrow 0}$ $\varrho P(20, 19)$
+2.120418	5890.855	3.9	¹⁶ O ¹⁶ O	$\nu_{0\leftarrow 0}$ $\varrho P(18, 17)$
+2.101386	5890.862	3.8	¹⁶ O ¹⁶ O	$\nu_{0\leftarrow 0}$ $\varrho P(16, 15)$
+2.084317	5890.868	3.7	¹⁶ O ¹⁶ O	$\nu_{0\leftarrow 0}$ $\varrho R(2, 3)$
+2.081815	5890.869	3.7	¹⁶ O ¹⁶ O	$\nu_{0\leftarrow 0}$ $\varrho P(14, 13)$
+2.061431	5890.876	3.7	¹⁶ O ¹⁶ O	$\nu_{0\leftarrow 0}$ $\varrho P(12, 11)$
+2.039763	5890.883	3.7	¹⁶ O ¹⁶ O	$\nu_{0\leftarrow 0}$ $\varrho P(10, 9)$
+2.015887	5890.892	3.7	¹⁶ O ¹⁶ O	$\nu_{0\leftarrow 0}$ $\varrho P(8, 7)$
+2.011594	5890.893	3.7	¹⁶ O ¹⁶ O	$\nu_{0\leftarrow 0}$ $\varrho R(4, 5)$
+1.987742	5890.901	3.8	¹⁶ O ¹⁶ O	$\nu_{0\leftarrow 0}$ $\varrho P(6, 5)$
+1.973506	5890.906	3.8	¹⁶ O ¹⁶ O	$\nu_{0\leftarrow 0}$ $\varrho R(6, 7)$
+1.949569	5890.915	3.8	¹⁶ O ¹⁶ O	$\nu_{0\leftarrow 0}$ $\varrho P(4, 3)$
+1.945475	5890.916	3.8	¹⁶ O ¹⁶ O	$\nu_{0\leftarrow 0}$ $\varrho R(8, 9)$
+1.921746	5890.924	3.8	¹⁶ O ¹⁶ O	$\nu_{0\leftarrow 0}$ $\varrho R(10, 11)$
+1.900255	5890.932	3.9	¹⁶ O ¹⁶ O	$\nu_{0\leftarrow 0}$ $\varrho R(12, 13)$
+1.880080	5890.939	3.9	¹⁶ O ¹⁶ O	$\nu_{0\leftarrow 0}$ $\varrho R(14, 15)$
+1.876791	5890.940	3.9	¹⁶ O ¹⁶ O	$\nu_{0\leftarrow 0}$ $\varrho P(2, 1)$
+1.860748	5890.945	3.9	¹⁶ O ¹⁶ O	$\nu_{0\leftarrow 0}$ $\varrho R(16, 17)$
+1.841987	5890.952	3.9	¹⁶ O ¹⁶ O	$\nu_{0\leftarrow 0}$ $\varrho R(18, 19)$
+1.823634	5890.958	4.2	¹⁶ O ¹⁶ O	$\nu_{0\leftarrow 0}$ $\varrho R(20, 21)$
-1.823634	5892.224	3.9	¹⁶ O ¹⁶ O	$\nu_{0\leftarrow 0}$ $\varrho R(20, 21)$
-1.841987	5892.231	3.9	¹⁶ O ¹⁶ O	$\nu_{0\leftarrow 0}$ $\varrho R(18, 19)$
-1.860748	5892.237	3.8	¹⁶ O ¹⁶ O	$\nu_{0\leftarrow 0}$ $\varrho R(16, 17)$
-1.876791	5892.243	3.8	¹⁶ O ¹⁶ O	$\nu_{0\leftarrow 0}$ $\varrho P(2, 1)$
-1.880080	5892.244	3.8	¹⁶ O ¹⁶ O	$\nu_{0\leftarrow 0}$ $\varrho R(14, 15)$
-1.900255	5892.251	3.8	¹⁶ O ¹⁶ O	$\nu_{0\leftarrow 0}$ $\varrho R(12, 13)$
-1.921746	5892.258	3.8	¹⁶ O ¹⁶ O	$\nu_{0\leftarrow 0}$ $\varrho R(10, 11)$
-1.945475	5892.267	3.7	¹⁶ O ¹⁶ O	$\nu_{0\leftarrow 0}$ $\varrho R(8, 9)$
-1.949569	5892.268	3.7	¹⁶ O ¹⁶ O	$\nu_{0\leftarrow 0}$ $\varrho P(4, 3)$
-1.973506	5892.276	3.7	¹⁶ O ¹⁶ O	$\nu_{0\leftarrow 0}$ $\varrho R(6, 7)$
-1.987742	5892.281	3.7	¹⁶ O ¹⁶ O	$\nu_{0\leftarrow 0}$ $\varrho P(6, 5)$
-2.011594	5892.290	3.6	¹⁶ O ¹⁶ O	$\nu_{0\leftarrow 0}$ $\varrho R(4, 5)$
-2.015887	5892.291	3.6	¹⁶ O ¹⁶ O	$\nu_{0\leftarrow 0}$ $\varrho P(8, 7)$
-2.039763	5892.299	3.6	¹⁶ O ¹⁶ O	$\nu_{0\leftarrow 0}$ $\varrho P(10, 9)$
-2.061431	5892.307	3.7	¹⁶ O ¹⁶ O	$\nu_{0\leftarrow 0}$ $\varrho P(12, 11)$
-2.081815	5892.314	3.8	¹⁶ O ¹⁶ O	$\nu_{0\leftarrow 0}$ $\varrho P(14, 13)$
-2.084317	5892.315	3.8	¹⁶ O ¹⁶ O	$\nu_{0\leftarrow 0}$ $\varrho R(2, 3)$
-2.101386	5892.321	3.8	¹⁶ O ¹⁶ O	$\nu_{0\leftarrow 0}$ $\varrho P(16, 15)$
-2.120418	5892.327	3.8	¹⁶ O ¹⁶ O	$\nu_{0\leftarrow 0}$ $\varrho P(18, 17)$
-2.139072	5892.334	3.9	¹⁶ O ¹⁶ O	$\nu_{0\leftarrow 0}$ $\varrho P(20, 19)$
-2.157456	5892.340	3.9	¹⁶ O ¹⁶ O	$\nu_{0\leftarrow 0}$ $\varrho P(22, 21)$
-2.341616	5892.404	4.2	¹² C ¹⁶ O ¹⁶ O	$\nu_{0\leftarrow 0}$ $S(0)$
-3.961085	5892.966	5.0	¹⁶ O ¹⁶ O	$\nu_{0\leftarrow 0}$ $\varrho R(0, 1)$
-5.463734	5893.488	5.1	¹² C ¹⁶ O ¹⁶ O	$\nu_{0\leftarrow 0}$ $S(2)$
-8.585765	5894.573	5.5	¹² C ¹⁶ O ¹⁶ O	$\nu_{0\leftarrow 0}$ $S(4)$
-9.955987	5895.049	4.9	¹⁶ O ¹⁸ O	$\nu_{0\leftarrow 0}$ $sR(1, 0)$
-10.167662	5895.123	nan	¹⁶ O ¹⁷ O	$\nu_{0\leftarrow 0}$ $sR(1, 0)$
-11.508553	5895.589	nan	¹⁶ O ¹⁸ O	$\nu_{0\leftarrow 0}$ $sR(1, 1)$
-11.541462	5895.600	5.3	¹⁴ N ¹⁵ N	$\nu_{0\leftarrow 0}$ $S(0)$
-11.707660	5895.658	4.9	¹² C ¹⁶ O ¹⁶ O	$\nu_{0\leftarrow 0}$ $S(6)$
-11.876054	5895.716	3.7	¹⁶ O ¹⁷ O	$\nu_{0\leftarrow 0}$ $sR(1, 1)$
-11.937340	5895.738	3.5	¹⁴ N ¹⁴ N	$\nu_{0\leftarrow 0}$ $S(0)$
-12.291779	5895.861	4.3	¹⁶ O ¹⁶ O	$\nu_{0\leftarrow 0}$ $sR(1, 1)$
-13.577931	5896.308	nan	¹⁶ O ¹⁸ O	$\nu_{0\leftarrow 0}$ $sS(1, 1)$
-13.952677	5896.438	5.4	¹⁶ O ¹⁷ O	$\nu_{0\leftarrow 0}$ $sS(1, 1)$

TABLE V. (*Continued.*)

$\Delta\nu$ (cm ⁻¹)	λ_{vac} (Å)	$\log(\frac{I_*}{I})$	Molecule	Transition
-14.376096	5896.585	3.8	¹⁶ O ¹⁶ O	$v_{0 \leftarrow 0}$ $^sS(1, 1)$
-14.829367	5896.743	nan	¹² C ¹⁶ O ¹⁶ O	$v_{0 \leftarrow 0}$ $S(8)$
-15.469975	5896.966	5.3	¹⁶ O ¹⁸ O	$v_{0 \leftarrow 0}$ $^sR(2, 1)$
-15.837330	5897.094	5.1	¹⁶ O ¹⁷ O	$v_{0 \leftarrow 0}$ $^sR(2, 1)$
-16.252887	5897.238	4.2	¹⁶ O ¹⁶ O	$v_{0 \leftarrow 0}$ $^sR(2, 1)$
-16.978269	5897.490	5.0	¹⁶ O ¹⁸ O	$v_{0 \leftarrow 0}$ $^sR(2, 2)$
-17.498134	5897.671	nan	¹⁶ O ¹⁷ O	$v_{0 \leftarrow 0}$ $^sR(2, 2)$
-17.950842	5897.829	nan	¹² C ¹⁶ O ¹⁶ O	$v_{0 \leftarrow 0}$ $S(10)$
-19.008378	5898.197	nan	¹⁶ O ¹⁸ O	$v_{0 \leftarrow 0}$ $^sS(2, 2)$
-19.235338	5898.276	5.4	¹⁴ N ¹⁵ N	$v_{0 \leftarrow 0}$ $S(1)$
-19.532983	5898.379	nan	¹⁶ O ¹⁷ O	$v_{0 \leftarrow 0}$ $^sS(2, 2)$
-19.895107	5898.505	3.6	¹⁴ N ¹⁴ N	$v_{0 \leftarrow 0}$ $S(1)$
-20.939713	5898.869	nan	¹⁶ O ¹⁸ O	$v_{0 \leftarrow 0}$ $^sR(3, 2)$
-21.072030	5898.915	5.2	¹² C ¹⁶ O ¹⁶ O	$v_{0 \leftarrow 0}$ $S(12)$
-21.459431	5899.049	5.2	¹⁶ O ¹⁷ O	$v_{0 \leftarrow 0}$ $^sR(3, 2)$
-22.433194	5899.388	5.2	¹⁶ O ¹⁸ O	$v_{0 \leftarrow 0}$ $^sR(3, 3)$
-23.104349	5899.622	5.4	¹⁶ O ¹⁷ O	$v_{0 \leftarrow 0}$ $^sR(3, 3)$
-23.862939	5899.886	3.7	¹⁶ O ¹⁶ O	$v_{0 \leftarrow 0}$ $^sR(3, 3)$
-24.192886	5900.001	4.6	¹² C ¹⁶ O ¹⁶ O	$v_{0 \leftarrow 0}$ $S(14)$
-24.438099	5900.086	4.9	¹⁶ O ¹⁸ O	$v_{0 \leftarrow 0}$ $^sS(3, 3)$
-25.112522	5900.321	5.2	¹⁶ O ¹⁷ O	$v_{0 \leftarrow 0}$ $^sS(3, 3)$
-25.874533	5900.586	2.5	¹⁶ O ¹⁶ O	$v_{0 \leftarrow 0}$ $^sS(3, 3)$
-26.394667	5900.767	5.0	¹⁶ O ¹⁸ O	$v_{0 \leftarrow 0}$ $^sR(4, 3)$
-26.928571	5900.953	4.5	¹⁴ N ¹⁵ N	$v_{0 \leftarrow 0}$ $S(2)$
-27.065676	5901.001	5.0	¹⁶ O ¹⁷ O	$v_{0 \leftarrow 0}$ $^sR(4, 3)$
-27.313356	5901.087	4.5	¹² C ¹⁶ O ¹⁶ O	$v_{0 \leftarrow 0}$ $S(16)$
-27.824102	5901.265	2.4	¹⁶ O ¹⁶ O	$v_{0 \leftarrow 0}$ $^sR(4, 3)$
-27.852181	5901.275	2.3	¹⁴ N ¹⁴ N	$v_{0 \leftarrow 0}$ $S(2)$
-27.880868	5901.285	2.4	¹⁶ O ¹⁸ O	$v_{0 \leftarrow 0}$ $^sR(4, 4)$
-28.702800	5901.571	5.2	¹⁶ O ¹⁷ O	$v_{0 \leftarrow 0}$ $^sR(4, 4)$
-29.866888	5901.977	4.9	¹⁶ O ¹⁸ O	$v_{0 \leftarrow 0}$ $^sS(4, 4)$
-30.433392	5902.174	4.6	¹² C ¹⁶ O ¹⁶ O	$v_{0 \leftarrow 0}$ $S(18)$
-30.691076	5902.264	5.2	¹⁶ O ¹⁷ O	$v_{0 \leftarrow 0}$ $^sS(4, 4)$
-31.842377	5902.665	5.4	¹⁶ O ¹⁸ O	$v_{0 \leftarrow 0}$ $^sR(5, 4)$
-32.664165	5902.951	5.5	¹⁶ O ¹⁷ O	$v_{0 \leftarrow 0}$ $^sR(5, 4)$
-33.324017	5903.181	5.4	¹⁶ O ¹⁸ O	$v_{0 \leftarrow 0}$ $^sR(5, 5)$
-33.552946	5903.261	4.7	¹² C ¹⁶ O ¹⁶ O	$v_{0 \leftarrow 0}$ $S(20)$
-34.296417	5903.520	5.5	¹⁶ O ¹⁷ O	$v_{0 \leftarrow 0}$ $^sR(5, 5)$
-34.620899	5903.633	4.4	¹⁴ N ¹⁵ N	$v_{0 \leftarrow 0}$ $S(3)$
-35.294538	5903.868	4.3	¹⁶ O ¹⁸ O	$v_{0 \leftarrow 0}$ $^sS(5, 5)$
-35.395281	5903.903	3.9	¹⁶ O ¹⁶ O	$v_{0 \leftarrow 0}$ $^sR(5, 5)$
-35.808290	5904.047	2.6	¹⁴ N ¹⁴ N	$v_{0 \leftarrow 0}$ $S(3)$
-36.268428	5904.207	4.9	¹⁶ O ¹⁷ O	$v_{0 \leftarrow 0}$ $^sS(5, 5)$
-36.671970	5904.348	4.6	¹² C ¹⁶ O ¹⁶ O	$v_{0 \leftarrow 0}$ $S(22)$
-37.285569	5904.562	2.7	¹⁶ O ¹⁸ O	$v_{0 \leftarrow 0}$ $^sR(6, 5)$
-37.368787	5904.591	2.3	¹⁶ O ¹⁶ O	$v_{0 \leftarrow 0}$ $^sS(5, 5)$
-38.257827	5904.901	5.3	¹⁶ O ¹⁷ O	$v_{0 \leftarrow 0}$ $^sR(6, 5)$
-38.763794	5905.077	5.4	¹⁶ O ¹⁸ O	$v_{0 \leftarrow 0}$ $^sR(6, 6)$
-39.356529	5905.284	4.1	¹⁶ O ¹⁶ O	$v_{0 \leftarrow 0}$ $^sR(6, 5)$
-39.790408	5905.435	4.8	¹² C ¹⁶ O ¹⁶ O	$v_{0 \leftarrow 0}$ $S(24)$
-39.886439	5905.469	5.2	¹⁶ O ¹⁷ O	$v_{0 \leftarrow 0}$ $^sR(6, 6)$
-40.720842	5905.760	4.8	¹⁶ O ¹⁸ O	$v_{0 \leftarrow 0}$ $^sS(6, 6)$
-41.844357	5906.152	5.2	¹⁶ O ¹⁷ O	$v_{0 \leftarrow 0}$ $^sS(6, 6)$
-42.312063	5906.315	4.4	¹⁴ N ¹⁵ N	$v_{0 \leftarrow 0}$ $S(4)$
-42.725397	5906.459	5.3	¹⁶ O ¹⁸ O	$v_{0 \leftarrow 0}$ $^sR(7, 6)$
-42.908217	5906.523	4.8	¹² C ¹⁶ O ¹⁶ O	$v_{0 \leftarrow 0}$ $S(26)$
-43.763154	5906.821	2.2	¹⁴ N ¹⁴ N	$v_{0 \leftarrow 0}$ $S(4)$
-43.847900	5906.851	2.6	¹⁶ O ¹⁷ O	$v_{0 \leftarrow 0}$ $^sR(7, 6)$

TABLE V. (*Continued.*)

$\Delta\nu$ (cm ⁻¹)	λ_{vac} (Å)	$\log(\frac{I_*}{I})$	Molecule	Transition
-44.200706	5906.974	4.8	¹⁶ O ¹⁸ O	$\nu_{0\leftarrow 0}$
-45.473414	5907.418	5.4	¹⁶ O ¹⁷ O	$\nu_{0\leftarrow 0}$
-46.025345	5907.610	4.9	¹² C ¹⁶ O ¹⁶ O	$\nu_{0\leftarrow 0}$
-46.145591	5907.652	4.8	¹⁶ O ¹⁸ O	$\nu_{0\leftarrow 0}$
-46.911526	5907.920	4.2	¹⁶ O ¹⁶ O	$\nu_{0\leftarrow 0}$
-47.418644	5908.097	5.3	¹⁶ O ¹⁷ O	$\nu_{0\leftarrow 0}$
-48.162367	5908.356	5.2	¹⁶ O ¹⁸ O	$\nu_{0\leftarrow 0}$
-48.857001	5908.599	2.3	¹⁶ O ¹⁶ O	$\nu_{0\leftarrow 0}$
-49.141740	5908.698	4.4	¹² C ¹⁶ O ¹⁶ O	$\nu_{0\leftarrow 0}$
-49.434936	5908.801	5.1	¹⁶ O ¹⁷ O	$\nu_{0\leftarrow 0}$
-49.634960	5908.870	5.2	¹⁶ O ¹⁸ O	$\nu_{0\leftarrow 0}$
-50.001810	5908.999	4.4	¹⁴ N ¹⁵ N	$\nu_{0\leftarrow 0}$
-50.872888	5909.303	4.2	¹⁶ O ¹⁶ O	$\nu_{0\leftarrow 0}$
-51.057569	5909.367	5.2	¹⁶ O ¹⁷ O	$\nu_{0\leftarrow 0}$
-51.568579	5909.546	3.6	¹⁶ O ¹⁸ O	$\nu_{0\leftarrow 0}$
-51.716502	5909.597	2.5	¹⁴ N ¹⁴ N	$\nu_{0\leftarrow 0}$
-52.257355	5909.786	4.9	¹² C ¹⁶ O ¹⁶ O	$\nu_{0\leftarrow 0}$
-52.991071	5910.042	5.3	¹⁶ O ¹⁷ O	$\nu_{0\leftarrow 0}$
-53.596688	5910.254	5.6	¹⁶ O ¹⁸ O	$\nu_{0\leftarrow 0}$
-55.019157	5910.751	5.6	¹⁶ O ¹⁷ O	$\nu_{0\leftarrow 0}$
-55.066607	5910.767	5.6	¹⁶ O ¹⁸ O	$\nu_{0\leftarrow 0}$
-55.372143	5910.874	5.2	¹² C ¹⁶ O ¹⁶ O	$\nu_{0\leftarrow 0}$
-56.638959	5911.317	5.6	¹⁶ O ¹⁷ O	$\nu_{0\leftarrow 0}$
-56.989599	5911.439	4.9	¹⁶ O ¹⁸ O	$\nu_{0\leftarrow 0}$
-57.689878	5911.684	4.4	¹⁴ N ¹⁵ N	$\nu_{0\leftarrow 0}$
-58.415569	5911.938	4.4	¹⁶ O ¹⁶ O	$\nu_{0\leftarrow 0}$
-58.486049	5911.962	4.5	¹² C ¹⁶ O ¹⁶ O	$\nu_{0\leftarrow 0}$
-58.561420	5911.989	5.0	¹⁶ O ¹⁷ O	$\nu_{0\leftarrow 0}$
-59.028406	5912.152	5.1	¹⁶ O ¹⁸ O	$\nu_{0\leftarrow 0}$
-59.668051	5912.376	2.3	¹⁴ N ¹⁴ N	$\nu_{0\leftarrow 0}$
-60.337315	5912.610	2.4	¹⁶ O ¹⁶ O	$\nu_{0\leftarrow 0}$
-60.495603	5912.665	3.5	¹⁶ O ¹⁸ O	$\nu_{0\leftarrow 0}$
-60.600622	5912.702	4.3	¹⁶ O ¹⁷ O	$\nu_{0\leftarrow 0}$
-61.599028	5913.051	5.2	¹² C ¹⁶ O ¹⁶ O	$\nu_{0\leftarrow 0}$
-62.377078	5913.323	4.4	¹⁶ O ¹⁶ O	$\nu_{0\leftarrow 0}$
-62.408442	5913.334	4.4	¹⁶ O ¹⁸ O	$\nu_{0\leftarrow 0}$
-64.129472	5913.936	5.4	¹⁶ O ¹⁷ O	$\nu_{0\leftarrow 0}$
-64.457482	5914.050	5.7	¹⁶ O ¹⁸ O	$\nu_{0\leftarrow 0}$
-64.711027	5914.139	5.4	¹² C ¹⁶ O ¹⁶ O	$\nu_{0\leftarrow 0}$
-65.376009	5914.372	4.4	¹⁴ N ¹⁵ N	$\nu_{0\leftarrow 0}$
-65.921856	5914.562	5.7	¹⁶ O ¹⁸ O	$\nu_{0\leftarrow 0}$
-66.179288	5914.653	5.6	¹⁶ O ¹⁷ O	$\nu_{0\leftarrow 0}$
-67.617529	5915.156	2.5	¹⁴ N ¹⁴ N	$\nu_{0\leftarrow 0}$
-67.821999	5915.227	4.1	¹² C ¹⁶ O ¹⁶ O	$\nu_{0\leftarrow 0}$
-67.824904	5915.228	4.2	¹⁶ O ¹⁸ O	$\nu_{0\leftarrow 0}$
-69.695006	5915.883	5.4	¹⁶ O ¹⁷ O	$\nu_{0\leftarrow 0}$
-69.883823	5915.949	4.7	¹⁶ O ¹⁸ O	$\nu_{0\leftarrow 0}$
-69.907616	5915.957	4.7	¹⁶ O ¹⁶ O	$\nu_{0\leftarrow 0}$
-70.931895	5916.316	5.4	¹² C ¹⁶ O ¹⁶ O	$\nu_{0\leftarrow 0}$
-71.755059	5916.604	2.5	¹⁶ O ¹⁷ O	$\nu_{0\leftarrow 0}$
-71.807871	5916.622	2.4	¹⁶ O ¹⁶ O	$\nu_{0\leftarrow 0}$
-73.059946	5917.061	4.4	¹⁴ N ¹⁵ N	$\nu_{0\leftarrow 0}$
-73.238776	5917.123	5.0	¹⁶ O ¹⁸ O	$\nu_{0\leftarrow 0}$
-73.869302	5917.344	4.7	¹⁶ O ¹⁶ O	$\nu_{0\leftarrow 0}$
-74.040661	5917.404	5.5	¹² C ¹⁶ O ¹⁶ O	$\nu_{0\leftarrow 0}$
-75.257806	5917.830	4.6	¹⁶ O ¹⁷ O	$\nu_{0\leftarrow 0}$
-75.307300	5917.847	4.4	¹⁶ O ¹⁸ O	$\nu_{0\leftarrow 0}$
-75.564661	5917.938	2.3	¹⁴ N ¹⁴ N	$\nu_{0\leftarrow 0}$

TABLE V. (*Continued.*)

$\Delta\nu$ (cm ⁻¹)	λ_{vac} (Å)	$\log(\frac{I_*}{I})$	Molecule	Transition
-77.148252	5918.492	5.6	¹² C ¹⁶ O ¹⁶ O	$v_{0 \leftarrow 0}$ <i>S</i> (48)
-77.327801	5918.555	5.7	¹⁶ O ¹⁷ O	$v_{0 \leftarrow 0}$ <i>sR</i> (13, 12)
-78.649850	5919.018	5.1	¹⁶ O ¹⁸ O	$v_{0 \leftarrow 0}$ <i>sS</i> (13, 13)
-80.254618	5919.581	5.8	¹² C ¹⁶ O ¹⁶ O	$v_{0 \leftarrow 0}$ <i>S</i> (50)
-80.727763	5919.746	4.5	¹⁶ O ¹⁸ O	$v_{0 \leftarrow 0}$ <i>sR</i> (14, 13)
-80.741430	5919.751	4.5	¹⁴ N ¹⁵ N	$v_{0 \leftarrow 0}$ <i>S</i> (9)
-80.817651	5919.778	4.8	¹⁶ O ¹⁷ O	$v_{0 \leftarrow 0}$ <i>sS</i> (13, 13)
-81.386728	5919.977	4.9	¹⁶ O ¹⁶ O	$v_{0 \leftarrow 0}$ <i>sR</i> (13, 13)
-83.266808	5920.636	2.5	¹⁶ O ¹⁶ O	$v_{0 \leftarrow 0}$ <i>sS</i> (13, 13)
-83.509168	5920.721	2.6	¹⁴ N ¹⁴ N	$v_{0 \leftarrow 0}$ <i>S</i> (9)
-84.057921	5920.914	5.0	¹⁶ O ¹⁸ O	$v_{0 \leftarrow 0}$ <i>sS</i> (14, 14)
-85.348623	5921.366	4.9	¹⁶ O ¹⁶ O	$v_{0 \leftarrow 0}$ <i>sR</i> (14, 13)
-86.145050	5921.645	5.9	¹⁶ O ¹⁸ O	$v_{0 \leftarrow 0}$ <i>sR</i> (15, 14)
-86.374323	5921.726	5.6	¹⁶ O ¹⁷ O	$v_{0 \leftarrow 0}$ <i>sS</i> (14, 14)
-88.420203	5922.443	4.6	¹⁴ N ¹⁵ N	$v_{0 \leftarrow 0}$ <i>S</i> (10)
-89.462780	5922.809	5.2	¹⁶ O ¹⁸ O	$v_{0 \leftarrow 0}$ <i>sS</i> (15, 15)
-91.450775	5923.506	2.4	¹⁴ N ¹⁴ N	$v_{0 \leftarrow 0}$ <i>S</i> (10)
-91.558983	5923.544	3.1	¹⁶ O ¹⁸ O	$v_{0 \leftarrow 0}$ <i>sR</i> (16, 15)
-91.927605	5923.674	5.1	¹⁶ O ¹⁷ O	$v_{0 \leftarrow 0}$ <i>sS</i> (15, 15)
-92.851524	5923.998	5.2	¹⁶ O ¹⁶ O	$v_{0 \leftarrow 0}$ <i>sR</i> (15, 15)
-94.712272	5924.651	2.7	¹⁶ O ¹⁶ O	$v_{0 \leftarrow 0}$ <i>sS</i> (15, 15)
-94.864219	5924.704	3.9	¹⁶ O ¹⁸ O	$v_{0 \leftarrow 0}$ <i>sS</i> (16, 16)
-96.096009	5925.137	4.7	¹⁴ N ¹⁵ N	$v_{0 \leftarrow 0}$ <i>S</i> (11)
-96.813658	5925.389	5.2	¹⁶ O ¹⁶ O	$v_{0 \leftarrow 0}$ <i>sR</i> (16, 15)
-96.969381	5925.443	5.9	¹⁶ O ¹⁸ O	$v_{0 \leftarrow 0}$ <i>sR</i> (17, 16)
-97.477275	5925.622	5.8	¹⁶ O ¹⁷ O	$v_{0 \leftarrow 0}$ <i>sS</i> (16, 16)
-99.389204	5926.293	2.8	¹⁴ N ¹⁴ N	$v_{0 \leftarrow 0}$ <i>S</i> (11)
-100.262034	5926.600	5.4	¹⁶ O ¹⁸ O	$v_{0 \leftarrow 0}$ <i>sS</i> (17, 17)
-102.376058	5927.342	6.1	¹⁶ O ¹⁸ O	$v_{0 \leftarrow 0}$ <i>sR</i> (18, 17)
-103.023115	5927.570	5.9	¹⁶ O ¹⁷ O	$v_{0 \leftarrow 0}$ <i>sS</i> (17, 17)
-103.768587	5927.832	4.8	¹⁴ N ¹⁵ N	$v_{0 \leftarrow 0}$ <i>S</i> (12)
-104.300412	5928.019	5.5	¹⁶ O ¹⁶ O	$v_{0 \leftarrow 0}$ <i>sR</i> (17, 17)
-105.656016	5928.495	5.4	¹⁶ O ¹⁸ O	$v_{0 \leftarrow 0}$ <i>sS</i> (18, 18)
-106.142399	5928.666	3.0	¹⁶ O ¹⁶ O	$v_{0 \leftarrow 0}$ <i>sS</i> (17, 17)
-107.324180	5929.081	2.6	¹⁴ N ¹⁴ N	$v_{0 \leftarrow 0}$ <i>S</i> (12)
-107.778821	5929.241	5.2	¹⁶ O ¹⁸ O	$v_{0 \leftarrow 0}$ <i>sR</i> (19, 18)
-108.262817	5929.411	5.4	¹⁶ O ¹⁶ O	$v_{0 \leftarrow 0}$ <i>sR</i> (18, 17)
-108.564908	5929.518	5.8	¹⁶ O ¹⁷ O	$v_{0 \leftarrow 0}$ <i>sS</i> (18, 18)
-111.045957	5930.390	5.6	¹⁶ O ¹⁸ O	$v_{0 \leftarrow 0}$ <i>sS</i> (19, 19)
-111.437678	5930.528	4.9	¹⁴ N ¹⁵ N	$v_{0 \leftarrow 0}$ <i>S</i> (13)
-113.177475	5931.140	6.1	¹⁶ O ¹⁸ O	$v_{0 \leftarrow 0}$ <i>sR</i> (20, 19)
-114.102435	5931.465	5.9	¹⁶ O ¹⁷ O	$v_{0 \leftarrow 0}$ <i>sS</i> (19, 19)
-115.255427	5931.871	3.0	¹⁴ N ¹⁴ N	$v_{0 \leftarrow 0}$ <i>S</i> (13)
-115.731700	5932.038	5.5	¹⁶ O ¹⁶ O	$v_{0 \leftarrow 0}$ <i>sR</i> (19, 19)
-116.431651	5932.285	5.7	¹⁶ O ¹⁸ O	$v_{0 \leftarrow 0}$ <i>sS</i> (20, 20)
-117.555334	5932.680	3.2	¹⁶ O ¹⁶ O	$v_{0 \leftarrow 0}$ <i>sS</i> (19, 19)
-118.571823	5933.038	6.0	¹⁶ O ¹⁸ O	$v_{0 \leftarrow 0}$ <i>sR</i> (21, 20)
-119.103026	5933.225	5.0	¹⁴ N ¹⁵ N	$v_{0 \leftarrow 0}$ <i>S</i> (14)
-119.635475	5933.412	5.8	¹⁶ O ¹⁷ O	$v_{0 \leftarrow 0}$ <i>sS</i> (20, 20)
-119.694406	5933.433	5.7	¹⁶ O ¹⁶ O	$v_{0 \leftarrow 0}$ <i>sR</i> (20, 19)
-121.812890	5934.179	5.8	¹⁶ O ¹⁸ O	$v_{0 \leftarrow 0}$ <i>sS</i> (21, 21)
-123.182669	5934.662	2.8	¹⁴ N ¹⁴ N	$v_{0 \leftarrow 0}$ <i>S</i> (14)
-125.163811	5935.359	6.0	¹⁶ O ¹⁷ O	$v_{0 \leftarrow 0}$ <i>sS</i> (21, 21)
-126.764374	5935.923	5.1	¹⁴ N ¹⁵ N	$v_{0 \leftarrow 0}$ <i>S</i> (15)
-127.189468	5936.073	5.8	¹⁶ O ¹⁸ O	$v_{0 \leftarrow 0}$ <i>sS</i> (22, 22)
-128.949217	5936.693	3.5	¹⁶ O ¹⁶ O	$v_{0 \leftarrow 0}$ <i>sS</i> (21, 21)
-130.687223	5937.306	5.8	¹⁶ O ¹⁷ O	$v_{0 \leftarrow 0}$ <i>sS</i> (22, 22)
-131.105630	5937.453	3.3	¹⁴ N ¹⁴ N	$v_{0 \leftarrow 0}$ <i>S</i> (15)

TABLE V. (*Continued.*)

$\Delta\nu$ (cm ⁻¹)	λ_{vac} (Å)	$\log(\frac{I^*}{I})$	Molecule	Transition
-131.106673	5937.454	3.3	¹⁶ O ¹⁶ O	$v_0 \leftarrow 0$
-132.561178	5937.966	5.9	¹⁶ O ¹⁸ O	$v_0 \leftarrow 0$
-134.421459	5938.622	5.3	¹⁴ N ¹⁵ N	$v_0 \leftarrow 0$
-136.205493	5939.252	6.0	¹⁶ O ¹⁷ O	$v_0 \leftarrow 0$
-137.927811	5939.859	5.9	¹⁶ O ¹⁸ O	$v_0 \leftarrow 0$
-139.024031	5940.246	3.1	¹⁴ N ¹⁴ N	$v_0 \leftarrow 0$
-140.322190	5940.704	3.8	¹⁶ O ¹⁶ O	$v_0 \leftarrow 0$
-141.718404	5941.197	6.0	¹⁶ O ¹⁷ O	$v_0 \leftarrow 0$
-142.074029	5941.323	5.4	¹⁴ N ¹⁵ N	$v_0 \leftarrow 0$
-142.497831	5941.472	5.9	¹⁶ O ¹⁶ O	$v_0 \leftarrow 0$
-143.289160	5941.752	5.9	¹⁶ O ¹⁸ O	$v_0 \leftarrow 0$
-146.937601	5943.040	3.6	¹⁴ N ¹⁴ N	$v_0 \leftarrow 0$
-147.225734	5943.142	5.5	¹⁶ O ¹⁷ O	$v_0 \leftarrow 0$
-148.645020	5943.643	5.8	¹⁶ O ¹⁸ O	$v_0 \leftarrow 0$
-149.721820	5944.023	5.4	¹⁴ N ¹⁵ N	$v_0 \leftarrow 0$
-151.672395	5944.713	4.2	¹⁶ O ¹⁶ O	$v_0 \leftarrow 0$
-152.727264	5945.085	5.7	¹⁶ O ¹⁷ O	$v_0 \leftarrow 0$
-153.995182	5945.534	5.6	¹⁶ O ¹⁸ O	$v_0 \leftarrow 0$
-154.846059	5945.834	3.5	¹⁴ N ¹⁴ N	$v_0 \leftarrow 0$
-157.364578	5946.725	5.3	¹⁴ N ¹⁵ N	$v_0 \leftarrow 0$
-162.749130	5948.630	3.9	¹⁴ N ¹⁴ N	$v_0 \leftarrow 0$
-162.997971	5948.718	4.5	¹⁶ O ¹⁶ O	$v_0 \leftarrow 0$
-165.002043	5949.427	5.1	¹⁴ N ¹⁵ N	$v_0 \leftarrow 0$
-170.646539	5951.426	3.9	¹⁴ N ¹⁴ N	$v_0 \leftarrow 0$
-172.633957	5952.130	5.5	¹⁴ N ¹⁵ N	$v_0 \leftarrow 0$
-174.297064	5952.719	4.9	¹⁶ O ¹⁶ O	$v_0 \leftarrow 0$
-178.538006	5954.222	4.4	¹⁴ N ¹⁴ N	$v_0 \leftarrow 0$
-180.260062	5954.833	5.8	¹⁴ N ¹⁵ N	$v_0 \leftarrow 0$
-185.567812	5956.715	5.4	¹⁶ O ¹⁶ O	$v_0 \leftarrow 0$
-186.423262	5957.019	4.3	¹⁴ N ¹⁴ N	$v_0 \leftarrow 0$
-187.880102	5957.536	6.0	¹⁴ N ¹⁵ N	$v_0 \leftarrow 0$
-194.302024	5959.816	4.9	¹⁴ N ¹⁴ N	$v_0 \leftarrow 0$
-195.493814	5960.239	6.2	¹⁴ N ¹⁵ N	$v_0 \leftarrow 0$
-196.808357	5960.706	5.8	¹⁶ O ¹⁶ O	$v_0 \leftarrow 0$
-202.174021	5962.613	4.8	¹⁴ N ¹⁴ N	$v_0 \leftarrow 0$
-203.100944	5962.943	6.3	¹⁴ N ¹⁵ N	$v_0 \leftarrow 0$
-208.016844	5964.691	6.1	¹⁶ O ¹⁶ O	$v_0 \leftarrow 0$
-210.038971	5965.411	5.4	¹⁴ N ¹⁴ N	$v_0 \leftarrow 0$
-210.701231	5965.647	6.3	¹⁴ N ¹⁵ N	$v_0 \leftarrow 0$
-217.896600	5968.209	5.3	¹⁴ N ¹⁴ N	$v_0 \leftarrow 0$
-219.191412	5968.670	6.3	¹⁶ O ¹⁶ O	$v_0 \leftarrow 0$
-225.746635	5971.006	5.9	¹⁴ N ¹⁴ N	$v_0 \leftarrow 0$
-230.330204	5972.641	6.4	¹⁶ O ¹⁶ O	$v_0 \leftarrow 0$
-233.588797	5973.803	5.9	¹⁴ N ¹⁴ N	$v_0 \leftarrow 0$
-241.422809	5976.600	6.2	¹⁴ N ¹⁴ N	$v_0 \leftarrow 0$
-241.431361	5976.603	6.2	¹⁶ O ¹⁶ O	$v_0 \leftarrow 0$
-249.248396	5979.397	6.3	¹⁴ N ¹⁴ N	$v_0 \leftarrow 0$
-257.065283	5982.193	6.4	¹⁴ N ¹⁴ N	$v_0 \leftarrow 0$
-264.873190	5984.988	6.5	¹⁴ N ¹⁴ N	$v_0 \leftarrow 0$
-1265.100000	6366.084	7.1	¹² C ¹⁶ O ¹⁶ O	
-1285.400000	6374.322	6.1	¹² C ¹⁶ O ¹⁶ O	
-1381.441949	6413.586	7.0	¹⁶ O ¹⁶ O	$v_1 \leftarrow 0$
-1388.200000	6416.367	5.6	¹² C ¹⁶ O ¹⁶ O	
-1394.443469	6418.939	6.7	¹⁶ O ¹⁶ O	$v_1 \leftarrow 0$
-1407.343126	6424.258	6.4	¹⁶ O ¹⁶ O	$v_1 \leftarrow 0$
-1409.500000	6425.148	7.1	¹² C ¹⁶ O ¹⁶ O	
-1420.139060	6429.543	6.1	¹⁶ O ¹⁶ O	$v_1 \leftarrow 0$
-1420.143517	6429.545	6.1	¹⁶ O ¹⁸ O	$v_1 \leftarrow 0$
-1425.983689	6431.960	7.2	¹⁶ O ¹⁸ O	$v_1 \leftarrow 0$

TABLE V. (*Continued.*)

$\Delta\nu$ (cm ⁻¹)	λ_{vac} (Å)	$\log(\frac{I_*}{I})$	Molecule	Transition
-1431.798051	6434.367	7.1	¹⁶ O ¹⁸ O	$v_1 \leftarrow 0$
-1432.829414	6434.794	5.7	¹⁶ O ¹⁶ O	$v_1 \leftarrow 0$
-1437.586395	6436.764	7.1	¹⁶ O ¹⁸ O	$v_1 \leftarrow 0$
-1443.348514	6439.152	7.1	¹⁶ O ¹⁸ O	$v_1 \leftarrow 0$
-1445.412328	6440.008	5.5	¹⁶ O ¹⁶ O	$v_1 \leftarrow 0$
-1449.084203	6441.531	7.0	¹⁶ O ¹⁸ O	$v_1 \leftarrow 0$
-1454.793252	6443.901	7.0	¹⁶ O ¹⁸ O	$v_1 \leftarrow 0$
-1455.778850	6444.310	7.1	¹⁶ O ¹⁶ O	$v_1 \leftarrow 0$
-1457.885947	6445.185	5.2	¹⁶ O ¹⁶ O	$v_1 \leftarrow 0$
-1459.746695	6445.959	7.1	¹⁶ O ¹⁶ O	$v_1 \leftarrow 0$
-1460.475456	6446.261	7.0	¹⁶ O ¹⁸ O	$v_1 \leftarrow 0$
-1466.130608	6448.612	6.9	¹⁶ O ¹⁸ O	$v_1 \leftarrow 0$
-1468.160867	6449.457	7.0	¹⁶ O ¹⁶ O	$v_1 \leftarrow 0$
-1470.248413	6450.325	5.0	¹⁶ O ¹⁶ O	$v_1 \leftarrow 0$
-1471.758500	6450.953	6.9	¹⁶ O ¹⁸ O	$v_1 \leftarrow 0$
-1472.128493	6451.107	7.0	¹⁶ O ¹⁶ O	$v_1 \leftarrow 0$
-1477.358926	6453.285	7.0	¹⁶ O ¹⁸ O	$v_1 \leftarrow 0$
-1480.430658	6454.564	6.9	¹⁶ O ¹⁶ O	$v_1 \leftarrow 0$
-1482.497867	6455.426	4.8	¹⁶ O ¹⁶ O	$v_1 \leftarrow 0$
-1482.931677	6455.606	6.9	¹⁶ O ¹⁸ O	$v_1 \leftarrow 0$
-1484.398122	6456.218	6.9	¹⁶ O ¹⁶ O	$v_1 \leftarrow 0$
-1488.476548	6457.918	7.1	¹⁶ O ¹⁸ O	$v_1 \leftarrow 0$
-1492.586830	6459.633	6.7	¹⁶ O ¹⁶ O	$v_1 \leftarrow 0$
-1493.993330	6460.220	7.0	¹⁶ O ¹⁸ O	$v_1 \leftarrow 0$
-1494.632454	6460.486	4.7	¹⁶ O ¹⁶ O	$v_1 \leftarrow 0$
-1496.554200	6461.289	6.7	¹⁶ O ¹⁶ O	$v_1 \leftarrow 0$
-1499.481818	6462.511	7.2	¹⁶ O ¹⁸ O	$v_1 \leftarrow 0$
-1502.584877	6463.807	7.3	¹⁶ O ¹⁷ O	$v_1 \leftarrow 0$
-1504.628422	6464.661	6.6	¹⁶ O ¹⁶ O	$v_1 \leftarrow 0$
-1505.078987	6464.849	7.1	¹⁶ O ¹⁸ O	$v_1 \leftarrow 0$
-1505.746480	6465.128	7.1	¹⁶ O ¹⁸ O	$v_1 \leftarrow 0$
-1506.384951	6465.395	6.6	¹⁶ O ¹⁸ O	$v_1 \leftarrow 0$
-1506.650315	6465.506	4.6	¹⁶ O ¹⁶ O	$v_1 \leftarrow 0$
-1506.994398	6465.650	6.8	¹⁶ O ¹⁸ O	$v_1 \leftarrow 0$
-1507.574823	6465.893	7.0	¹⁶ O ¹⁸ O	$v_1 \leftarrow 0$
-1508.126225	6466.123	6.9	¹⁶ O ¹⁸ O	$v_1 \leftarrow 0$
-1508.284358	6466.189	7.2	¹⁶ O ¹⁷ O	$v_1 \leftarrow 0$
-1508.595790	6466.320	6.4	¹⁶ O ¹⁶ O	$v_1 \leftarrow 0$
-1508.648604	6466.342	6.5	¹⁶ O ¹⁸ O	$v_1 \leftarrow 0$
-1509.141961	6466.548	6.8	¹⁶ O ¹⁸ O	$v_1 \leftarrow 0$
-1509.606297	6466.742	6.7	¹⁶ O ¹⁸ O	$v_1 \leftarrow 0$
-1510.041610	6466.924	6.6	¹⁶ O ¹⁸ O	$v_1 \leftarrow 0$
-1510.447901	6467.094	6.6	¹⁶ O ¹⁸ O	$v_1 \leftarrow 0$
-1510.825171	6467.252	6.5	¹⁶ O ¹⁸ O	$v_1 \leftarrow 0$
-1511.173418	6467.398	6.5	¹⁶ O ¹⁸ O	$v_1 \leftarrow 0$
-1511.492645	6467.531	6.4	¹⁶ O ¹⁸ O	$v_1 \leftarrow 0$
-1511.782851	6467.652	6.4	¹⁶ O ¹⁸ O	$v_1 \leftarrow 0$
-1512.044035	6467.762	6.3	¹⁶ O ¹⁸ O	$v_1 \leftarrow 0$
-1512.276199	6467.859	6.4	¹⁶ O ¹⁸ O	$v_1 \leftarrow 0$
-1512.479342	6467.944	6.4	¹⁶ O ¹⁸ O	$v_1 \leftarrow 0$
-1512.653464	6468.017	6.4	¹⁶ O ¹⁸ O	$v_1 \leftarrow 0$
-1512.798565	6468.077	6.4	¹⁶ O ¹⁸ O	$v_1 \leftarrow 0$
-1512.914647	6468.126	6.4	¹⁶ O ¹⁸ O	$v_1 \leftarrow 0$
-1513.001708	6468.162	6.4	¹⁶ O ¹⁸ O	$v_1 \leftarrow 0$
-1513.059749	6468.187	6.5	¹⁶ O ¹⁸ O	$v_1 \leftarrow 0$
-1513.954592	6468.561	7.3	¹⁶ O ¹⁷ O	$v_1 \leftarrow 0$
-1516.555582	6469.650	6.4	¹⁶ O ¹⁶ O	$v_1 \leftarrow 0$
-1518.549593	6470.484	4.6	¹⁶ O ¹⁶ O	$v_1 \leftarrow 0$

TABLE V. (*Continued.*)

$\Delta\nu$ (cm ⁻¹)	λ_{vac} (Å)	$\log(\frac{I^*}{I})$	Molecule	Transition
-1519.595361	6470.922	7.3	¹⁶ O ¹⁷ O	$v_1 \leftarrow 0$
-1520.523099	6471.311	6.3	¹⁶ O ¹⁶ O	$v_1 \leftarrow 0$
-1526.492578	6473.812	7.3	¹⁶ O ¹⁸ O	$v_1 \leftarrow 0$
-1527.834158	6474.374	7.3	¹⁶ O ¹⁷ O	$v_1 \leftarrow 0$
-1528.372047	6474.599	6.2	¹⁶ O ¹⁶ O	$v_1 \leftarrow 0$
-1528.408576	6474.615	6.2	¹⁶ O ¹⁷ O	$v_1 \leftarrow 0$
-1528.952761	6474.843	7.2	¹⁶ O ¹⁷ O	$v_1 \leftarrow 0$
-1529.466713	6475.058	7.2	¹⁶ O ¹⁷ O	$v_1 \leftarrow 0$
-1529.950431	6475.261	6.9	¹⁶ O ¹⁷ O	$v_1 \leftarrow 0$
-1530.328430	6475.420	4.8	¹⁶ O ¹⁶ O	$v_1 \leftarrow 0$
-1530.403914	6475.451	5.0	¹⁶ O ¹⁷ O	$v_1 \leftarrow 0$
-1530.827166	6475.629	7.0	¹⁶ O ¹⁷ O	$v_1 \leftarrow 0$
-1531.220183	6475.793	7.0	¹⁶ O ¹⁷ O	$v_1 \leftarrow 0$
-1531.582968	6475.946	6.9	¹⁶ O ¹⁷ O	$v_1 \leftarrow 0$
-1531.806943	6476.040	7.1	¹⁶ O ¹⁸ O	$v_1 \leftarrow 0$
-1531.915520	6476.085	6.9	¹⁶ O ¹⁷ O	$v_1 \leftarrow 0$
-1532.217839	6476.212	6.7	¹⁶ O ¹⁷ O	$v_1 \leftarrow 0$
-1532.340024	6476.263	6.0	¹⁶ O ¹⁶ O	$v_1 \leftarrow 0$
-1532.489926	6476.326	6.8	¹⁶ O ¹⁷ O	$v_1 \leftarrow 0$
-1532.731781	6476.427	6.9	¹⁶ O ¹⁷ O	$v_1 \leftarrow 0$
-1532.943404	6476.516	6.9	¹⁶ O ¹⁷ O	$v_1 \leftarrow 0$
-1533.124795	6476.592	7.0	¹⁶ O ¹⁷ O	$v_1 \leftarrow 0$
-1533.275953	6476.656	6.9	¹⁶ O ¹⁷ O	$v_1 \leftarrow 0$
-1533.396880	6476.706	7.0	¹⁶ O ¹⁷ O	$v_1 \leftarrow 0$
-1533.487575	6476.744	7.0	¹⁶ O ¹⁷ O	$v_1 \leftarrow 0$
-1533.548038	6476.770	7.0	¹⁶ O ¹⁷ O	$v_1 \leftarrow 0$
-1537.091563	6478.257	7.2	¹⁶ O ¹⁸ O	$v_1 \leftarrow 0$
-1538.653159	6478.912	7.1	¹⁶ O ¹⁶ O	$v_1 \leftarrow 0$
-1540.099852	6479.519	5.6	¹⁶ O ¹⁶ O	$v_1 \leftarrow 0$
-1540.708565	6479.775	6.8	¹⁶ O ¹⁶ O	$v_1 \leftarrow 0$
-1541.984969	6480.311	5.2	¹⁶ O ¹⁶ O	$v_1 \leftarrow 0$
-1542.049421	6480.338	5.1	¹⁶ O ¹⁶ O	$v_1 \leftarrow 0$
-1542.346230	6480.463	6.9	¹⁶ O ¹⁸ O	$v_1 \leftarrow 0$
-1542.637487	6480.585	6.4	¹⁶ O ¹⁶ O	$v_1 \leftarrow 0$
-1544.069286	6481.186	5.7	¹⁶ O ¹⁶ O	$v_1 \leftarrow 0$
-1544.439920	6481.342	6.1	¹⁶ O ¹⁶ O	$v_1 \leftarrow 0$
-1546.115864	6482.046	5.7	¹⁶ O ¹⁶ O	$v_1 \leftarrow 0$
-1547.349557	6482.565	7.3	¹⁶ O ¹⁷ O	$v_1 \leftarrow 0$
-1547.570737	6482.657	5.9	¹⁶ O ¹⁸ O	$v_1 \leftarrow 0$
-1547.665316	6482.697	5.3	¹⁶ O ¹⁶ O	$v_1 \leftarrow 0$
-1549.088277	6483.295	5.0	¹⁶ O ¹⁶ O	$v_1 \leftarrow 0$
-1550.384748	6483.840	4.7	¹⁶ O ¹⁶ O	$v_1 \leftarrow 0$
-1550.491122	6483.885	5.5	¹⁶ O ¹⁶ O	$v_1 \leftarrow 0$
-1550.714171	6483.979	6.8	¹⁶ O ¹⁶ O	$v_1 \leftarrow 0$
-1551.427675	6484.279	5.3	¹⁶ O ¹⁶ O	$v_1 \leftarrow 0$
-1551.554727	6484.332	4.4	¹⁶ O ¹⁶ O	$v_1 \leftarrow 0$
-1551.611060	6484.356	4.6	¹⁶ O ¹⁶ O	$v_1 \leftarrow 0$
-1552.238529	6484.620	6.5	¹⁶ O ¹⁶ O	$v_1 \leftarrow 0$
-1552.380182	6484.679	6.1	¹⁶ O ¹⁶ O	$v_1 \leftarrow 0$
-1552.598219	6484.771	4.2	¹⁶ O ¹⁶ O	$v_1 \leftarrow 0$
-1552.764877	6484.841	5.7	¹⁶ O ¹⁸ O	$v_1 \leftarrow 0$
-1552.808936	6484.860	6.1	¹⁶ O ¹⁷ O	$v_1 \leftarrow 0$
-1552.924145	6484.908	6.2	¹⁶ O ¹⁶ O	$v_1 \leftarrow 0$
-1553.020640	6484.949	6.3	¹⁶ O ¹⁶ O	$v_1 \leftarrow 0$
-1553.485423	6485.144	4.0	¹⁶ O ¹⁶ O	$v_1 \leftarrow 0$
-1553.515221	6485.157	4.0	¹⁶ O ¹⁶ O	$v_1 \leftarrow 0$
-1553.530431	6485.163	4.0	¹⁶ O ¹⁶ O	$v_1 \leftarrow 0$
-1553.903957	6485.320	5.8	¹⁶ O ¹⁶ O	$v_1 \leftarrow 0$

TABLE V. (*Continued.*)

$\Delta\nu$ (cm ⁻¹)	λ_{vac} (Å)	$\log(\frac{I^*}{I})$	Molecule	Transition
-1553.924369	6485.329	5.8	¹⁶ O ¹⁶ O	$v_1 \leftarrow 0$
-1554.117331	6485.410	5.4	¹⁶ O ¹⁶ O	$v_1 \leftarrow 0$
-1554.246580	6485.464	4.0	¹⁶ O ¹⁶ O	$v_1 \leftarrow 0$
-1554.267132	6485.473	3.9	¹⁶ O ¹⁶ O	$v_1 \leftarrow 0$
-1554.305738	6485.489	3.9	¹⁶ O ¹⁶ O	$v_1 \leftarrow 0$
-1554.478299	6485.562	5.3	¹⁶ O ¹⁶ O	$v_1 \leftarrow 0$
-1554.699605	6485.655	5.9	¹⁶ O ¹⁶ O	$v_1 \leftarrow 0$
-1554.969769	6485.768	3.8	¹⁶ O ¹⁶ O	$v_1 \leftarrow 0$
-1555.415476	6485.956	4.3	¹⁶ O ¹⁶ O	$v_1 \leftarrow 0$
-1555.507316	6485.995	3.7	¹⁶ O ¹⁶ O	$v_1 \leftarrow 0$
-1555.597036	6486.032	4.2	¹⁶ O ¹⁶ O	$v_1 \leftarrow 0$
-1555.918380	6486.167	3.7	¹⁶ O ¹⁶ O	$v_1 \leftarrow 0$
-1556.066900	6486.230	4.7	¹⁶ O ¹⁶ O	$v_1 \leftarrow 0$
-1556.202963	6486.287	3.9	¹⁶ O ¹⁶ O	$v_1 \leftarrow 0$
-1556.227484	6486.298	3.9	¹⁶ O ¹⁶ O	$v_1 \leftarrow 0$
-1556.330897	6486.341	4.2	¹⁶ O ¹⁶ O	$v_1 \leftarrow 0$
-1556.361065	6486.354	4.2	¹⁶ O ¹⁶ O	$v_1 \leftarrow 0$
-1556.367169	6486.356	4.2	¹⁶ O ¹⁶ O	$v_1 \leftarrow 0$
-1556.915244	6486.587	6.3	¹⁶ O ¹⁶ O	$v_1 \leftarrow 0$
-1557.009532	6486.627	6.4	¹⁶ O ¹⁶ O	$v_1 \leftarrow 0$
-1557.480822	6486.825	6.1	¹⁶ O ¹⁶ O	$v_1 \leftarrow 0$
-1557.523203	6486.843	6.2	¹⁶ O ¹⁶ O	$v_1 \leftarrow 0$
-1557.906122	6487.004	5.9	¹⁶ O ¹⁶ O	$v_1 \leftarrow 0$
-1557.928442	6487.013	5.9	¹⁶ O ¹⁸ O	$v_1 \leftarrow 0$
-1557.929974	6487.014	5.9	¹⁶ O ¹⁶ O	$v_1 \leftarrow 0$
-1558.152532	6487.108	5.7	¹⁶ O ¹⁶ O	$v_1 \leftarrow 0$
-1558.237317	6487.143	5.5	¹⁶ O ¹⁷ O	$v_1 \leftarrow 0$
-1558.287280	6487.164	5.5	¹⁶ O ¹⁶ O	$v_1 \leftarrow 0$
-1558.437033	6487.227	5.8	¹⁶ O ¹⁶ O	$v_1 \leftarrow 0$
-1563.061224	6489.174	7.0	¹⁶ O ¹⁸ O	$v_1 \leftarrow 0$
-1563.634480	6489.415	7.2	¹⁶ O ¹⁷ O	$v_1 \leftarrow 0$
-1568.163017	6491.323	7.1	¹⁶ O ¹⁸ O	$v_1 \leftarrow 0$
-1568.493427	6491.462	5.6	¹⁶ O ¹⁶ O	$v_1 \leftarrow 0$
-1569.000209	6491.676	7.2	¹⁶ O ¹⁷ O	$v_1 \leftarrow 0$
-1570.499467	6492.308	5.1	¹⁶ O ¹⁶ O	$v_1 \leftarrow 0$
-1570.579059	6492.341	5.2	¹⁶ O ¹⁶ O	$v_1 \leftarrow 0$
-1572.455850	6493.132	5.6	¹⁶ O ¹⁶ O	$v_1 \leftarrow 0$
-1573.233613	6493.460	7.0	¹⁶ O ¹⁸ O	$v_1 \leftarrow 0$
-1578.272805	6495.586	7.2	¹⁶ O ¹⁸ O	$v_1 \leftarrow 0$
-1579.778490	6496.221	6.0	¹⁶ O ¹⁶ O	$v_1 \leftarrow 0$
-1581.792913	6497.071	4.7	¹⁶ O ¹⁶ O	$v_1 \leftarrow 0$
-1583.280386	6497.699	7.1	¹⁶ O ¹⁸ O	$v_1 \leftarrow 0$
-1583.742482	6497.894	6.1	¹⁶ O ¹⁶ O	$v_1 \leftarrow 0$
-1588.256147	6499.801	7.2	¹⁶ O ¹⁸ O	$v_1 \leftarrow 0$
-1590.899218	6500.918	6.2	¹⁶ O ¹⁶ O	$v_1 \leftarrow 0$
-1592.876103	6501.753	4.6	¹⁶ O ¹⁶ O	$v_1 \leftarrow 0$
-1593.199882	6501.890	6.7	¹⁶ O ¹⁸ O	$v_1 \leftarrow 0$
-1594.863845	6502.593	6.3	¹⁶ O ¹⁶ O	$v_1 \leftarrow 0$
-1598.111384	6503.967	7.2	¹⁶ O ¹⁸ O	$v_1 \leftarrow 0$
-1601.877641	6505.561	6.4	¹⁶ O ¹⁶ O	$v_1 \leftarrow 0$
-1602.990444	6506.032	7.1	¹⁶ O ¹⁸ O	$v_1 \leftarrow 0$
-1603.826770	6506.386	4.5	¹⁶ O ¹⁶ O	$v_1 \leftarrow 0$
-1605.842657	6507.239	6.5	¹⁶ O ¹⁶ O	$v_1 \leftarrow 0$
-1607.836857	6508.084	7.3	¹⁶ O ¹⁸ O	$v_1 \leftarrow 0$
-1612.650414	6510.123	6.8	¹⁶ O ¹⁸ O	$v_1 \leftarrow 0$
-1612.717497	6510.151	6.6	¹⁶ O ¹⁶ O	$v_1 \leftarrow 0$
-1614.643053	6510.968	4.6	¹⁶ O ¹⁶ O	$v_1 \leftarrow 0$
-1616.682816	6511.832	6.7	¹⁶ O ¹⁶ O	$v_1 \leftarrow 0$

TABLE V. (*Continued.*)

$\Delta\nu$ (cm ⁻¹)	λ_{vac} (Å)	$\log(\frac{I_*}{I})$	Molecule	Transition
-1617.430908	6512.150	7.2	¹⁶ O ¹⁸ O	$v_1 \leftarrow 0$
-1623.418931	6514.690	6.8	¹⁶ O ¹⁶ O	$v_1 \leftarrow 0$
-1625.323092	6515.498	4.7	¹⁶ O ¹⁶ O	$v_1 \leftarrow 0$
-1627.384523	6516.374	6.9	¹⁶ O ¹⁶ O	$v_1 \leftarrow 0$
-1633.980979	6519.176	7.0	¹⁶ O ¹⁶ O	$v_1 \leftarrow 0$
-1635.865027	6519.977	4.8	¹⁶ O ¹⁶ O	$v_1 \leftarrow 0$
-1637.946842	6520.862	6.9	¹⁶ O ¹⁶ O	$v_1 \leftarrow 0$
-1644.402245	6523.608	7.1	¹⁶ O ¹⁶ O	$v_1 \leftarrow 0$
-1646.266999	6524.402	5.0	¹⁶ O ¹⁶ O	$v_1 \leftarrow 0$
-1648.368385	6525.296	7.1	¹⁶ O ¹⁶ O	$v_1 \leftarrow 0$
-1656.527147	6528.772	5.3	¹⁶ O ¹⁶ O	$v_1 \leftarrow 0$
-1666.643611	6533.087	5.5	¹⁶ O ¹⁶ O	$v_1 \leftarrow 0$
-1676.614533	6537.345	5.8	¹⁶ O ¹⁶ O	$v_1 \leftarrow 0$
-1686.438054	6541.546	6.1	¹⁶ O ¹⁶ O	$v_1 \leftarrow 0$
-1696.112315	6545.689	6.5	¹⁶ O ¹⁶ O	$v_1 \leftarrow 0$
-1705.635458	6549.772	6.8	¹⁶ O ¹⁶ O	$v_1 \leftarrow 0$
-1715.005629	6553.794	7.1	¹⁶ O ¹⁶ O	$v_1 \leftarrow 0$
-2108.577124	6727.317	7.5	¹⁴ N ¹⁴ N	$v_1 \leftarrow 0$
-2117.311259	6731.273	7.3	¹⁴ N ¹⁴ N	$v_1 \leftarrow 0$
-2126.017623	6735.220	7.2	¹⁴ N ¹⁴ N	$v_1 \leftarrow 0$
-2134.695948	6739.159	6.9	¹⁴ N ¹⁴ N	$v_1 \leftarrow 0$
-2143.345963	6743.090	7.0	¹⁴ N ¹⁴ N	$v_1 \leftarrow 0$
-2151.967394	6747.012	6.6	¹⁴ N ¹⁴ N	$v_1 \leftarrow 0$
-2152.424408	6747.220	7.3	¹⁴ N ¹⁵ N	$v_1 \leftarrow 0$
-2160.559975	6750.926	6.6	¹⁴ N ¹⁴ N	$v_1 \leftarrow 0$
-2160.610024	6750.949	6.8	¹⁴ N ¹⁵ N	$v_1 \leftarrow 0$
-2168.766849	6754.668	7.3	¹⁴ N ¹⁵ N	$v_1 \leftarrow 0$
-2169.123428	6754.831	6.1	¹⁴ N ¹⁴ N	$v_1 \leftarrow 0$
-2176.894629	6758.378	7.3	¹⁴ N ¹⁵ N	$v_1 \leftarrow 0$
-2177.657486	6758.727	6.2	¹⁴ N ¹⁴ N	$v_1 \leftarrow 0$
-2184.993108	6762.080	7.1	¹⁴ N ¹⁵ N	$v_1 \leftarrow 0$
-2186.161875	6762.614	5.8	¹⁴ N ¹⁴ N	$v_1 \leftarrow 0$
-2193.062035	6765.771	7.1	¹⁴ N ¹⁵ N	$v_1 \leftarrow 0$
-2194.636324	6766.492	5.9	¹⁴ N ¹⁴ N	$v_1 \leftarrow 0$
-2201.101149	6769.453	7.0	¹⁴ N ¹⁵ N	$v_1 \leftarrow 0$
-2203.080559	6770.360	5.4	¹⁴ N ¹⁴ N	$v_1 \leftarrow 0$
-2209.110197	6773.125	7.0	¹⁴ N ¹⁵ N	$v_1 \leftarrow 0$
-2211.494309	6774.219	5.6	¹⁴ N ¹⁴ N	$v_1 \leftarrow 0$
-2217.088922	6776.787	6.9	¹⁴ N ¹⁵ N	$v_1 \leftarrow 0$
-2219.877299	6778.068	5.1	¹⁴ N ¹⁴ N	$v_1 \leftarrow 0$
-2225.037068	6780.440	6.8	¹⁴ N ¹⁵ N	$v_1 \leftarrow 0$
-2228.229258	6781.908	5.3	¹⁴ N ¹⁴ N	$v_1 \leftarrow 0$
-2232.954378	6784.082	6.8	¹⁴ N ¹⁵ N	$v_1 \leftarrow 0$
-2236.549910	6785.737	4.9	¹⁴ N ¹⁴ N	$v_1 \leftarrow 0$
-2240.840598	6787.713	6.8	¹⁴ N ¹⁵ N	$v_1 \leftarrow 0$
-2244.838983	6789.556	5.1	¹⁴ N ¹⁴ N	$v_1 \leftarrow 0$
-2248.695467	6791.334	6.8	¹⁴ N ¹⁵ N	$v_1 \leftarrow 0$
-2253.096206	6793.364	4.7	¹⁴ N ¹⁴ N	$v_1 \leftarrow 0$
-2256.518731	6794.944	6.8	¹⁴ N ¹⁵ N	$v_1 \leftarrow 0$
-2261.321299	6797.162	5.0	¹⁴ N ¹⁴ N	$v_1 \leftarrow 0$
-2264.310130	6798.543	6.9	¹⁴ N ¹⁵ N	$v_1 \leftarrow 0$
-2269.513992	6800.949	4.6	¹⁴ N ¹⁴ N	$v_1 \leftarrow 0$
-2272.069410	6802.132	7.0	¹⁴ N ¹⁵ N	$v_1 \leftarrow 0$
-2277.674008	6804.726	4.9	¹⁴ N ¹⁴ N	$v_1 \leftarrow 0$
-2279.796310	6805.709	7.1	¹⁴ N ¹⁵ N	$v_1 \leftarrow 0$
-2282.980441	6807.184	7.3	¹⁴ N ¹⁵ N	$v_1 \leftarrow 0$
-2283.707350	6807.521	7.2	¹⁴ N ¹⁵ N	$v_1 \leftarrow 0$
-2284.401184	6807.842	7.1	¹⁴ N ¹⁵ N	$v_1 \leftarrow 0$

TABLE V. (*Continued.*)

$\Delta\nu$ (cm ⁻¹)	λ_{vac} (Å)	$\log(\frac{I^*}{I})$	Molecule	Transition
-2285.061948	6808.148	6.9	¹⁴ N ¹⁵ N	$v_1 \leftarrow 0$ Q (19)
-2285.689648	6808.439	5.4	¹⁴ N ¹⁵ N	$v_1 \leftarrow 0$ Q (18)
-2285.801072	6808.491	4.6	¹⁴ N ¹⁴ N	$v_1 \leftarrow 0$ O (6)
-2286.284287	6808.715	6.6	¹⁴ N ¹⁵ N	$v_1 \leftarrow 0$ Q (17)
-2286.845867	6808.975	6.5	¹⁴ N ¹⁵ N	$v_1 \leftarrow 0$ Q (16)
-2287.374396	6809.220	6.3	¹⁴ N ¹⁵ N	$v_1 \leftarrow 0$ Q (15)
-2287.869875	6809.450	6.2	¹⁴ N ¹⁵ N	$v_1 \leftarrow 0$ Q (14)
-2288.332307	6809.665	6.1	¹⁴ N ¹⁵ N	$v_1 \leftarrow 0$ Q (13)
-2288.761696	6809.864	6.0	¹⁴ N ¹⁵ N	$v_1 \leftarrow 0$ Q (12)
-2289.158043	6810.048	5.9	¹⁴ N ¹⁵ N	$v_1 \leftarrow 0$ Q (11)
-2289.521354	6810.216	5.8	¹⁴ N ¹⁵ N	$v_1 \leftarrow 0$ Q (10)
-2289.851627	6810.369	5.7	¹⁴ N ¹⁵ N	$v_1 \leftarrow 0$ Q (9)
-2290.148869	6810.507	5.7	¹⁴ N ¹⁵ N	$v_1 \leftarrow 0$ Q (8)
-2290.413078	6810.630	5.7	¹⁴ N ¹⁵ N	$v_1 \leftarrow 0$ Q (7)
-2290.644256	6810.737	5.6	¹⁴ N ¹⁵ N	$v_1 \leftarrow 0$ Q (6)
-2290.842407	6810.829	5.6	¹⁴ N ¹⁵ N	$v_1 \leftarrow 0$ Q (5)
-2291.007530	6810.905	5.6	¹⁴ N ¹⁵ N	$v_1 \leftarrow 0$ Q (4)
-2291.139629	6810.967	5.6	¹⁴ N ¹⁵ N	$v_1 \leftarrow 0$ Q (3)
-2291.238700	6811.013	5.6	¹⁴ N ¹⁵ N	$v_1 \leftarrow 0$ Q (2)
-2291.304749	6811.043	5.7	¹⁴ N ¹⁵ N	$v_1 \leftarrow 0$ Q (1)
-2291.337773	6811.059	5.9	¹⁴ N ¹⁵ N	$v_1 \leftarrow 0$ Q (0)
-2293.894913	6812.245	4.9	¹⁴ N ¹⁴ N	$v_1 \leftarrow 0$ O (5)
-2301.955250	6815.988	4.7	¹⁴ N ¹⁴ N	$v_1 \leftarrow 0$ O (4)
-2302.780160	6816.371	7.1	¹⁴ N ¹⁵ N	$v_1 \leftarrow 0$ S (0)
-2309.981811	6819.719	5.1	¹⁴ N ¹⁴ N	$v_1 \leftarrow 0$ O (3)
-2310.374967	6819.902	6.8	¹⁴ N ¹⁵ N	$v_1 \leftarrow 0$ S (1)
-2314.791104	6821.956	7.5	¹⁴ N ¹⁴ N	$v_1 \leftarrow 0$ Q (29)
-2315.799602	6822.426	7.0	¹⁴ N ¹⁴ N	$v_1 \leftarrow 0$ Q (28)
-2316.773262	6822.879	7.1	¹⁴ N ¹⁴ N	$v_1 \leftarrow 0$ Q (27)
-2317.712092	6823.316	6.5	¹⁴ N ¹⁴ N	$v_1 \leftarrow 0$ Q (26)
-2317.936099	6823.420	5.1	¹⁴ N ¹⁵ N	$v_1 \leftarrow 0$ S (2)
-2317.974319	6823.438	5.0	¹⁴ N ¹⁴ N	$v_1 \leftarrow 0$ O (2)
-2318.616094	6823.737	6.5	¹⁴ N ¹⁴ N	$v_1 \leftarrow 0$ Q (25)
-2319.485277	6824.141	6.0	¹⁴ N ¹⁴ N	$v_1 \leftarrow 0$ Q (24)
-2320.319649	6824.530	6.0	¹⁴ N ¹⁴ N	$v_1 \leftarrow 0$ Q (23)
-2321.119211	6824.902	5.5	¹⁴ N ¹⁴ N	$v_1 \leftarrow 0$ Q (22)
-2321.883970	6825.259	5.6	¹⁴ N ¹⁴ N	$v_1 \leftarrow 0$ Q (21)
-2322.613933	6825.599	5.1	¹⁴ N ¹⁴ N	$v_1 \leftarrow 0$ Q (20)
-2323.309104	6825.923	5.2	¹⁴ N ¹⁴ N	$v_1 \leftarrow 0$ Q (19)
-2323.969488	6826.230	4.7	¹⁴ N ¹⁴ N	$v_1 \leftarrow 0$ Q (18)
-2324.595086	6826.522	4.8	¹⁴ N ¹⁴ N	$v_1 \leftarrow 0$ Q (17)
-2325.185907	6826.797	4.3	¹⁴ N ¹⁴ N	$v_1 \leftarrow 0$ Q (16)
-2325.463304	6826.926	6.2	¹⁴ N ¹⁵ N	$v_1 \leftarrow 0$ S (3)
-2325.741953	6827.056	4.4	¹⁴ N ¹⁴ N	$v_1 \leftarrow 0$ Q (15)
-2326.263227	6827.299	4.0	¹⁴ N ¹⁴ N	$v_1 \leftarrow 0$ Q (14)
-2326.749736	6827.526	4.2	¹⁴ N ¹⁴ N	$v_1 \leftarrow 0$ Q (13)
-2327.201479	6827.737	3.8	¹⁴ N ¹⁴ N	$v_1 \leftarrow 0$ Q (12)
-2327.618461	6827.931	4.0	¹⁴ N ¹⁴ N	$v_1 \leftarrow 0$ Q (11)
-2328.000685	6828.109	3.6	¹⁴ N ¹⁴ N	$v_1 \leftarrow 0$ Q (10)
-2328.348153	6828.271	3.8	¹⁴ N ¹⁴ N	$v_1 \leftarrow 0$ Q (9)
-2328.660867	6828.417	3.4	¹⁴ N ¹⁴ N	$v_1 \leftarrow 0$ Q (8)
-2328.938830	6828.547	3.7	¹⁴ N ¹⁴ N	$v_1 \leftarrow 0$ Q (7)
-2329.182043	6828.660	3.4	¹⁴ N ¹⁴ N	$v_1 \leftarrow 0$ Q (6)
-2329.390508	6828.757	3.6	¹⁴ N ¹⁴ N	$v_1 \leftarrow 0$ Q (5)
-2329.564226	6828.838	3.4	¹⁴ N ¹⁴ N	$v_1 \leftarrow 0$ Q (4)
-2329.703202	6828.903	3.6	¹⁴ N ¹⁴ N	$v_1 \leftarrow 0$ Q (3)
-2329.807430	6828.952	3.5	¹⁴ N ¹⁴ N	$v_1 \leftarrow 0$ Q (2)
-2329.876917	6828.984	3.6	¹⁴ N ¹⁴ N	$v_1 \leftarrow 0$ Q (1)

TABLE V. (*Continued.*)

$\Delta\nu$ (cm ⁻¹)	λ_{vac} (Å)	$\log(\frac{I^*}{I})$	Molecule	Transition
-2329.911659	6829.000	3.8	¹⁴ N ¹⁴ N	$v_1 \leftarrow 0$ $Q(0)$
-2332.956319	6830.421	6.6	¹⁴ N ¹⁵ N	$v_1 \leftarrow 0$ $S(4)$
-2340.414886	6833.902	6.6	¹⁴ N ¹⁵ N	$v_1 \leftarrow 0$ $S(5)$
-2341.744771	6834.523	5.0	¹⁴ N ¹⁴ N	$v_1 \leftarrow 0$ $S(0)$
-2347.838746	6837.371	6.7	¹⁴ N ¹⁵ N	$v_1 \leftarrow 0$ $S(6)$
-2349.598306	6838.194	5.0	¹⁴ N ¹⁴ N	$v_1 \leftarrow 0$ $S(1)$
-2355.227637	6840.827	6.7	¹⁴ N ¹⁵ N	$v_1 \leftarrow 0$ $S(7)$
-2357.416409	6841.851	4.6	¹⁴ N ¹⁴ N	$v_1 \leftarrow 0$ $S(2)$
-2362.581299	6844.270	6.7	¹⁴ N ¹⁵ N	$v_1 \leftarrow 0$ $S(8)$
-2365.198797	6845.496	4.8	¹⁴ N ¹⁴ N	$v_1 \leftarrow 0$ $S(3)$
-2369.899474	6847.700	6.8	¹⁴ N ¹⁵ N	$v_1 \leftarrow 0$ $S(9)$
-2372.945198	6849.128	4.5	¹⁴ N ¹⁴ N	$v_1 \leftarrow 0$ $S(4)$
-2377.181901	6851.116	6.9	¹⁴ N ¹⁵ N	$v_1 \leftarrow 0$ $S(10)$
-2380.655330	6852.747	4.8	¹⁴ N ¹⁴ N	$v_1 \leftarrow 0$ $S(5)$
-2384.428316	6854.519	7.0	¹⁴ N ¹⁵ N	$v_1 \leftarrow 0$ $S(11)$
-2388.328918	6856.353	4.5	¹⁴ N ¹⁴ N	$v_1 \leftarrow 0$ $S(6)$
-2391.638461	6857.909	7.1	¹⁴ N ¹⁵ N	$v_1 \leftarrow 0$ $S(12)$
-2395.965683	6859.944	4.8	¹⁴ N ¹⁴ N	$v_1 \leftarrow 0$ $S(7)$
-2398.812074	6861.284	7.1	¹⁴ N ¹⁵ N	$v_1 \leftarrow 0$ $S(13)$
-2403.565345	6863.523	4.6	¹⁴ N ¹⁴ N	$v_1 \leftarrow 0$ $S(8)$
-2405.948895	6864.646	7.0	¹⁴ N ¹⁵ N	$v_1 \leftarrow 0$ $S(14)$
-2411.127628	6867.087	4.9	¹⁴ N ¹⁴ N	$v_1 \leftarrow 0$ $S(9)$
-2413.048659	6867.993	7.4	¹⁴ N ¹⁵ N	$v_1 \leftarrow 0$ $S(15)$
-2418.652253	6870.637	4.7	¹⁴ N ¹⁴ N	$v_1 \leftarrow 0$ $S(10)$
-2420.111108	6871.326	7.4	¹⁴ N ¹⁵ N	$v_1 \leftarrow 0$ $S(16)$
-2426.138939	6874.173	6.2	¹⁴ N ¹⁴ N	$v_1 \leftarrow 0$ $S(11)$
-2427.135977	6874.644	7.7	¹⁴ N ¹⁵ N	$v_1 \leftarrow 0$ $S(17)$
-2433.587409	6877.695	4.9	¹⁴ N ¹⁴ N	$v_1 \leftarrow 0$ $S(12)$
-2434.123004	6877.948	7.3	¹⁴ N ¹⁵ N	$v_1 \leftarrow 0$ $S(18)$
-2440.997381	6881.201	5.3	¹⁴ N ¹⁴ N	$v_1 \leftarrow 0$ $S(13)$
-2448.368577	6884.694	5.1	¹⁴ N ¹⁴ N	$v_1 \leftarrow 0$ $S(14)$
-2455.700715	6888.171	5.6	¹⁴ N ¹⁴ N	$v_1 \leftarrow 0$ $S(15)$
-2462.993519	6891.633	5.5	¹⁴ N ¹⁴ N	$v_1 \leftarrow 0$ $S(16)$
-2470.246704	6895.079	6.0	¹⁴ N ¹⁴ N	$v_1 \leftarrow 0$ $S(17)$
-2477.459991	6898.510	5.8	¹⁴ N ¹⁴ N	$v_1 \leftarrow 0$ $S(18)$
-2484.633101	6901.926	6.6	¹⁴ N ¹⁴ N	$v_1 \leftarrow 0$ $S(19)$
-2491.765749	6905.325	6.2	¹⁴ N ¹⁴ N	$v_1 \leftarrow 0$ $S(20)$
-2498.857655	6908.708	6.7	¹⁴ N ¹⁴ N	$v_1 \leftarrow 0$ $S(21)$
-2505.908540	6912.075	6.7	¹⁴ N ¹⁴ N	$v_1 \leftarrow 0$ $S(22)$
-2512.918119	6915.426	7.1	¹⁴ N ¹⁴ N	$v_1 \leftarrow 0$ $S(23)$
-2519.886110	6918.760	7.1	¹⁴ N ¹⁴ N	$v_1 \leftarrow 0$ $S(24)$
-2526.812233	6922.077	7.5	¹⁴ N ¹⁴ N	$v_1 \leftarrow 0$ $S(25)$
-2533.696203	6925.377	7.4	¹⁴ N ¹⁴ N	$v_1 \leftarrow 0$ $S(26)$
-2540.537739	6928.660	7.8	¹⁴ N ¹⁴ N	$v_1 \leftarrow 0$ $S(27)$
-3077.272828	7196.279	7.4	¹⁶ O ¹⁶ O	$v_2 \leftarrow 0$ $\varrho Q(19, 19)$
-3079.607949	7197.488	7.3	¹⁶ O ¹⁶ O	$v_2 \leftarrow 0$ $\varrho Q(17, 17)$
-3081.690633	7198.568	7.2	¹⁶ O ¹⁶ O	$v_2 \leftarrow 0$ $\varrho Q(15, 15)$
-3083.520876	7199.516	7.1	¹⁶ O ¹⁶ O	$v_2 \leftarrow 0$ $\varrho Q(13, 13)$
-3085.098676	7200.334	6.9	¹⁶ O ¹⁶ O	$v_2 \leftarrow 0$ $\varrho Q(11, 11)$
-3086.424031	7201.021	6.9	¹⁶ O ¹⁶ O	$v_2 \leftarrow 0$ $\varrho Q(9, 9)$
-3087.496938	7201.578	6.9	¹⁶ O ¹⁶ O	$v_2 \leftarrow 0$ $\varrho Q(7, 7)$
-3088.317397	7202.003	6.9	¹⁶ O ¹⁶ O	$v_2 \leftarrow 0$ $\varrho Q(5, 5)$
-3088.885408	7202.298	7.0	¹⁶ O ¹⁶ O	$v_2 \leftarrow 0$ $\varrho Q(3, 3)$
-3089.200970	7202.461	7.3	¹⁶ O ¹⁶ O	$v_2 \leftarrow 0$ $\varrho Q(1, 1)$

- [1] R. Foy and A. Labeyrie, Feasibility of adaptive telescope with laser probe, *Astron. Astrophys.* **152**, L29 (1985).
- [2] R. Davies and M. Kasper, Adaptive Optics for Astronomy, *Annu. Rev. Astron. Astrophys.* **50**, 305 (2012).
- [3] R. K. Tyson, Adaptive optics compensation of atmospheric turbulence: The past, the present, and the promise, in *Atmospheric Propagation and Remote Sensing III*, Proc. SPIE **2222**, 404 (1994).
- [4] C. d'Orgeville and G. J. Fetzer, Four generations of sodium guide star lasers for adaptive optics in astronomy and space situational awareness, in *Adaptive Optics Systems V*, Proc. SPIE **9909**, 99090R (2016).
- [5] R. Bacon, M. Accardo, L. Adjali, H. Anwand, S. Bauer, I. Biswas, J. Blaizot, D. Boudon, S. Brau-Nogue, J. Brinchmann *et al.*, The MUSE second-generation VLT instrument, in *Ground-Based and Airborne Instrumentation for Astronomy III*, Proc. SPIE **7735**, 773508 (2010).
- [6] D. B. Calia, W. Hackenberg, R. Holzlöhner, S. Lewis, and T. Pfrommer, The Four-Laser Guide Star Facility: Design considerations and system implementation, *Adv. Opt. Technol.* **3**, 345 (2014).
- [7] R. Arsenault, P.-Y. Madec, J. Paufique, P. La Penna, S. Stroebele, E. Vernet, J.-F. Pirard, W. Hackenberg, H. Kuntschner, J. Kolb *et al.*, The ESO Adaptive Optics Facility under Test, in *Proceedings of the Third AO4ELT Conference* (2013), p. 118.
- [8] F. Delplancke, N. Ageorges, N. Hubin, and C. O'Sullivan, LGS Light Pollution Investigation in Calar Alto, in *ESO Conference and Workshop Proceedings*, Vol. 56 (European Southern Observatory, Garching, Germany, 1999), p. 501.
- [9] S. Chueca Urzay and J. J. Fuensalida, Rayleigh scattering profiles with altitude at Teide Observatory produced by laser, in *Adaptive Optical Systems Technology*, Proc. SPIE, Vol. 4007 (2000), pp. 375–383.
- [10] D. Summers, B. Gregory, P. J. Stomski, Jr., A. Brighton, R. J. Wainscoat, P. L. Wizinowich, W. Gaessler, J. Sebag, C. Boyer, T. Vermeulen *et al.*, Implementation of a laser traffic control system supporting laser guide star adaptive optics on Mauna Kea, in *Adaptive Optical System Technologies II*, Proc. SPIE, Vol. 4839 (2003), pp. 440–451.
- [11] Y. Hayano, W. Gaessler, H. Takami, N. Takato, and Y. Minowa, Rayleigh scatter measurement of Keck LGS by Subaru telescope, in *Adaptive Optical System Technologies II*, Proc. SPIE, Vol. 4839 (2003), pp. 452–455.
- [12] P. Amico, R. D. Campbell, and J. C. Christou, Laser operations at the 8–10m class telescopes Gemini, Keck, and the VLT: Lessons learned, old and new challenges, in *Observatory Operations: Strategies, Processes, and Systems III*, Proc. SPIE, Vol. 7737 (2010), p. 77370A.
- [13] F. P. A. Vogt, D. Bonaccini Calia, W. Hackenberg, C. Opitom, M. Comin, L. Schmidtborek, J. Smoker, I. Blanchard, M. Espinoza Contreras, I. Aranda, J. Milli, Y. L. Jaffe, F. Selman, J. Kolb, P. Hibon, H. Kuntschner, and P.-Y. Madec, Detection and Implications of Laser-Induced Raman Scattering at Astronomical Observatories, *Phys. Rev. X* **7**, 021044 (2017).
- [14] G. Lombardi, D. Bonaccini Calia, M. Centrone, M. Reyes Garcia Talavera, T. Morris, T. Pfrommer, A. Basden, F. Vidal, E. Gendron, G. Rousset *et al.*, Photometry and Spectrum measurements of the Laser Guide Star beam emission at Observatorio del Roque de Los Muchachos with the Gran Telescopio CANARIAS, in *AO4ELT5 Proceedings* (Tenerife, Canary Islands, Spain, 2017).
- [15] E. Marin, G. Sivo, M. Andersen, R. Carrasco, C. Moreno, E. Chirre, A. Hankla, M. Lazo, and G. Lombardi, Confirmation of laser-induced Raman scattering at Cerro Pachon, in *Society of Photo-Optical Instrumentation Engineers (SPIE) Conference Series*, Proc. SPIE, Vol. 10703 (Austin, Texas, 2018), pp. 10703S–10703–7.
- [16] T. Kawaguchi, S. Ozaki, H. Sugai, K. Matsubayashi, T. Hattori, A. Shimono, K. Aoki, Y. Hayano, Y. Minowa, K. Mitsuda *et al.*, A 100 pc-scale fast and dense outflow in the narrow-line Seyfert 1 galaxy IRAS 04576+0912, *Publ. Astron. Soc. Jpn.* **70**, 93 (2018).
- [17] G. Lombardi, D. B. Calia, M. Centrone, A. de Ugarte Postigo, and S. Geier, Laser Guide Star uplink beam: Scattering and Raman emission measurements with the 10.4m Gran Telescopio CANARIAS, *Mon. Not. R. Astron. Soc.* **517**, 201 (2022).
- [18] F. P. A. Vogt, J. Luis Álvarez, D. Bonaccini Calia, W. Hackenberg, P. Bourget, I. Aranda, C. Bellhouse, I. Blanchard, S. Cerdá, C. Cid *et al.*, Raman-scattered laser guide-star photons to monitor the scatter of astronomical telescope mirrors, *Astron. Astrophys.* **618**, L7 (2018).
- [19] P. M. Weilbacher, R. Palsa, O. Streicher, R. Bacon, T. Urrutia, L. Wisotzki, S. Conseil, B. Husemann, A. Jarno, A. Kelz *et al.*, The data processing pipeline for the MUSE instrument, *Astron. Astrophys.* **641**, A28 (2020).
- [20] N. Thatte, M. Tecza, H. Schnetler, B. Neichel, D. Melotte, T. Fusco, V. Ferraro-Wood, F. Clarke, I. Bryson, K. O'Brien *et al.*, HARMONI: The ELT's First-Light Near-infrared and Visible Integral Field Spectrograph, *The Messenger* **182**, 7 (2021).
- [21] T. de Zeeuw, R. Tamai, and J. Liske, Constructing the E-ELT, *The Messenger* **158**, 3 (2014).
- [22] I. Appenzeller, K. Fricke, W. Fürtg, W. Gäßler, R. Häfner, R. Harke, H.-J. Hess, W. Hummel, P. Jürgens, R.-P. Kudritzki *et al.*, Successful commissioning of FORS1 - the first optical instrument on the VLT. *The Messenger* **94**, 1 (1998).
- [23] F. A. Pepe, S. Cristiani, R. Rebolo Lopez, N. C. Santos, A. Amorim, G. Avila, W. Benz, P. Bonifacio, A. Cabral, P. Carvas *et al.*, ESPRESSO: The Echelle spectrograph for rocky exoplanets and stable spectroscopic observations, in *Ground-Based and Airborne Instrumentation for Astronomy III*, Proc. SPIE, Vol. 7735 (2010), p. 77350F.
- [24] F. Pepe, S. Cristiani, R. Rebolo, N. C. Santos, H. Dekker, D. Mégevand, F. M. Zerbini, A. Cabral, P. Molaro, P. Di Marcantonio *et al.*, ESPRESSO—An Echelle spectrograph for rocky exoplanets search and stable spectroscopic observations, *The Messenger* **153**, 6 (2013).
- [25] F. Pepe, S. Cristiani, R. Rebolo, N. C. Santos, H. Dekker, A. Cabral, P. Di Marcantonio, P. Figueira, G. Lo Curto, C. Lovis *et al.*, ESPRESSO at VLT. On-sky performance and first results, *Astron. Astrophys.* **645**, A96 (2021).
- [26] F. P. A. Vogt, F. Kerber, A. Mehner, S. Yu, T. Pfrommer, G. Lo Curto, P. Figueira, D. Parraguez, F. A. Pepe, D. Mégevand, M. Riva, P. Di Marcantonio, C. Lovis, M. Amate, P. Molaro, A. Cabral, and M. R. Z. Osorio, Rotational and Rotational-Vibrational Raman Spectroscopy of Air to Characterize Astronomical Spectrographs, *Phys. Rev. Lett.* **123**, 061101 (2019).

- [27] The official ESO definition for a CLEAR sky transparency is as follows: Less than 10% of the sky (above 30 degrees elevation) covered in clouds, transparency variations under 10%.
- [28] H. Hersbach, B. Bell, P. Berrisford, G. Biavati, A. Horányi, J. Muñoz Sabater, J. Nicolas, C. Peubey, R. Radu, I. Rozum, D. Schepers, A. Simmons, C. Soci, D. Dee, and J.-N. Thépaut (2023): ERA5 hourly data on pressure levels from 1940 to present. Copernicus Climate Change Service (C3S) Climate Data Store (CDS), DOI: [10.24381/cds.bd0915c6](https://doi.org/10.24381/cds.bd0915c6).
- [29] CDSAPI is the official Copernicus Climate Change Service (C3S) Climate Data Store (CDS) API client, <https://cds.climate.copernicus.eu/api-how-to>.
- [30] F. Cantalloube, J. Milli, C. Böhm, S. Crewell, J. Navarrete, K. Rehfeld, M. Sarazin, and A. Sommani, The impact of climate change on astronomical observations, *Nat. Astron.* **4**, 826 (2020).
- [31] D. Bonaccini Calia, M. Centrone, F. Pedichini, A. Ricciardi, A. Cerruto, and F. Ambrosino, Laser guide star pointing camera for ESO LGS Facilities, in *Adaptive Optics Systems IV*, Proc. SPIE, Vol. 9148 (2014), p. 91483P.
- [32] M. Centrone, D. Bonaccini Calia, F. Pedichini, A. Cerruto, A. Ricciardi, and F. Ambrosino, Laser pointing camera: A valuable tool for the LGS-AO operations, in *Society of Photo-Optical Instrumentation Engineers (SPIE) Conference Series*, Proc. SPIE, Vol. 9909 (2016), p. 99095L.
- [33] In 2021 a heavier binning scheme with 4 pixels in the spatial direction and 2 pixels in the dispersion direction was implemented for the singleHR mode of ESPRESSO.
- [34] Gaia Collaboration, T. Prusti, J. H. J. de Bruijne, A. G. A. Brown, A. Vallenari, C. Babusiaux, C. A. L. Bailer-Jones, U. Bastian, M. Biermann, D. W. Evans *et al.*, The Gaia mission, *Astron. Astrophys.* **595**, A1 (2016).
- [35] Gaia Collaboration, A. G. A. Brown, A. Vallenari, T. Prusti, J. H. J. de Bruijne, C. Babusiaux, C. a. L. Bailer-Jones, M. Biermann, D. W. Evans, L. Eyer *et al.*, Gaia Data Release 2. Summary of the contents and survey properties, *Astron. Astrophys.* **616**, A1 (2018).
- [36] D. G. Monet, S. E. Levine, B. Canzian, H. D. Ables, A. R. Bird, C. C. Dahn, H. H. Guetter, H. C. Harris, A. A. Henden, S. K. Leggett *et al.*, The USNO-B Catalog, *Astron. J.* **125**, 984 (2003).
- [37] F. Patat, O. S. Ugolnikov, and O. V. Postylyakov, UVBVRI twilight sky brightness at ESO-Paranal, *Astron. Astrophys.* **455**, 385 (2006).
- [38] R. N. Wilson, F. Franzia, and L. Noethe, Active optics. I. A system for optimizing the optical quality and reducing the costs of large telescopes. *J. Mod. Opt.* **34**, 485 (1987).
- [39] L. Noethe, F. Franzia, P. Giordano, R. N. Wilson, O. Citterio, G. Conti, and E. Mattani, Active optics. II. Results of an experiment with a thin 1 m test mirror. *J. Mod. Opt.* **35**, 1427 (1988).
- [40] M. Riva, M. Landoni, F. M. Zerbi, D. Mégevand, A. Cabral, S. Cristiani, and B. Delabre, ESPRESSO front end optomechanical configuration, in *Ground-based and Airborne Instrumentation for Astronomy IV*, Proc. SPIE **8446**, 84469E (2012).
- [41] C. Frank, F. Kerber, G. Avila, N. Di Lieto, G. Lo Curto, and A. Manescau, A fibre scrambling unit for the laser frequency comb of ESPRESSO, in *Ground-Based and Airborne Instrumentation for Astronomy VII*, Proc. SPIE **10702**, 107026P (2018).
- [42] F. Zhao, G. Lo Curto, L. Pasquini, J. I. González Hernández, J. R. De Medeiros, I. C. Leão, B. L. Canto Martins, R. Rebolo, A. Suárez Mascareño, M. Esposito *et al.*, Measuring and characterizing the line profile of HARPS with a laser frequency comb, *A&A* **645**, A23 (2021).
- [43] D. Milaković, C.-C. Lee, R. F. Carswell, J. K. Webb, P. Molaro, and L. Pasquini, A new era of fine structure constant measurements at high redshift, *Mon. Not. R. Astron. Soc.* **500**, 1 (2021).
- [44] E. Harel, A. Anretar, J.-P. Antelme, S. Caillon, A. Dussourd, G. Foucaud, H. Jaury, O. Roure, J.-P. William, P. Wuillaume *et al.*, Thin glass shells for AO: From plano to off-axis aspherics, in *Advances in Optical and Mechanical Technologies for Telescopes and Instrumentation II*, Proc. SPIE **9912**, 99120U (2016).
- [45] C. G. Rupert, Mathematics of the reflecting telescope, *Popular Astron.* **26**, 525 (1918).
- [46] A. Cabral, M. Abreu, J. Coelho, G. Ávila, M. Riva, D. Mégevand, N. C. Santos, and F. Pepe, ESPRESSO Coudé-Train: ESO's VLT working as 16-metre telescope, in *Fourth International Conference on Applications of Optics and Photonics*, Proc. SPIE **11207**, 112070V (2019).
- [47] R. Holzlöhner, S. M. Rochester, D. Bonaccini Calia, D. Budker, J. M. Higbie, and W. Hackenberg, Optimization of cw sodium laser guide star efficiency, *Astron. Astrophys.* **510**, A20 (2010).
- [48] D. Bonaccini Calia, Y. Feng, W. Hackenberg, R. Holzlöhner, L. Taylor, and S. Lewis, Laser Development for Sodium Laser Guide Stars at ESO, *The Messenger* **139**, 12 (2010).
- [49] W. Freudling, M. Romaniello, D. M. Bramich, P. Ballester, V. Forchi, C. E. García-Dabló, S. Moehler, and M. J. Neeser, Automated data reduction workflows for astronomy. The ESO Reflex environment, *Astron. Astrophys.* **559**, A96 (2013).
- [50] G. Tejeda, B. Maté, and S. Montero, Overtone Raman spectrum and molecular polarizability surface of CO₂, *J. Chem. Phys.* **103**, 568 (1995).
- [51] DOI: [10.26093/cds/vizier](https://doi.org/10.26093/cds/vizier).
- [52] F. Ochsenbein, P. Bauer, and J. Marcout, The VizieR database of astronomical catalogues, *Astron. Astrophys.* **143**, 23 (2000).
- [53] S. Yu, C. E. Miller, B. J. Drouin, and H. S. P. Müller, High resolution spectral analysis of oxygen. I. Isotopically invariant Dunham fit for the X³Σ⁻, a¹Δ_g, b¹Σ⁺ states, *J. Chem. Phys.* **137**, 024304 (2012).
- [54] B. J. Drouin, H. Gupta, S. Yu, C. E. Miller, and H. S. P. Müller, High resolution spectral analysis of oxygen. II. Rotational spectra of a¹Δ_g O₂ isotopologues, *J. Chem. Phys.* **137**, 024305 (2012).
- [55] B. J. Drouin, S. Yu, B. M. Elliott, T. J. Crawford, and C. E. Miller, High resolution spectral analysis of oxygen. III. Laboratory investigation of the airglow bands, *J. Chem. Phys.* **139**, 144301 (2013).
- [56] S. Yu, B. J. Drouin, and C. E. Miller, High resolution spectral analysis of oxygen. IV. Energy levels, partition sums, band constants, RKR potentials, Franck-Condon factors involving the X³Σ⁻_g, X³Σ⁻_g, a¹Δ_g and b¹Σ⁺_g b¹Σ⁺_g states, *J. Chem. Phys.* **141**, 174302 (2014).
- [57] R. A. Hill, Effect of satellite Q-branches on temperatures computed from oxygen vibrational raman intensities, *J. Quant. Spectrosc. Radiat. Transfer* **21**, 221 (1979).
- [58] R. A. Hill, P. Esherick, and A. Owyong, High-resolution stimulated Raman spectroscopy of O₂, *J. Mol. Spectrosc.* **100**, 119 (1983).

- [59] W. Hackenberg, ESO 4LGSF: Integration in the VLT, Commissioning and on-sky results, SPIE Conference on Astronomical Telescopes+Instrumentation (Edinburgh, 2016).
- [60] A. Friedenauer, V. Karpov, D. Wei, M. Hager, B. Ernstberger, W. R. L. Clements, and W. G. Kaenders, RFA-based 589-nm guide star lasers for ESO VLT: A paradigm shift in performance, operational simplicity, reliability, and maintenance, in *Adaptive Optics Systems III*, Proc. SPIE **8447**, 84470F (2012).
- [61] M. Enderlein, A. Friedenauer, R. Schwerdt, P. Rehme, D. Wei, V. Karpov, B. Ernstberger, P. Leisching, W. R. L. Clements, and W. G. Kaenders, Series production of next-generation guide-star lasers at TOPTICA and MPBC, in *Adaptive Optics Systems IV*, Proc. SPIE **9148**, 914807 (2014).
- [62] L. C. Bradley, Pulse-train excitation of sodium for use as a synthetic beacon, *J. Opt. Soc. Am. B* **9**, 1931 (1992).
- [63] H. Wiesemeyer, R. Güsten, R. Aladro, B. Klein, H.-W. Hübers, H. Richter, U. U. Graf, M. Justen, Y. Okada, and J. Stutzki, First detection of the atomic ^{18}O isotope in the mesosphere and lower thermosphere of Earth, *Phys. Rev. Res.* **5**, 013072 (2023).
- [64] T. Robitaille and E. Bressert, APLPy: Astronomical Plotting Library in Python, Astrophysics Source Code Library, ascl:1208.017 (2012).
- [65] B. M. Morris, E. Tollerud, B. Sipőcz, C. Deil, S. T. Douglas, J. Berlanga Medina, K. Vyhmeister, T. R. Smith, S. Littlefair, A. M. Price-Whelan *et al.*, Astroplan: An open source observation planning package in Python, *Astron. J.* **155**, 128 (2018).
- [66] Astropy Collaboration, T. P. Robitaille, E. J. Tollerud, P. Greenfield, M. Droettboom, E. Bray, T. Aldcroft, M. Davis, A. Ginsburg, A. M. Price-Whelan *et al.*, Astropy: A community Python package for astronomy, *Astron. Astrophys.* **558**, A33 (2013).
- [67] Astropy Collaboration, A. M. Price-Whelan, B. M. Sipőcz, H. M. Günther, P. L. Lim, S. M. Crawford, S. Conseil, D. L. Shupe, M. W. Craig, N. Dencheva *et al.*, The Astropy Project: Building an open-science project and status of the v2.0 core package, *Astron. J.* **156**, 123 (2018).
- [68] <https://astroquery.readthedocs.io>
- [69] A. Ginsburg, M. Parikh, J. Woillez, A. Groener, S. Liedtke, B. Sipocz, T. Robitaille, C. Deil, B. Svoboda, E. Tollerud *et al.*, Astroquery: Access to online data resources, Astrophysics Source Code Library, ascl:1708.004 (2017).
- [70] A. Ginsburg, B. M. Sipőcz, C. E. Brasseur, P. S. Cowperthwaite, M. W. Craig, C. Deil, J. Guillochon, G. Guzman, S. Liedtke, P. Lian Lim *et al.*, Astroquery: An astronomical web-querying package in Python, *Astron. J.* **157**, 98 (2019).
- [71] R. Thomas, Dfitspy: A dfits|fitsort implementation in python, *J. Open Source Softw.* **4**, 1249 (2019).
- [72] D. Foreman-Mackey, D. W. Hogg, D. Lang, and J. Goodman, Emcee: The MCMC Hammer, *Publ. Astron. Soc. Pac.* **125**, 306 (2013).
- [73] F. P. A. Vogt, Fcmaker: Creating ESO-compliant finding charts for Observing Blocks on p2, Astrophysics Source Code Library, ascl:1806.027 (2018).
- [74] F. P. A. Vogt, Fcmaker: Automating the creation of ESO-compliant finding charts for Observing Blocks on p2, *Astron. Comput.* **25**, 81 (2018).
- [75] J. D. Hunter, Matplotlib: A 2D Graphics Environment, *Comput. Sci. Eng.* **9**, 90 (2007).
- [76] C. R. Harris, K. J. Millman, S. J. van der Walt, R. Gommers, P. Virtanen, D. Cournapeau, E. Wieser, J. Taylor, S. Berg, N. J. Smith *et al.*, Array programming with NumPy, *Nature (London)* **585**, 357 (2020).
- [77] W. McKinney, Data Structures for Statistical Computing in Python, in *Proceedings of the 9th Python in Science Conference* (2010), pp. 56–61.
- [78] The pandas development team, Pandas-dev/pandas: Pandas, Zenodo (2021).
- [79] P. Virtanen, R. Gommers, T. E. Oliphant, M. Haberland, T. Reddy, D. Cournapeau, E. Burovski, P. Peterson, W. Weckesser, J. Bright *et al.*, SciPy 1.0: Fundamental algorithms for scientific computing in Python, *Nat. Methods* **17**, 261 (2020).
- [80] A. C. Carnall, SpectRes: A fast spectral resampling tool in Python, [arXiv:1705.05165](https://arxiv.org/abs/1705.05165).
- [81] N. Earl, E. Tollerud, C. Jones, W. Kerzendorf, shaileshahuja, D. D'Avella, T. Robitaille, rosteen, A. Ginsburg, I. Busko *et al.*, Astropy/specutils: V1.1, Zenodo (2020).
- [82] F. Bonnarel, P. Fernique, O. Bienaymé, D. Egret, F. Genova, M. Louys, F. Ochsenbein, M. Wenger, and J. G. Bartlett, The ALADIN interactive sky atlas. A reference tool for identification of astronomical sources, *Astron. Astrophys.* **143**, 33 (2000).
- [83] W. A. Joye and E. Mandel, New Features of SAOImage DS9, in *Astronomical Data Analysis Software and Systems XII ASP Conference Series*, Vol. 295 (2003), p. 489.
- [84] [cdsarc.u-strasbg.fr \(130.79.128.5\)](https://cdsarc.u-strasbg.fr/130.79.128.5).
- [85] <https://cdsarc.unistra.fr/viz-bin/cat/Jother/PhRvR>.
- [86] R. J. Le Roy, Y. Huang, and C. Jary, An accurate analytic potential function for ground-state N_2 from a direct-potential-fit analysis of spectroscopic data, *J. Chem. Phys.* **125**, 164310 (2006).
- [87] P. F. Bernath, *Spectra of Atoms and Molecules*, third edition ed. (Oxford University Press, Oxford, 2016).
- [88] J. J. Barrett and A. Weber, Pure-rotational Raman scattering in a CO_2 Electric Discharge, *J. Opt. Soc. Am.* **60**, 70 (1970).